ELECTRONIC PHASE SEPARATION AND RELATED ASPECTS OF RARE EARTH MANGANATES AND COBALTATES OF THE TYPE, $Ln_{1-X}A_XMO_3$

(Ln = trivalent rare earth, A = divalent alkaline earth and M = Mn or Co)

A Thesis

Submitted for the degree of

Doctor of Philosophy

By

Asish K Kundu

To

JAWAHARLAL NEHRU CENTRE FOR ADVANCED SCIENTIFIC RESEARCH

(A Deemed University)

BANGALORE, INDIA

June 2006

Dedicated to

My

Beloved Mother

Contents

CHAPTER 3

3. Electronic phase separation and related aspects of rare earth cobaltates

DECLARATION

I hereby declare that the matter embodied in this thesis entitled **"ELECTRONIC PHASE SEPARATION AND RELATED ASPECTS OF RARE EARTH MANGANATES AND COBALTATES OF THE TYPE, $Ln_{1-x}A_xMO_3$ (Ln = trivalent rare earth, A = divalent alkaline earth and M = Mn or Co)"** is the results of investigations carried out by me at the Chemistry and Physics of Materials Unit, Jawaharlal Nehru Centre for Advanced Scientific Research, Bangalore, India, under the supervision of ***Professor C. N. R. Rao, FRS*** and it has not been submitted elsewhere for the award of any degree or diploma.

In keeping with the general practice of reporting scientific observations, due acknowledgement has been made whenever the work described is based on the findings of other investigators. Any omission that might have occurred by oversight or error of judgement is regretted.

Asish K Kundu

Asish K Kundu

CERTIFICATE

I hereby certify that the work described in this thesis entitled **"ELECTRONIC PHASE SEPARATION AND RELATED ASPECTS OF RARE EARTH MANGANATES AND COBALTATES OF THE TYPE, $Ln_{1-x}A_xMO_3$ (Ln = trivalent rare earth, A = divalent alkaline earth and M = Mn or Co)"** has been carried out by **Mr. Asish K Kundu**, under my supervision at the Chemistry and Physics of Materials Unit, Jawaharlal Nehru Centre for Advanced Scientific Research, Bangalore, India.

Prof. C. N. R. Rao

(Research Supervisor)

Acknowledgements

There are no words that can express my deep respect and sincere gratitude towards my research supervisor Professor C. N. R. Rao, FRS. It was his invaluable guidance, immense support and constant encouragement that have been instrumental in developing me as a scientific researcher. I am also grateful to him for not only suggesting me the research problems but also providing me with constant guidance till their completion. I am overjoyed and also honored for getting the opportunity of working under him who is not only a great scientist but also a noble human being. I shall always remember his endless enthusiasm, dedication and commitment towards science and will try to imbibe these fantastic qualities in me as well.

I am extremely thankful to Professor Per Nordblad, Uppsala University, Sweden, for permitting me to conduct some of my research work in his laboratory under his valuable guidance. Our long discussions on spin-glasses and related properties have improved my understanding of many aspects of rare earth manganates and cobaltates. His keen interest in my work and his friendly approach had always been very encouraging during my stay in Sweden.

I am thankful to Professor E. V. Sampathkumaran, TIFR, Mumbai, for helping me with some of my magnetic measurements and data interpretation.

My sincere thanks to Drs. Vanitha, Motin and Sudheendra for making me understand few of the basic concepts regarding synthesis of samples and instrument operation.

I would like to thank Dr. K. Ramesha, UCSB, for helping me with some of my magnetic measurements.

My sincere thanks and regards to Professor A. R. Raju, for help during single crystal growth and magnetoresistance measurements.

I would like to express my sincere thanks to Dr. A. Govindaraj who has provided great technical help.

I am thankful to Dr. A. Sundaresan and Mr. Vangadesh who helped me in carrying out few of my magnetic measurements.

I thank all my teachers, Professors K. S. Narayan, G. U. Kulkarni, A. R. Raju, S. Natarajan, N. Chandrabhas, S. Balasubramanian, S. Narashimhan, S. K. Pati and U. V. Waghmare.

I thank all the faculty members of CPMU, Professors K. S. Narayan, G. U. Kulkarni, N. Chandrabhas, S. Balasubramanian, Dr. M. Eswaramoorty and Dr. A. Sundaresan for their cordial and helpful attitude.

I express my heartfelt thanks to Motin'da, Anne and my wife for critically going through the thesis and suggesting useful corrections.

I shall be ever thankful to Mrs. Indumati Rao for her warmth and hospitality.

I am extremely grateful to all my past and present labmates, Dr. Vanitha, Dr. Sudheendra, Dr. Sachin, Dr. Amitava, Dr. Motin, Claudy, Jyoti, Anne, Behera, Meenakshi, Thiru, Sreeraj, Nimmi, Avinash, Anupama, Dr. Prabhakar and Dr. Ayi for help and cooperation in the lab.

I would like to thank my batch mates, Prashant, Neena, Soumya, Gargi, Lakshmi and Joydeep for making my stay in JNC a memorable experience.

I would also like to thank all my friends in JNC, Chandu, Madhu, Bhat, Ved, Angappane, Selvi, Gomati, Vivek, Gopal, Pavan, Dhritiman, Manu, Kabra, Saikrishna, Kumar, Dinesh, Prasenjit, Debabrata, Mousumi, Ayan, Nantu, Kirti, Jaita, Moumita, Himadri, Anil, Dr. Neels, Dr. Multi and Kishore for their warm friendship.

I express my thanks to all my friends in IISC, Motin'da, Partha'da, Arindam'da, Sudip'da, Shyama'da, Krishanu'da, Pal, Moumita, Ujjal, Kanishka, Sandip, Prakashbhai, Sukhendu, Partha, Animesh and Dipti.

My deepest thanks to my old friends, Amit, Neeraj, Sujit, Sanjib, Pranab, Sushrut, Shukla, Rupesh, Ankur'da, Ashok, Bidyut, Goutam, Kalyan and Kaberi'di for their moral support.

I am very thankful to Mr. Anil, Mr. Basavaraj, Mr. Vasu, Mr. Arokianathan, Mr. Srinath and Mrs. Usha for their invaluable technical assistance. I would

also like to thank Mrs. Sashi, Mr. Gowda, Mr. Xaviers and Mrs. Veena for their continuous help.

I thank all the staff members of the academic section in JNC for their continuous help starting from my admission till the completion of my Ph.D. I would thank all the library staff for their help. I am thankful to the staff of the computer lab for their generous computer facility. I am also grateful to the administrative staff of JNC for their continuous help.

I thank the University Grants Commission (UGC), India, the Swedish agencies SIDA/SAREC and VR through the Asian-Swedish research program and JNCASR for their financial support.

I would also like to thank my sisters, uncle and aunty, and my wife for their love and great support throughout.

Finally, I express my deepest sense of thanks and gratitude to my mother; it was her great support and encouragement that helped me to take up research as my career.

Preface

This thesis presents the results of investigations of rare earth manganates and cobaltates. It is organized into three chapters. ***Chapter 1*** gives a brief overview of colossal magnetoresistance, charge-ordering, electronic phase separation and related properties of rare earth manganates and cobaltates of the formula $Ln_{1-x}A_xMO_3$ (Ln = trivalent rare earth, A = divalent alkaline earth, and M = Mn or Co).

Chapter 2 deals with the results of the investigations of the rare earth manganates. Electronic phase separation and related aspects of the hole-doped rare earth manganates form the major part of these investigations. Measurements of magnetic and electron transport properties have been employed to study the phenomena after suitably characterizing the materials by the X-ray diffraction (Cu-Kα radiation) and energy dispersive X-ray analysis. The various aspects studied include the effects of A-site cation radius, and novel effects of cation size-disorder. The re-entrant ferromagnetic transition in rare earth manganates with relatively small A-site cations wherein ferromagnetism occurs on cooling the charge-ordered state is also shown to be results of phase separation.

Electronic phase separation, cation size-disorder and related aspects in hole-doped compositions of the rare earth cobaltates are described in ***chapter 3***. The effects of cation size and size-disorder on the properties of polycrystalline as well as single crystalline cobaltates of the formula $Ln_{0.7}Ca_{0.3}CoO_3$ (Ln = La, Pr or Nd) have been examined.

1. A BRIEF OVERVIEW OF RARE EARTH MANGANATES AND COBALTATES $Ln_{1-x}A_xMO_3$ (Ln = trivalent rare earth, A = divalent alkaline earth, M = transition metal oxide)

1.1 INTRODUCTION

For nearly the last five decades, there has been extensive research on ABO_3-type perovskite oxides of the general formula $Ln_{1-x}A_xMO_3$ (Ln = trivalent rare earth, A = divalent alkaline earth, M = transition metal oxide). Some of the novel properties of the perovskite oxides are known for some time, particularly the paramagnetic (PM) to ferromagnetic (FM) transition at Curie temperature (T_C) and the associated insulator-metal transition (T_{IM}) in the case of manganates and cobaltates [1]. The discovery of colossal magnetoresistance (CMR) in doped manganates has renewed great interest in this system since the early 90's. Apart from CMR, the rare earth manganates exhibit rich phase diagram spanning a wide range of magnetic properties and phenomena like charge ordering (CO), orbital ordering, spin-glass behavior and electronic phase separation (EPS) [2, 3]. These phenomena represent a combined interaction between the spin, the lattice, the charge and the orbital degrees of freedom. Such interactions are manifested in single crystal and polycrystalline samples as well as in the thin films. Experimentally it has been observed that the doped perovskite manganates, $Ln_{1-x}A_xMnO_3$, reveal rich phase diagrams which include spin, charge and orbital ordered phases as well as some magnetic phases. The properties of these oxides can be tuned either by external factors or by

chemical means. In certain critical range of cation doping at the A-site, the rare earth manganates exhibit simultaneous occurrence of ferromagnetism and metallicity, along with a CMR in the vicinity of T_C or T_{IM} [4]. The doped rare earth cobaltates, $Ln_{1-x}A_xCoO_3$, are also interesting in that they exhibit compositionally controlled insulator-metal transitions and ferromagnetism, the ferromagnetic phase being metallic [5]. The properties of both the manganates and cobaltates are affected by the size of the A-site cations.

Some of the perovskite-based transition metal oxides are known to exhibit compositional and electronic inhomogeneities arising from the existence of more than one phase in crystals of nominally monophasic composition. This is understood in terms of electronic phase separation described recently in the literature [3]. Such a phenomenon occurs because of the comparable free energies of the different phases [2, 3]. The phase-separated hole-rich and hole-poor regions give rise to anomalous properties such as weak FM moments in an antiferromagnetic regime. A variety of magnetic and electronic properties manifest themselves in $Ln_{1-x}A_xMnO_3$ depending on the various factors such as the A-site cation size and size-disorder as well as external factors such as temperature, magnetic field etc. In the last few years electronic phase separation in rare earth manganates and cobaltates have attracted considerable attention.

1.2 TRANSITION METAL OXIDES

Transition metal oxides (TMOs) constitute one of the most interesting classes of materials exhibiting a wide variety of structures and physical properties. Metal oxides crystallize in a variety of structures, and bonding in these materials can vary from ionic

(e.g. MgO, $Fe_{1-x}O$) to metallic (TiO, ReO_3). Associated with such changes in bonding, these materials also show a gamut of fascinating properties. The unusual properties of TMOs are due to unique nature of the outer *d*-electrons, the metal-oxygen bond varying anywhere from ionic to metallic. The phenomenal range of electronic and magnetic properties exhibited by TMOs is equally interesting. There are oxides with metallic properties (e.g. RuO_2, ReO_3, $LaNiO_3$) at one end of the range and oxides with insulating behavior ($BaTiO_3$) at the other end [5]. There are oxides that traverse both these regimes with the change in temperature, pressure or composition (V_2O_3, $La_{1-x}Sr_xVO_3$). Interesting electronic properties also arise from charge-density waves ($K_{0.3}MoO_3$), charge ordering (Fe_3O_4) and defect ordering ($Ca_2Mn_2O_5$, $Ca_2Fe_2O_5$). Examples of TMOs are known with diverse magnetic properties; like ferromagnetic (CrO_2, $La_{0.5}Sr_{0.5}MnO_3$), ferrimagnetic (Fe_3O_4, $MnFe_2O_4$), and antiferromagnetic (NiO, $LaCrO_3$). Many oxides posses switchable orientation states as in ferroelectric ($BaTiO_3$, $KNbO_3$) and ferroelastic ($Gd_2Mo_3O_{12}$) materials. The discovery of high temperature superconductivity in cuprates has focused world wide interest on the physics and chemistry of TMOs since 1986. The unusual properties of TMOs that distinguish them from metallic elements, covalent semiconductors and ionic insulators arise from several factors [5]. One of the reasons is the oxides of *d*-block transition elements have narrow electronic bands, because of the small overlap between the metal *d* and oxygen *p* orbitals. The band widths are typically of the order of 1 or 2 eV (rather than 5-15 eV, for metal).

TMOs possessing several types of complex structure have been characterized in recent years. These include not only the well known perovskite, spinel, pyrochlore and hexagonal ferrite structures, but also the octahedral tunnel structures. Many TMOs are

not truly three dimensional, but have low-dimensional features. For example, La_2CuO_4 and La_2NiO_4 with the K_2NiO_4 structure are quasi two dimensional compared to $LaCuO_3$ and $LaNiO_3$, which are three dimensional perovskites. Because of their varied features and properties, it has not been possible to establish a straight forward theoretical model to cover all TMOs. However, there have been many convenient approaches to understand their electronic structures and properties.

It is well established that the transition metal oxides are strongly correlated electron system. In other words, the crystal structure, electrical and magnetic properties and so on are intimately related to each other. Hence, it is appropriate to have a brief overview of the structure, properties and their inter-relation mechanism in these perovskite oxides.

1.3 PEROVSKITE STRUCTURE

In general, the rare earth manganates and cobaltates crystallize in the perovskite structure. The ABO_3-perovskite is a simple cubic structure (*Pm3m*) as shown in Fig. 1.1. However, many perovskites distort a little from this structure even at room temperature.

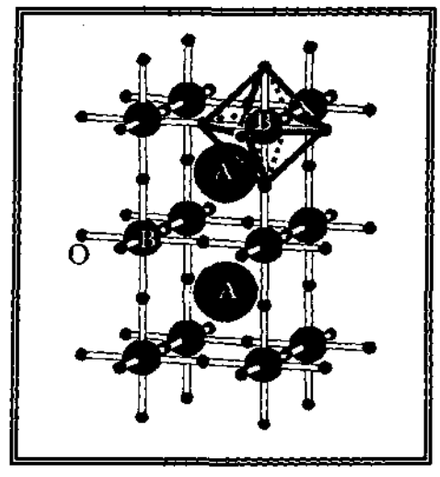

Figure 1.1 Simple ABO_3 perovskite structure.

The perovskite structure is most stable when the Goldschmidt tolerance factor, t, is unity (for cubic structure), which is defined by, $t = (r_A + r_O)/\sqrt{2}\ (r_B + r_O)$ where, r_A, r_B and r_O are the average ionic radius of the A, B and O ions respectively. Deviation of 't' from unity leads to the structural distortion. For a small deviation in t (i.e. $t < 1$), the crystal structure changes from cubic to rhombohedral or orthorhombic symmetry. In this situation the ⟨Mn-O-Mn⟩ bond angle decreases from 180°. The perovskite structure occurs only within the range $0.75 \leq t \leq 1.00$. To stabilized the A and B-site cations in their respective 12- and 6-fold co-ordinations, the lower limits of their radius should be set as $r_A > 0.90$ Å and $r_B > 0.51$ Å. The stability of the perovskite structure of manganates and cobaltates depends on the relative size of the Ln/A and M ions in $Ln_{1-x}A_xMO_3$. In rare earth manganates Ln/A cation is surrounded by eight corner sharing MnO_6 octahedra, which build a 3D network. The smaller ionic radius of the cations results in a lower value of 't', consequently more is the lattice distortion. The increase in lattice distortion significantly decreases the ⟨Mn-O-Mn⟩ bond angle from 180°, which strongly affects the physical properties of perovskite manganates. When $t < 1$, there is a compression of the Mn-O bonds, which in turn induces a tension on Ln-O bonds. A cooperative rotation of

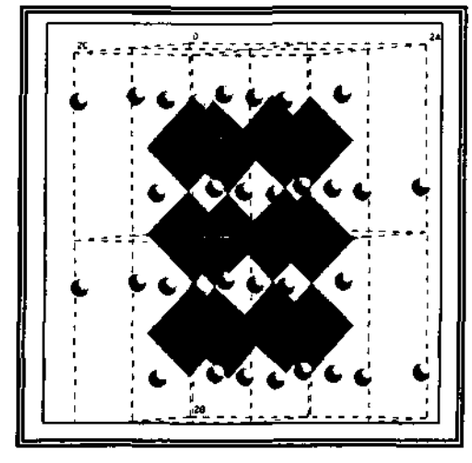

Figure 1.2 Orthorhombic $GdFeO_3$ structure. Iron ions are octahedrally co-ordinated by the oxygen ions.

the MnO_6 octahedra and a distortion of the cubic structure counteract these stresses. When $0.75 < t < 0.90$, the MnO_6 octahedra tilts cooperatively to give an enlarged orthorhombic (*Pbnm*) structure of $GdFeO_3$ (Fig. 1.2). For $0.90 < t < 1.0$, buckling of octahedra is not found and small distortion leads to lower symmetry structure. Hence, tilting of MnO_6 octahedra along [111] direction gives rise to the rhombohedral structure ($LaAlO_3$) whereas along [001] direction leads to tetragonal structure ($SrTiO_3$). The rare earth oxides can be crystallized not only in orthorhombic and cubic structure, but in tetragonal, hexagonal, rhombohedral, and monoclinic structures as well. The orthorhombic structure has four formula units per unit cell (Z = 4), the rhombohedral has Z = 2 and hexagonal has Z = 6 as compared to one in the case of ideal cubic perovskite.

1.4 PROPERTIES OF PEROVSKITE OXIDES

Perovskite oxides constitute an enormous group of solids exhibiting a wide variety of magnetic and electron transport properties [5]. These properties depend on the nature of the transition metal oxides present in the system. It is convenient to discuss the oxides of transition metals and nontransition metals separately. The examples of nontransition metal oxides are Na_2O, MgO, Al_2O_3 and SiO_2. Their electronic structure consists of a filled valence band (derived mainly from O:2*p*) and an empty conduction band (derived from the outer shells of metal atoms) separated by a large energy gap (~ 10 eV). They are therefore diamagnetic insulators under ordinary conditions [5]. Another type of perovskite oxides, in which two classes of transition metal ion are present in their structure: those in which the metal ion has d^0 electronic configuration and those where the *d* shell is partly filled (Table 1.1). The former class of oxides has a filled oxygen 2*p*

valence band and an empty metal *d* conduction band (energy gap ~ 3-5 eV). The presence of this class of materials at octahedral sites exhibit spontaneous ferroelectric and antiferroelectric distortions. At high temperature these materials show intrinsic electron conduction, which may be due to oxygen loss or insertion of electropositive metal atoms into these oxides [5].

Table 1.1 Different types of transition metal oxides [ref 5]

d^0 metal oxides Sc_2O_3, TiO_2, V_2O_5, CrO_3, ZrO_2, Nb_2O_5, MoO_3, HfO_2, Ta_2O_5, WO_3	Diamagnetic semiconductors or insulators when pure, but exhibit *n*-type extrinsic conduction when doped or slightly reduced.
d^n metal oxides TiO, NbO, CrO_2, ReO_2, RuO_2, OsO_2, MoO_2, RhO_2, WO_2, IrO_2 and ReO_3	Metallic and Pauli paramagnetic (CrO_2 is ferromagnetic)
Ti_2O_3, Ti_3O_5, Ti_4O_7, Ti_5O_9, V_2O_3, V_3O_5, V_4O_7, VO_2, NbO_2 and Fe_3O_4	Exhibit temperature-induced nonmetal–metal transition
MnO, FeO, CoO, NiO, Cr_2O_3, Fe_2O_3 and Mn_3O_4	Mott insulators
f^n metal oxides PrO_2, Ln_2O_3 (Ln = rare earth), Pr_nO_{2n-2}, Tb_nO_{2n-2} and EuO	Insulators or hopping semiconducto Paramagnetism characteristic of f^n configuration. EuO shows nonmetal–metal transition.

Transition metal oxides with partly filled *d* electron can be metallic or semiconducting. Some of them show temperature-induced nonmetal to metal transitions (Table 1.1). Magnetic properties also vary over a wide range from Curie-Weiss paramagnetism through spontaneous magnetism to Pauli paramagnetism. Metal oxides with d^n electronic configuration exhibit metallic properties when the overlap between

orbitals of the valence shells of constituent atoms is large. Two kinds of metallic behavior can be distinguished: one due to strong cation-cation interaction and other due to strong cation-anion-cation interaction [5]. In Table 1.1, we have also included typical rare earth oxides containing localized $4f^n$ electrons.

A number of isostructural transition metal oxide families exhibit perovskite, spinel, corundum, rutile and other structures, which also show systematic changes in electron transport properties. We shall discuss the properties of perovskite oxides in some detail. *The perovskite structure is ideally suited for the study of 180° cation-anion-cation* interaction of octahedral site cations as shown in Fig. 1.3. The possibility of cation-cation interaction is remote because of the large interaction distance along the face diagonal. The variety in the properties of perovskites is illustrated by the following examples: $BaTiO_3$ is ferroelectric, $SrRuO_3$ is ferromagnetic, $LaFeO_3$ is weakly ferromagnetic, and $BaPb_{1-x}Bi_xO_3$ is superconducting, while $LaCoO_3$ shows a nonmetal-metal transition. Several perovskite oxides exhibit metallic conductivity; typical examples are ReO_3, $LaTiO_3$ and $LaNiO_3$. Metallic conductivity in perovskite oxides is entirely due to strong cation-anion-cation interaction.

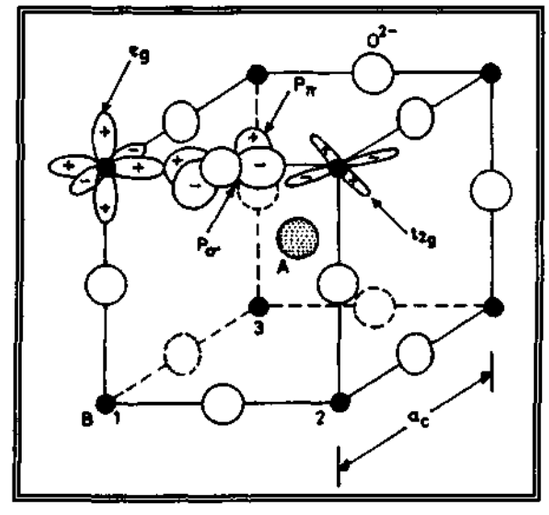

Figure 1.3 Perovskite structure, showing the possibility of cation-anion-cation interaction along the cube edge.

1.5 RARE EARTH MANGANATES

Rare earth manganates of the type $Ln_{1-x}A_xMnO_3$ can be regarded as solid solutions between the end members $Ln^{3+}Mn^{3+}O_3$ (e.g. $LaMnO_3$) and $A^{2+}Mn^{4+}O_3$ (e.g. $BaMnO_3$), leading to mixed valence compounds such as $(Ln^{3+}A^{2+})(Mn^{3+}\ Mn^{4+})O_3$. Therefore, when La^{3+} in $LaMnO_3$ is progressively substituted by a divalent A^{2+} cation as in $Ln_{1-x}A_xMnO_3$ (A = Ba, Sr or Ca), the doping effect introduces Mn^{4+} in place of Mn^{3+} ion. As the proportion of Mn^{4+} increases the orthorhombic distortion decreases. Generally, a sequence of *Tetragonal* → *Orthorhombic* → *Rhombohedral* → *Cubic* is found with increasing the Mn^{4+} ions in these manganates. The relative concentration of Mn^{3+} and Mn^{4+} play an important role in determining the physical properties of these manganates. The substitution at the A-site not only alters the Mn-O bonds, but also the ⟨Mn-O-Mn⟩ bond angle, which is related to the A-site cation radius and tolerance factor as discussed in previous section. Substitution of different rare earths in A-site as in $Ln_{0.7-x}Ln'_xA_{0.3}MnO_3$ (Ln and Ln' are trivalent rare earth, A is divalent alkaline earth), allows one to vary the ⟨Mn-O-Mn⟩ angle without any change in the Mn-O bond distances [6].

It is well known that the tilting of MnO_6 octahedra primarily controls the electron transfer between the neighboring Mn: e_g orbital mediated by the O: $2p$ orbitals. Thus, the tilting of the MnO_6 reduces the e_g bandwidth with the decrease in ⟨Mn-O-Mn⟩ bond angle [7]. This finally affects the magnetic and electron transport properties of the perovskite manganates.

1.5.1 Crystal field effects

There are two characteristic distortions which influence the perovskite structure of rare earth manganates. First one is due to the cooperative tilting of the MnO_6 octahedra

which is essentially established below 1000 K [2, 5]. This distortion is a consequence of the mismatch of the ionic radius and various factors as discussed in previous section. The other distortion arises from the Jahn-Teller (JT) effect due to Mn^{3+} ion, which distorts the MnO_6 octahedra in such a way that there are long and short Mn-O bonds. This occurs below a characteristic temperature for particular compounds. This is well understood in terms of crystal field theory or the ligand field theory, which describes how the *d*-electron of transition metal ions is perturbed by the chemical environment. The most effective distortion is the basal plane distortion (called Q_2 mode) as shown in Fig. 1.4, with one diagonally opposite oxygen-pair displaced outwards and the other pair displaced inward. It is well established that a JT distortion involving a displacement of oxygen ions ≥ 0.1Å can split the e_g-band of the manganate (which forms the conduction band) and opens a gap at the Fermi level.

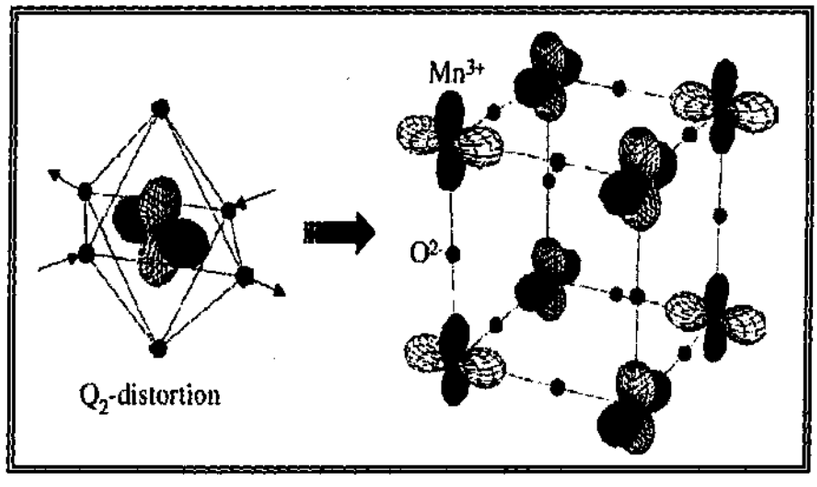

Figure 1.4 Jahn-Teller distorted MnO_6 octahedra.

The magnitude of the crystal field splitting of *d*-orbital determines whether the transition metal ion occurs in the low-spin (LS) or high-spin (HS) configuration. Fig. 1.5, shows a

schematic of the band diagram of $LaMnO_3$ to elucidate how JT distortion splits the conduction band and makes the material insulating. The octahedral ligand environment around Mn-ion split the five *d*-orbitals into t_{2g}-triplet (d_{xy}, d_{yz} and d_{zx}) and e_g-doublet ($d_{x^2-y^2}$ and d_{z^2}) state. The t_{2g} orbitals have their lobes oriented between the oxygen neighbors, while e_g orbitals are directed towards the oxygen neighbors.

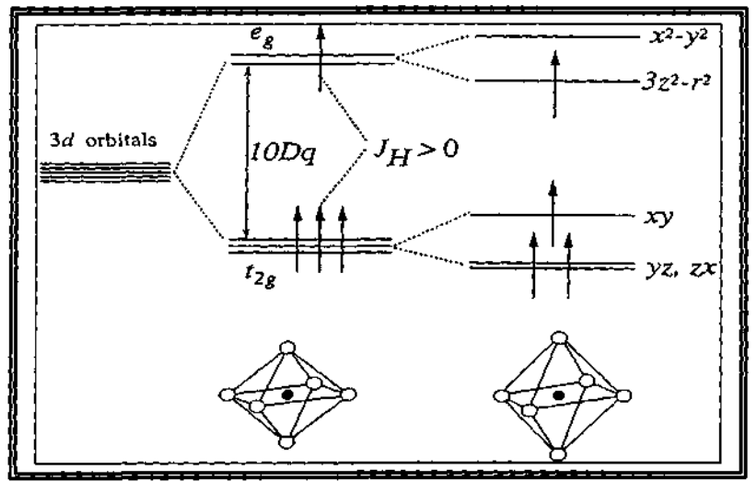

Figure 1.5 Field splitting of the five-fold degenerate atomic 3*d* levels.

Thus, the t_{2g} orbitals have a lower energy compared to the e_g orbitals because of the less electrostatic repulsion of electrons on neighboring sites. In this system, the resulting crystal-field splitting, Δ_{cf}, between t_{2g} and e_g orbital is around 1.5 eV. The value Δ_{cf} (= 10 *Dq*), can be estimated by comparing the spectra of Mn^{3+} in various distorted environments. Further splitting of the e_g orbitals due to the JT effect opens a gap at the Fermi level. The intra-atomic exchange energy responsible for Hund's highest multiplicity rule, Δ_{ex} (or J_H), is greater than Δ_{cf} i.e. $\Delta_{ex} > \Delta_{cf}$ for Mn^{3+} ion. Therefore manganese ions are always in high spin state; the divalent manganese, Mn^{2+} has a stable

$3d^5$ electronic configuration, a half filled shell $t_{2g}^3 e_g^2$ with S = 5/2, the Mn^{3+} is in $3d^4$ configuration with $t_{2g}^3 e_g^1$ and S = 2, where as Mn^{4+} has stable $3d^3$ with t_{2g}^3 and S = 3/2. The spin only moments of manganese ions are 5, 4 and 3 μ_B, respectively. In this connection, it is necessary to mention another perovskite oxide $LaCoO_3$, which does not follow Hund's first rule and shows three spin states for Co^{3+} ion [8]. The thermally driven spin-state transition in cobaltates is a consequence of the subtle interplay between the crystal field splitting (Δ_{cf}) and the Hund's coupling energy (Δ_{ex}). The Δ_{cf} usually decreases as the temperature is increased, whereas Δ_{ex} is insensitive to temperature since it's an atomic quantity [9]. The spin-state of undoped $LaCoO_3$ (Co^{3+} ion), exhibit a gradual crossover with increasing temperature from the low-spin (LS) state ($t_{2g}^6 e_g^0$; S = 0) to intermediate-spin (IS) state ($t_{2g}^5 e_g^1$; S = 1) at around 100 K and finally to high-spin (HS) state ($t_{2g}^4 e_g^2$; S = 2) [9]. This results from the competition of the crystal field with energy Δ_{cf} (t_{2g}- e_g splitting) and the interatomic (Hund) exchange energy Δ_{ex}, leading to redistribution of electrons between t_{2g} and e_g levels.

In $LaMnO_3$, it is well established that JT distortion due to the Mn^{3+} ion ($t_{2g}^3 e_g^1$) plays a crucial role. The distorted Mn^{3+} ions have three Mn-O bonds (1.91, 1.96 and 2.19 Å) and the ⟨Mn-O-Mn⟩ bond angle is around ~ 150°. While in $La_{1-x}A_xMnO_3$ the creation of Mn^{4+} ion removes the JT distortion leading to more cubic structure. The transfer interaction of e_g-electrons is greater in rhombohedral or pseudocubic phase than in the orthorhombic phase because the ⟨Mn-O-Mn⟩ bond angle becomes closer to 180°. Clearly, the doping or the Mn^{4+} ion plays an important role in this material to provide the FM and metallic behavior by suppressing the JT distortion.

1.5.2 Magnetic and electron transport properties

(a) Magnetic properties: The parent perovskite manganates such as $LaMnO_3$, $PrMnO_3$ and $NdMnO_3$ are insulator at all temperatures and undergo an antiferromagnetic (AFM) transition at low temperatures. The AFM ordering is of A-type, where ferromagnetically aligned *ab*-layers are coupled antiferromagnetically along c-axis. The different types of magnetic ordering are discussed below. The insulating nature of the parent compounds as well as the anisotropic magnetic interaction is related to their structure, in particular the JT distortion around Mn^{3+} ions. The A-site cation, as mentioned earlier affects the JT distortion, in particular the Q_2 mode distortion which gives rise to long and short Mn-O distances, leading to the anisotropic exchange interaction. Removal of the JT distortion reduces the AFM interaction and this in turn destroys the AFM ordering.

Wollan and Koehler [10] studied the magnetic and crystallographic lattices in the series of manganates with the compositions, $Ln_{1-x}A_xMnO_3$, as a function of Mn^{4+} ion. The data obtained from neutron diffraction study of these manganates are in good agreement with Goodenough's predictions for different kinds of magnetic ordering.

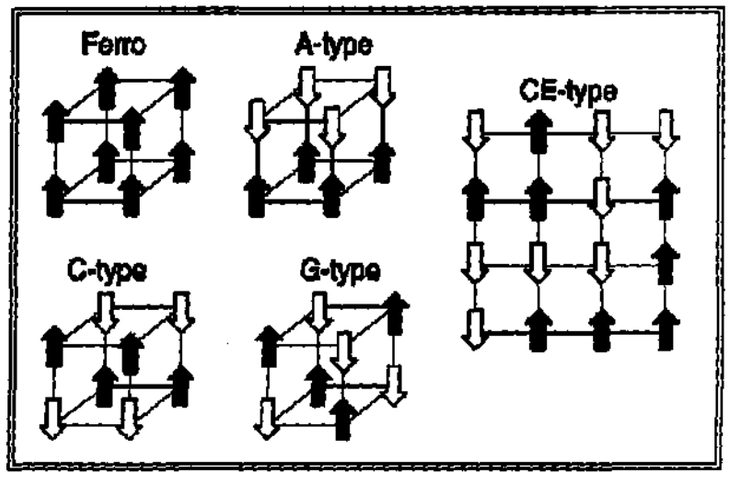

Figure 1.6 Schematic representations of different types of magnetic ordering.

The mixed-valence manganates (Mn^{3+} and Mn^{4+}) can exhibit magnetic ordering, charge ordering and orbital ordering. Some of the simplest magnetic ordering for B-site cation is shown in Fig. 1.6, which represent one FM and four AFM (A-, C-, G- and CE-type) ordering. In $Ln_{1-x}A_xMnO_3$ series, the magnetic lattice for $x = 1$ composition (i.e. $CaMnO_3$) corresponds to the G-type, whereas the $x = 0$ composition (i.e. $LaMnO_3$) has A-type ordering. The other types are found across the series as x varied, corresponding to the AFM ordering of Mn moments, which are C or CE-type. In C-type AFM, Mn-ions order in alternate [111] planes, whereas in the CE-type they order in alternate [110] planes. When these perovskite manganates are hole-doped as in $Ln_{1-x}A_xMnO_3$ (Ln = La, Pr or Nd and A = Ba, Sr or Ca) the proportion of Mn^{4+} increases. The material becomes FM with a well defined T_C at a finite value of x and also metallic below T_C. The FM and I-M transitions in the $La_{1-x}Sr_xMnO_3$ compositions are well defined [11] as shown in Fig. 1.7.

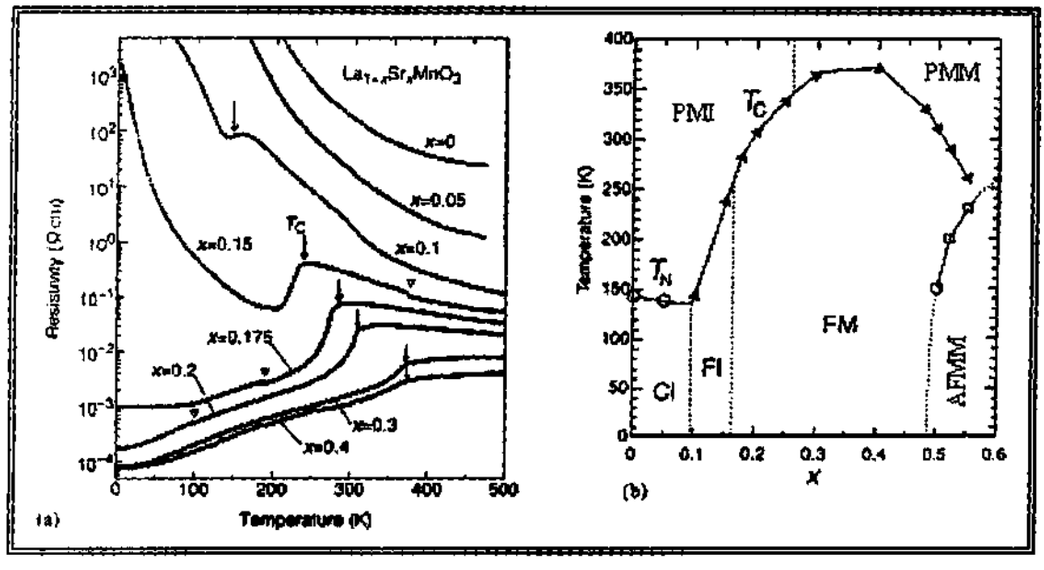

Figure 1.7 (a) Temperature variation of electrical resistivity and (b) magnetic phase diagram for $La_{1-x}Sr_xMnO_3$ [ref 11].

Although, the compositions with $x > 0.5$ are essentially AFM, and the FM clusters would also be present in the AFM phase. The material is generally ferromagnetic metal (FMM) below T_C when $0.2 < x < 0.5$, and become paramagnetic insulator (PMI) when $T > T_C$. Thus, I-M transition occurring around T_C (Fig. 1.7) is well understood on the basis of the Zener double-exchange mechanism, which is discussed in the following section [12].

Zener Double-Exchange (DE)

The simultaneous observation of ferromagnetism and itinerant electron behavior (metallicity) in perovskite manganates is explained through Zener double-exchange model. This involves the hopping of an electron from Mn^{3+} ($3d^4$, $t_{2g}^3 e_g^1$; S = 2) to Mn^{4+} ($3d^3$, t_{2g}^3; S = 3/2) via oxygen ion where the Mn^{3+} and Mn^{4+} ions exchange takes place i.e.

$$Mn^{3+}\ O^{2-}\ Mn^{4+} \rightarrow Mn^{4+}\ O^{2-}\ Mn^{3+}$$

The transfer of an electron occurs from the Mn^{3+} site to the intervening O^{2-} ion with a simultaneous transfer of an electron from the O^{2-} ion to the Mn^{4+} site. Such a double transfer is referred to as Double-Exchange (DE). The integral defining the exchange energy in such a system is non-vanishing only if the spins of the two *d*-orbitals are parallel. That is, the lowest energy of the system is one with a parallel alignment of the spins on the Mn^{3+} and Mn^{4+} ions. Due to this the spins of the incomplete *d*-orbitals of the adjacent Mn is accompanied by an increase in the rate of hopping of electrons and therefore by an increase in electrical conductivity. Thus, the mechanism which leads to enhanced electrical conductivity requires an FM coupling. It is assumed that the intra-atomic exchange, J_{ex}, is large compared to the transfer integral, t_{ij}, between the two Mn sites [7]. The relation between the electrical conductivity and ferromagnetism by the DE mechanism is given by the magnitude of the exchange energy, U_{ex}, is given by

$$U_{ex} = h\nu/2$$

Where ν is the frequency of oscillation of the electron between two Mn sites and h is Planck's constant. The diffusion coefficient for Mn^{4+} is related to exchange energy by

$$D = \alpha^2 U_{ex}/h$$

Where α is the lattice parameter. Making use of the Einstein equation relating conductivity, σ, and D as, $\sigma = ne^2D/kT$

Where n is the number of Mn^{4+} ions per unit volume, one obtains

$$\sigma = xe^2 U_{ex}/\alpha hkT$$

Here x is the fraction of Mn^{4+} ions in $Ln_{1-x}A_xMnO_3$. Since in the FM transition T_C is related to the exchange energy by the approximate relation, $U_{ex} \approx kT_C$, one can write:

$$\sigma \approx (xe^2/\alpha h)(T_C/T)$$

This equation relates the electrical conductivity to ferromagnetic T_C and the fraction of Mn^{4+} ions. We would therefore expect the IM transition in the manganates to occur at T_C. DE is strongly affected by structural parameters such as ⟨Mn-O-Mn⟩ bond angle or the Mn-Mn transfer integral (t_{ij}).

The t_{2g} electrons of the Mn^{3+} ion are localized on the Mn-site giving rise to a local spin of 3/2, but the e_g state, which is hybridized with the oxygen $2p$ state, can be localized or itinerant and only those electrons which have their spins parallely aligned give rise to conductivity in the hopping process. There is strong Hund's rule interactions between the e_g and the t_{2g} electrons. Goodenough [13] pointed out that FM interaction is governed not only by the DE interaction, but also by the nature of the super exchange interactions. The magnetic exchange is strongly dependent on the structural distortion, as indeed shown by

electronic structure calculations [12]. Recent investigations bring out the essential role of DE, along with the crucial role of the lattice and the electron-lattice interactions [12].

Superexchange interaction

A pair of electrons of like spin, localized on degenerate orbitals, is lower in energy than a pair with opposite spins by an amount called the intra-atomic exchange energy. There are two classes of exchange interactions between spins on different atoms. (a) Direct exchange, occurs between moments on atoms that are close enough to have significant overlap of their wave functions and decreases rapidly with increasing interatomic distance and (b) Indirect exchange, where the spin moments are coupled over relatively large distances. Indirect exchange manifests through an intermediary nonmagnetic ion (Superexchange) or through itinerant electrons (Ruderman-Kittel-Kasuya-Yoshida interaction; RKKY). Superexchange generally occurs in insulators while RKKY coupling is important in metal [14].

Superexchange or AFM interaction between localized moments of ions in insulators that are too far apart to interact by direct exchange operates through the intermediacy of a nonmagnetic ion. Superexchange is able to occur when localized electron states as described by the formal valances are stabilized by an admixture of excited states involving electron transfer between the cation and the anion. The DE discussed above is different from superexchange, which also describes cation-anion-cation interactions. Different types of superexchange interaction are possible, depending on the structure of the oxide and the electronic configuration of the cations. Two important types are delocalized- and correlation- superexchange. Delocalized superexchange involves transfer of electron from one cation to another, as a result of

cation-cation or cation-anion-cation interaction. Correlation superexchange is restricted to cation-anion-cation interaction. The Anderson-Goodenough-Kanamori rules [14] apply to superexchange interaction, according to which, a 180° cation-anion-cation interaction in a d^3-O- d^3 system is AFM (Fig. 1.8(a)), but a d^3-O- d^4 interaction would be FM. Whereas, a 90° cation-anion-cation interaction between half filled orbitals is FM, provided the orbitals are bonded orthogonally (Fig. 1.8(b)).

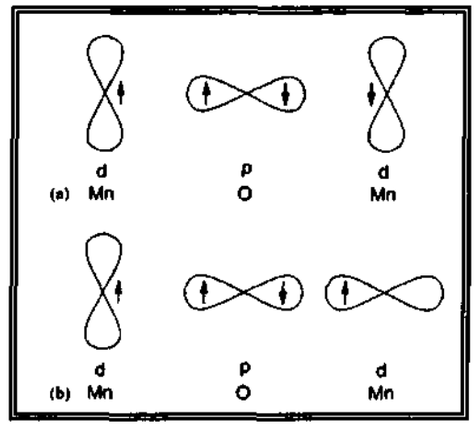

Figure 1.8 A cation-anion-cation interaction in a *Mn*-O- *Mn* system.

Superexchange involving σ bonds is stronger than those involving π bonds. In the 3*d* transition metal mono-oxides, the ordering temperature T_N increases in the order MnO < FeO < CoO, because the σ interaction increases in that order. For cations of the same electronic configuration, superexchange is stronger for the higher valency cation (e.g. $Fe^{3+} > Mn^{2+}$) [5].

Superexchange interaction would not, however, give rise to increased electrical conduction as in the DE mechanism. Zener's model has been extended or modified by several workers. In particular, de Gennes [15] has shown that the energy of the electrons gets lowered if there is canting of the sublattices, giving rise to a canted-spin AFM state, and a situation found when *x* in $La_{1-x}A_xMnO_3$ is small.

(b) Electrical properties: Electrical conductivity, thermal conductivity, Seebeck effect and Hall effects are some of the common electron transport properties of perovskite oxides that characterize the nature of charge carriers. On the basis of electrical properties, oxides material may be classified into metals, semiconductors and insulators, wherein charge carriers move in the band states. The electron transport properties of oxides provide useful criteria for distinguishing localized and itinerant electron in solids. In certain semiconductors and insulators, charge carriers are localized, their motion involves a diffusive process. The semiconductor or insulator like transport behavior in oxide materials is characterized by three models defined by $\log \rho \alpha 1/T^n$ where n = 1, 2 or 4; (i) Here n = 1, corresponds to a simple Arrhenius law, which describe the thermally activated behavior due to band gap or mobility edge, (ii) When, n = 2, the hopping is referred to as nearest neighbor hopping (NNH) of small polarons controlled by Coulombic forces and (iii) n = 4, correspond to variable range hopping (VRH). The hopping dynamics is controlled by the collective excitation of the charge carriers [16]. To understand the transport mechanism in rare earth perovskite oxides the data was analyzed based on these three models.

The electron transport property of $Ln_{1-x}A_xMnO_3$ has one to one correspondence with the magnetic properties, exhibiting low resistivities in the FM region and semiconducting or insulating behavior in the CO and AFM regions. The manganates with $x < 0.5$ have a conduction band more filled than half filled whereas those with $x > 0.5$ have conduction band less than half filled. The number of charge carriers in the system can be assumed to be equal to the Mn^{4+} ion introduced into the lattice for small doping in the A-site. The process involves the transfer of electrons from Mn^{3+} to Mn^{4+} by DE

mechanism. Most of the perovskite manganates (parent compounds) are paramagnetic insulators at room temperature and exhibit an increase in electrical resistivity with the decrease in temperature. Compositions that are FM show insulating behavior above T_C, but with decreasing temperature (below T_C) the resistivity decreases as in the metals. This, I-M transition is therefore associated with a peak in resistivity at a temperature T_{IM}. Generally, T_{IM} is somewhat lower than T_C and the sharpness of the transition in polycrystalline samples as well as in films often depends on the sample quality.

1.5.3 Colossal magnetoresistance

The change in electrical resistance of a material in response to an applied magnetic field is referred to as magnetoresistance (MR). In general MR is defined by

$$MR = [\rho(H) - \rho(0)]/ \rho(0) = [\Delta\rho/\rho(0)]$$

Where, $\rho(H)$ and $\rho(0)$ are the resistivity in the presence and absence of magnetic field (H), at a particular temperature. MR can be positive or negative depending on the materials. In magnetic material MR is negative, because of the suppression of spin disorder by the magnetic field. Many solids exhibit small MR owing to the Lorenz force that a magnetic field exerts on moving electrons which is known from physics text book since 1950. Very large MR, referred to as giant magnetoresistance (GMR) was first reported by Baibich et al [17] in layered Fe/Cr metallic multilayer. Large MR was observed in powder and single crystals of doped manganates of the type $Ln_{1-x}A_xMnO_3$ in mid 1980's. But the renewed interest in these manganates started with the report of negative MR in $Nd_{0.5}Pb_{0.5}MnO_3$ [18], which showed MR of 50 % near T_C (184 K). This report was followed by studies on thin films by several other workers [19]. In rare earth manganates, MR was found to be extremely large and hence termed as colossal magnetoresistance

(CMR) by Jin et al [19]. The discovery of negative GMR in perovskite manganates [19] has attracted wide attention. The magnitude of negative GMR in these materials can be very large, close to 100 %. Therefore many researchers prefer to call it CMR, as distinct from GMR in layered or granular metallic materials [20]. In metallic multilayers or granular alloys; the mechanism involves spin-polarized transport. Also, in rare earth manganates spin-polarized transport is responsible for the large negative MR, but it is distinctly different from the metallic multilayers.

The application of a magnetic field (~ a few Tesla) leads to a significant decrease in the resistivity of perovskite manganates; the magnitude of decrease in resistivity (i.e. MR) is highest in the region of T_C or T_{IM}. A typical example of $La_{1-x}A_xMnO_3$ is shown in Fig. 1.9, where the magnetization, resistivity and CMR are plotted as a function of temperature at various fields. The highest CMR effect is observed for x = 0.25 composition, the value is around 80 % for an applied field of 4 Tesla (T) [21].

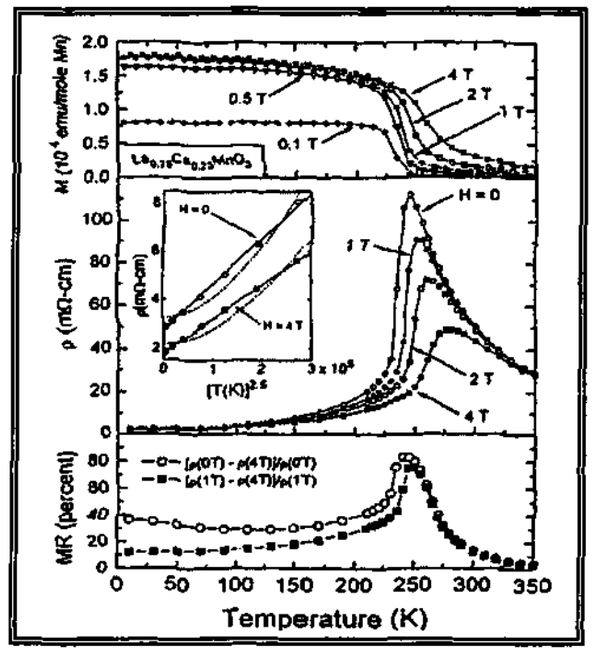

Figure 1. 9 Temperature variation of Magnetization, Resistivity and MR for $La_{0.75}Ca_{0.25}MnO_3$ (at different fields) [ref 21].

A self doped sample of the type $La_{1-\delta}Mn_{1-\delta}O_3$ also exhibit CMR effects similar to that observed in $Ln_{1-x}A_xMnO_3$ compositions [22]. The effect of CMR and related properties have been studied in the Ruddlesden-Popper phases by Moritomo et al [23] and Mahesh et al [23], in (SrO)($La_{1-x}Sr_xMnO_3)_n$ compound. Another class of compound is the ordered double perovskite (Sr_2FeMoO_6), which exhibits tunneling magnetoresistance (TMR) at room temperature [24]. Other than the perovskite manganates, CMR is also found in $Ti_2Mn_2O_7$ (with pyrochlore structure) which has only Mn^{3+} ions [25]. Rare earth cobaltates such as $La_{0.5}Ba_{0.5}CoO_3$ [8] and $La_{1-x}Sr_xCoO_3$ [26] are also known to exhibit CMR effect at low temperatures. Although the MR in cobaltates is much lower than the manganates, the actual peak value is around 8 %. In cobaltates the highest MR ever observed is in layered perovskite based cobaltate oxides of the type $LnBaCo_2O_{5.4}$ (Ln = Gd, Eu) [27].

1.5.4 Different types of ordering in rare earth manganates

The parent compound of perovskite manganates, $LaMnO_3$ has a layered AFM structure, referred to as A-type AFM ordering as shown in Fig. 1.10(a) [10]. Orbital ordering of $3x^2$-r^2 or $3y^2$-r^2 type accompanied by the JT distortion leads to a superexchange coupling in $LaMnO_3$, which is FM in planes and AFM between the planes (Fig. 1.10(a)).

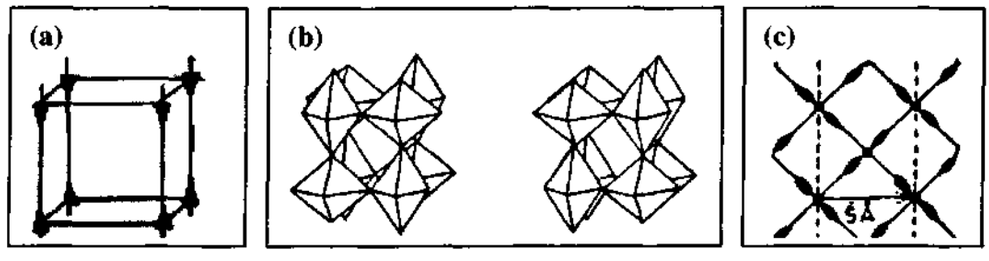

Figure 1.10 Schematic representations of different types of ordering in $LaMnO_3$.

Orbital ordering is shown in Fig. 1.10(c). Without JT distortion $LaMnO_3$ would have been an FM insulator instead of an A-type AFM insulator [28]. Since there is a doubly degenerate e_g orbital in each Mn^{3+} ion, $LaMnO_3$ and $NdMnO_3$ show a fine interplay between spin and orbital ordering. The orbital ordering is coupled to JT distortion; Fig. 1.10(b) describes the JT distortion in $LaMnO_3$.

Among these ordering the most important in manganates is charge ordering (CO), which is known since 1939 in the Fe_3O_4 [29]. Basically, the transition metal oxides with different charged cations of the same element show the phenomenon of CO, wherein the cations order on specific lattice sites. Such an ordering of the cation leads to the localization of the electrons rendering the material insulating in the CO state and is often accompanied by a change in crystal symmetry. In $Ln_{1-x}A_xMnO_3$, besides orbital and spin ordering, we can have CO because of the presence of Mn^{3+} and Mn^{4+} ions. The study of CMR in manganates has brought forth novel features related to the CO in these oxides.

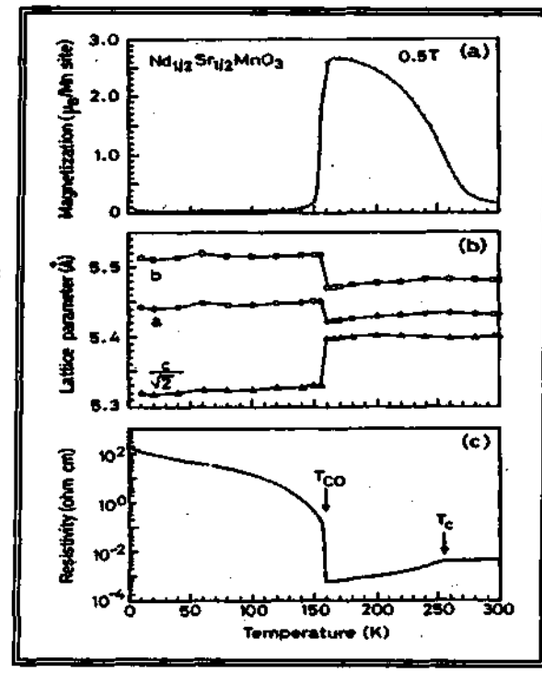

Figure 1.11 Temperature variation of the (a) magnetization, (b) lattice-parameters and (c) resistivity of $Nd_{0.5}Sr_{0.5}MnO_3$ – [ref 31].

The CO in the manganates is interesting because DE gives rise to FM and metallic state while the charge-ordered state is associated with insulating and AFM (or paramagnetic) behavior. In general, small Ln and A ions stabilize the CO state. The lattice distortion plays a crucial role in the CO, orthorhombic distortion stabilizing the charge-ordered state. The charge-ordered state can be melted into a metallic state, by the application of a magnetic field. An observation on the manganates [30] reveals two types of scenarios, as exemplified by $Nd_{0.5}Sr_{0.5}MnO_3$ and $Pr_{0.65}Ca_{0.35}MnO_3$. In $Nd_{0.5}Sr_{0.5}MnO_3$ an FM metallic state gives over to an AFM-CO state around 150 K (T_{CO}) accompanied by a change in the lattice parameters as shown in Fig. 1.11 [31]. The CO state in this manganates is associated with CE-type AFM ordering. In the CE-type ordering Mn^{3+} and Mn^{4+} ions are arranged like a checker board and the Mn^{3+} sites are JT distorted [10]. The charged ordered states in the manganates exhibit CE-type AFM ordering at the same temperature as the CO transition or at a lower temperature ($T_{CO} \geq T_N$). For the case of $Pr_{0.65}Ca_{0.35}MnO_3$ an insulating CO state (T_{CO} ~ 200 K) becomes AFM around 140 K (T_N) and then finally transforms to a canted-spin AFM state at a still lower temperature (~ 110 K) [32].

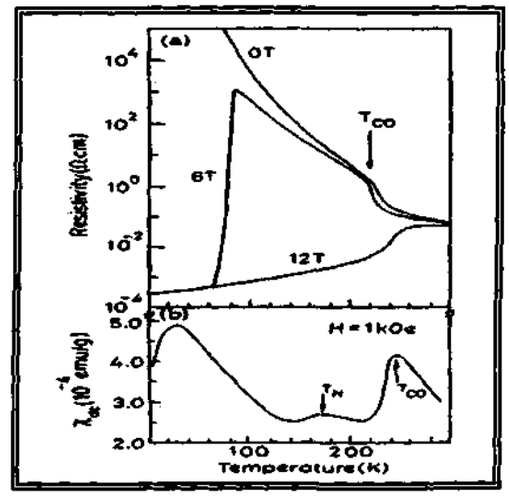

Figure 1.12 Temperature variation of (a) resistivity and (b) magnetization of $Pr_{0.65}Ca_{0.35}MnO_3$ [ref 32].

The application of a magnetic field melts the charged-ordered state in most of the manganates giving rise to metallic behavior (Fig. 1.12). By increasing the size of the A-site cations or by the application of pressure, the CO state in the manganates can be transformed to the FMM state [33].

1.5.5 Cation size effect

In rare earth manganates CO, CMR and other interesting physical phenomena are governed by the width of the e_g band, which is directly determined by the average radius of A-site cation $\langle r_A \rangle$ or the tolerance factor. This is because a distortion of the $\langle$Mn-O-Mn$\rangle$ bond angle affects the transfer interaction of the e_g conduction electrons (holes). In the manganates, the T_C, increases with $\langle r_A \rangle$, whereas T_{CO} increases with the decrease in $\langle r_A \rangle$. The increase in $\langle r_A \rangle$ is equivalent to increase in the external hydrostatic pressure and is therefore accompanied by an increase in the $\langle$Mn-O-Mn$\rangle$ angle and the e_g band width.

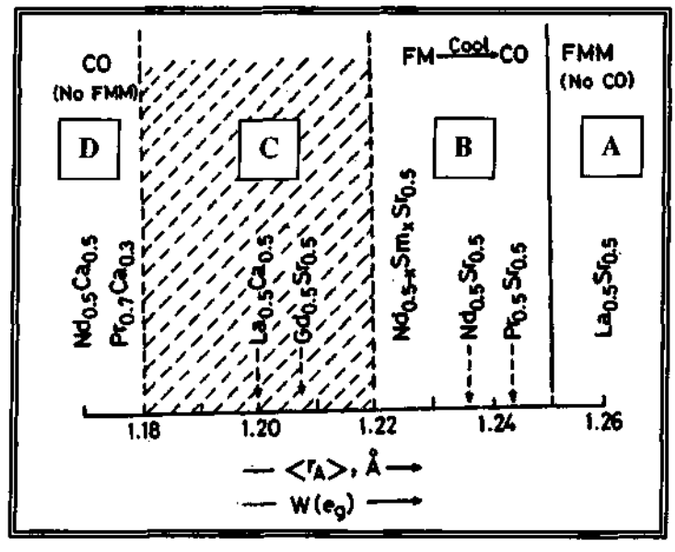

Figure 1.13 Schematic diagram showing the prevalence of CO and FM states in manganates depending on the $\langle r_A \rangle$ or the e_g bandwidth [ref 35].

The sensitivity of T_{CO} to $\langle r_A \rangle$ is studied by several workers [34] and is generally attributed to an increase in tilting of the MnO_6 octahedra as the $\langle r_A \rangle$ decreases.

Figure 1.13, shows a schematic phase diagram of the rare earth manganates, which describe the FM metal, AFM insulator, spin and charge ordered insulating state with the variation of $\langle r_A \rangle$ [35]. In region A, when $\langle r_A \rangle$ is large (e.g. $La_{1-x}Sr_xMnO_3$), only ferromagnetism and the associated IM transition occur (with no CO). With a slight decrease in $\langle r_A \rangle$ as in region B, the FM metallic state transform to AFM charge-ordered state ($T_{CO} = T_N$) on cooling the system (e.g. $Nd_{0.5}Sr_{0.5}MnO_3$, $\langle r_A \rangle$ = 1.236 Å). When $\langle r_A \rangle$ is sufficiently small (region D) as exemplified by compounds $Pr_{0.7}Ca_{0.3}MnO_3$ with $\langle r_A \rangle$ of 1.17 Å [36], no ferromagnetism is encountered and CO occurs in the paramagnetic state. Depending on the $\langle r_A \rangle$ value, the CO state can be melt to FM metallic state by the application of magnetic field. However, in $Y_{0.5}Ca_{0.5}MnO_3$ ($\langle r_A \rangle$ ~1.13 Å), the charged-ordered state ($T_N < T_{CO}$) is robust and is not affected at very high magnetic field (> 25T) [28]. Manganates in region C, show rather complex behavior; by the variation of $\langle r_A \rangle$ one can bring manganates in the region of B and D to region C. Thus, in $La_{0.25}Nd_{0.25}Ca_{0.5}MnO_3$ with $\langle r_A \rangle$ = 1.19 Å, on cooling the system a novel re entrant FM transition occurs from a CO state [37]. There is coexistence of two phases in the temperature range of 150-220 K, around the CO-FM metallic transition. Thus, the formation of FM clusters in an AFM-CO matrix in the manganates give rise to interesting magnetic properties like CMR, electronic phase separation, spin-glass etc. The magnetic and electrical properties of the manganates are consistent with the occurrence of electronic phase separation and glassy magnetic behavior corresponding to a critical average radius $\langle r_A^c \rangle$ of 1.18 Å [38].

Cation size-disorder (σ^2) effect

The effect of cation size-disorder on the various physical properties of manganates has been reported by several workers. As discussed in previous section, the ferromagnetic T_C and insulator-metal transition T_{IM} increase with increase in $\langle r_A \rangle$. But, if there is considerable mismatch in the radius of the different A-site cations, then the T_C does not increase with increase in $\langle r_A \rangle$ as shown in Fig 1. 14.

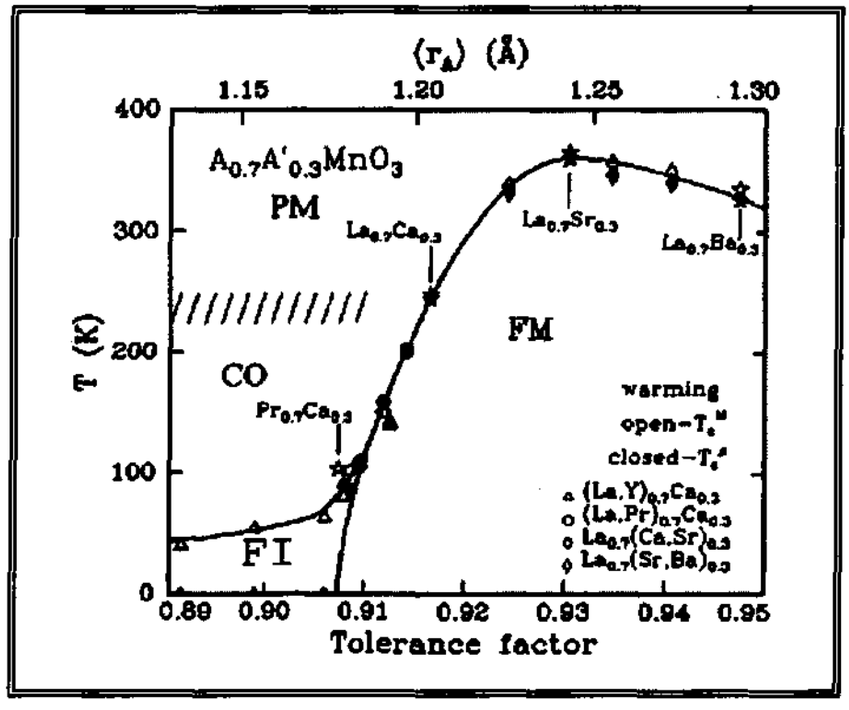

Figure 1.14 Magnetic phase-diagram of the $A_{0.7}A'_{0.3}MnO_3$ series of manganates [ref 39].

The size-disorder effect arising from the mismatch of the A-site cation on the T_C or T_{IM} has been analyzed by the σ^2 parameter, where σ^2 is defined as, $\sigma^2 = \sum x_i r_i^2 - \langle r_A \rangle^2$. Here x_i ($\Sigma x_i = 1$), is the fractional occupancy of the A-site ions, r_i is the corresponding ionic radii and $\langle r_A \rangle$ ($\langle r_A \rangle = \Sigma x_i r_i$) is the weighted average radius calculated from r_i values

[39]. The T_C decreases significantly with increase in variance σ^2, which is reported for both the manganates and cobaltates by several workers [40]. A similar study of the variation of T_{CO} with σ^2 in manganates for fixed $\langle r_A \rangle$ values of 1.17 and 1.24 Å, has shown that T_{CO} is not very sensitive to size mismatch [40].

1.6 PHASE SEPARATION IN PEROVSKITE OXIDES

The coexistence of more than one phase at a particular temperature is referred to as phase separation; a new phenomenon recently found to occur in certain transition metal oxides [3, 41]. The phase separation gives rise to electronic inhomogeneity and is associated with a diverse variety of electronic and magnetic properties. This is not expected for nominal monophasic compound. This is due to non uniformity in impurity distribution, as it can have an electronic origin or could also arise from the presence of magnetic impurities. Intrinsic inhomogeneities are present even in the best quality crystal available. Such phase separation can be controlled or changed by temperature, magnetic fields and other external factors. In these types of phase separation, a high carrier density favors FM ordering and/or metallicity. If carrier concentration is low, the FM metallic phase can occur in one part of the crystal keeping the rest part as an insulating and AFM phase. Impurity phase separation is different from electronic phase separation (EPS), there is no mutual charging of phases in the former. The diffusion of impurity atom has to be sufficiently large to give rise to phase separation in such system. One such example is the case of oxygen-excess La_2CuO_4 [41]. The EPS has been observed in magnetic semiconductors such as heavily doped EuSe and EuTe [41]. In these systems, the crystal is AFM at low temperatures and the conducting electrons occur in the droplets. The EPS

is entirely reversible, and in general, is the result of a competition between charge localization and delocalization. The large concentration of charge carriers giving rise to FM metallic state in a part of the crystal causes mutual existence of two phases. At relatively small carrier concentration, the conducting FM regions are separated and form droplets (Fig. 1.15(a) & (b)) or stripes (Fig.1.15(c)). With increasing carrier concentration, the volume of the FM phase increases rendering the droplets to coalesce and gives rise to a situation as shown in Fig. 1.15.

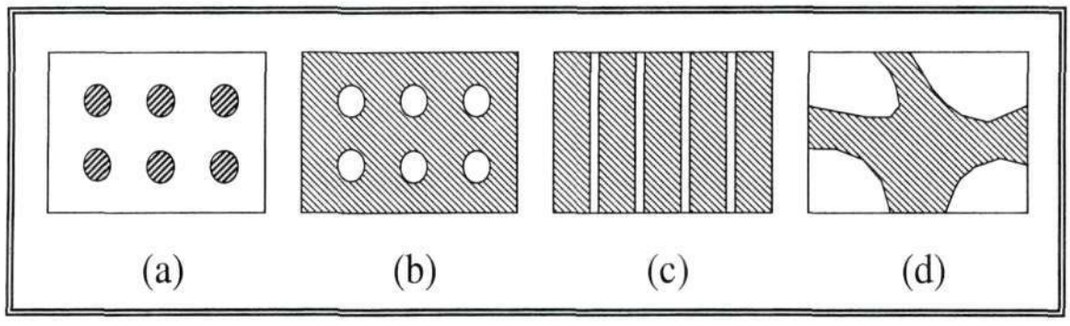

Figure 1.15 Schematic representation of microscopic phase-separation between ferromagnetic metallic (hatched regions) and non-ferromagnetic insulating state (white regions).

An interesting phenomenon of phase separation is that it covers a wide range of length scales anywhere between one to a few hundred of nanometer. The phase separation on a larger length scale is not possible because of strong Coulomb energy. In the presence of Coulomb interaction, the microscopically charged ordered state is stabilized giving rise to clusters of one phase embedded in another. The size of the clusters depends on the competition between DE and Coulomb forces. In phase separation, the phases of different charge densities are generally expected to give rise to nanometer (1-200 nm) scale clusters. This is related to the larger phase-separated

domains which would break up into small pieces because of Coulomb interactions. The JT distortion associated with the Mn^{3+} ions and CO of Mn^{3+} and Mn^{4+} ions compete with DE interaction and promote the insulating AFM behavior [41]. The techniques used to probe the phase separation in different length scales (Fig. 1.15) are, scanning probe microscopy, atomic force microscopy, neutron diffraction, NMR and Mossbauer spectroscopies. Figure 1.16, shows the presence of electronic inhomogeneities in the $La_{1-x}Ca_xMnO_3$ manganates observed by scanning tunneling microscope (STM) [42]. The dark field electron microscopy images of $(La_{1-y}Pr_y)_{1-x}Ca_xMnO_3$ shows a clear competition between CO-AFM versus FM phase, which can be tuned by varying the relative amount of La and Pr [38, 43].

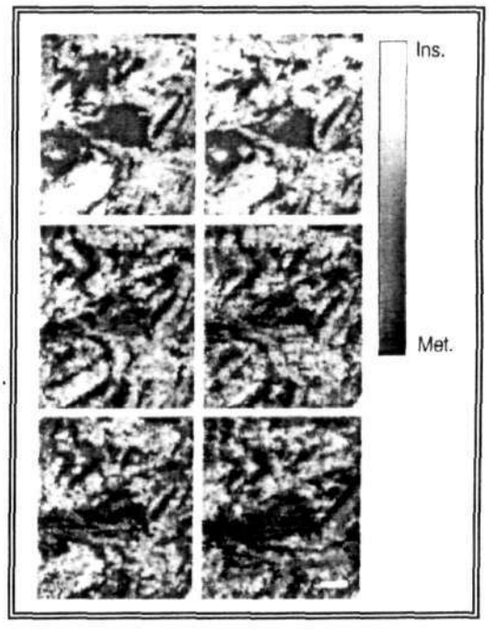

Figure 1.16 STM-image of the local electronic structure of $(La,Ca)MnO_3$ below T_C (scale bar: 100 nm). Light colors represent the insulating whereas dark colors are metallic region [ref 42].

Renner et al [44] have reported the evidence of phase separation even at room temperature. High resolution X-ray and neutron diffraction investigations have shown that in $Nd_{0.5}Sr_{0.5}MnO_3$ manganates three macroscopically different phases coexist at low

temperatures [45]. Recently, the phase separation scenario has been reported in rare earth cobaltates system, using X-ray photo electron spectroscopy. Also, Wu et al [46] have observed the magnetic phase-separated regions in $La_{1-x}Sr_xCoO_3$.

1.7 SPIN-GLASS SYSTEMS

One of the main fields of research in condensed matter physics over the last few decades involves non-equilibrium dynamics of glassy systems. The spin-glass represents a non-equilibrium state which is a rather complex kind of condensed state in solid state physics. In 1970's the spin-glasses were all important, and enormous effort was made to measure and explain the unique freezing (an unconventional spin-glass transition) and the low temperature glassy behavior [47]. In the following years experimental and theoretical studies have revealed some strong support of this new magnetic phenomenon, which are associated with the frustration and disorderness of the magnetic system [48]. The nature of this new kind of material raises many fundamental questions and thus its complete theoretical description, is still under discussion.

In brief, the spin-glass material can be described as, a magnetic system in which the interactions between the magnetic moments are "in conflict" with each other, due to some frozen-in structural disorder. Therefore, there is an absence of conventional long-range ordering (FM or AFM type) in these systems. Thus, the spin-glasses consist of an ensemble of disorder spins, and represent a model system for the statistical mechanics of a system with quenched randomness. Nevertheless these systems exhibit a "freezing transition" to a state with a new kind of "order", where the spins are aligned in random directions. The actual spin ordering in the spin-glass is a problem belonging to the

physics of structurally disorder materials, and does not arise in more conventional regular systems. Because of the spin disorder at low temperature, the spins are subject to different types of interactions like: FM (positive) or AFM (negative). In this situation a particular spin will receive conflicting information on the way of ordering from its nearest neighbors and therefore it will not be possible for the system to arrange in a certain spin configuration to minimize its energy. This phenomenon is commonly known as frustration [49], which is shown schematically in Fig. 1.17.

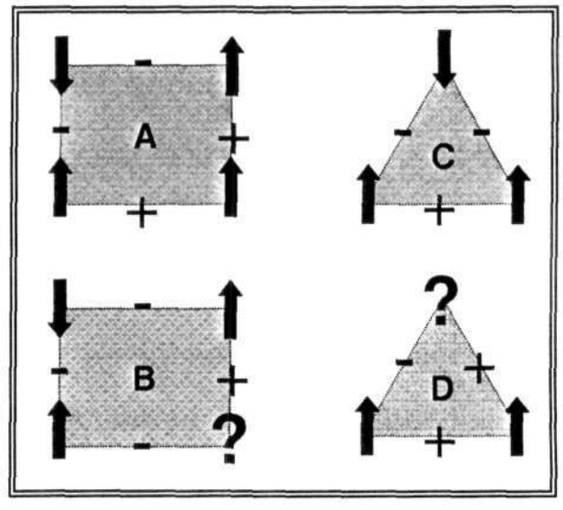

Figure 1.17 Schematic representations of spin-glass behavior. The positive and negative sign represents FM and AFM interactions.

Figure 1.17(A) represents a square lattice without frustration, since all positive and negative interactions are satisfied. The spin on the upper left couple antiferromagnetically with the spins on the upper right and lower left, while the spin on the lower right couples ferromagnetically with them. In Fig. 1.17(B), the frustration appears, since there is no even number of positive and negative spins. Therefore, the frustration originates from the disorder of the interactions. Figure 1.17(C) represents different spin arrangements in the triangular lattices. In this case, there is no magnetic disorder, since all sites are occupied and there is no frustration, but it appears in Fig. 1.17(D) as in square lattice.

In order to perform experiments on SG, first of all it is necessary to make sure that the given system does not fall in the category of ferromagnet (disorder), antiferromagnet or paramagnet at all temperatures. Furthermore, the characteristic phenomena observed in spin-glasses; such as the sharp 'cusp' in the frequency-dependent ac-susceptibility in low fields, first observed by Cannela and Mydosh [47] is a fairly universal feature. The classical spin-glass materials are noble metals (Au, Ag, Cu etc.) weakly doped by transition metal ions (Fe, Mn etc.). In recent years, a lot of materials have been reported in the literature, which show spin-glass behavior with perovskite and other structures as discussed below. Experimentally, it has been amply demonstrated that both 3D Ising ($Fe_{0.5}Mn_{0.5}TiO_3$) and Heisenberg (Ag(Mn)) spin-glass systems exhibit dynamic critical behavior on approaching the spin-glass temperature, T_{sg}, which correspond to a second order phase transition [50]. At low temperature both Ising and Heisenberg spin-glasses exhibit similar non-equilibrium dynamics and an infinitely slow approach towards a thermodynamic equilibrium state.

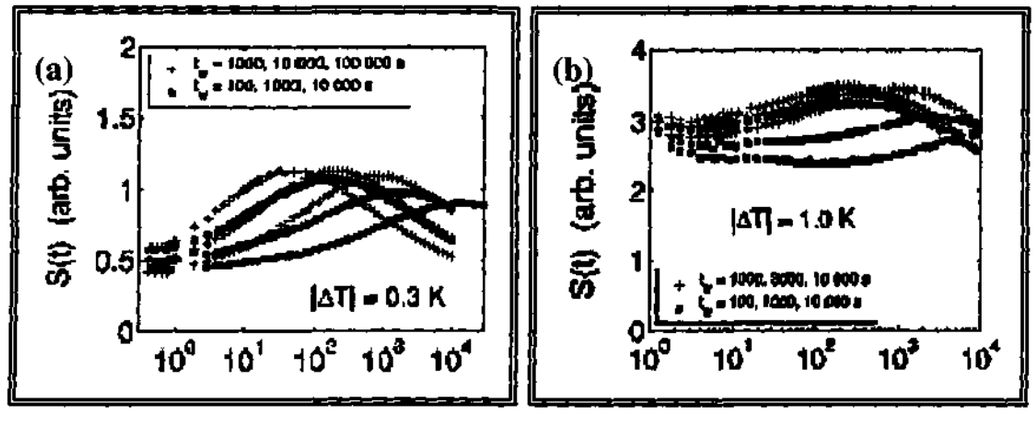

Figure 1.18 Relaxation rate vs time plot for (a) Ag (11% Mn) (b) $Fe_{0.5}Mn_{0.5}TiO_3$ [ref 51].

This means that below T_{sg}, the ZFC spin-glasses never reach equilibrium, in other words the equilibration time is infinite for spin-glass state. Therefore the experiments on low temperature phases seem to be like a non-equilibrium system and the results are age dependent [48]. Once the system is kept constant at low temperature phase, it spontaneously and continuously reorganizes the spin-structure i.e. the system ages. Aging has a very good characteristic influence on the response function of spin-glass. Figure 1.18 shows result from an isothermal aging experiment on an Ising and a Heisenberg system [51]. A striking feature between the behaviors of the two systems is that aging has much larger influence on the relaxation of the Heisenberg system than the Ising system.

There are two main approaches to describe the spin-glass behavior; one is phase space (mean field) and another one is the real space (droplet scaling) model. The mean field model predicts a finite spin-glass temperature (e.g. T_{sg}) and also a persistence of the phase in an applied magnetic field, and the spin-glass and paramagnetic phases are separated by the Almeida-Thouless line [52]. On the other hand, the droplet scaling theory predicts that [53] in the thermodynamic limit, any finite magnetic field destroys the spin-glass phase. A crucial point in this model is the correspondence between the time and length scales. An experimental probe that measures at a certain frequency or time scale, can also probes the system on a length scale set by the observation time (and temperature). A finite field sets an upper limit to the correlation length scales in the spin-glass; on shorter length scales the system appears to be unaffected by the field, but on larger length scales the system will be at equilibrium (paramagnetic) state.

Therefore to establish the spin-glass behavior experimentally, the next question that arises, is what properties a system has in order to be a spin-glass? The defining

properties are i) frozen-in magnetic moments below some freezing temperature, T_{sg}, and hence a cusp in the ac-susceptibility below T_{sg}, ii) absence of periodic long-range magnetic ordering and iii) remanence and magnetic relaxation on macroscopic time scale below T_{sg}, at sufficiently low field. Of course, whether the moments are frozen-in or not, depends on the time scale of the observation. In low field dc-magnetization, the spin-glass transition, T_{sg}, is revealed by a maximum in the ZFC-magnetization, irreversibility between the ZFC and the FC-magnetization; and a continuous decay of the thermoremanent magnetization (TRM) to zero at the temperature where irreversibility between the ZFC and FC appears. An additional and remarkable feature of the non-equilibrium spin-glass phase is "memory" phenomena. This is revealed by measurements according to a standard ZFC-magnetization protocol [54]. The memory-aging behaviors are manifestations of some crucial concepts-aging, rejuvenation and chaos that characterize the spin-glass phase and are the key factors for modeling spin-glasses [51]. The frequency-dependent cusp was first reported in dilute metallic alloy of CuMn (with 0.9 % Mn) and thereafter in concentrated insulator $Eu_{1-x}Sr_xS$ [55]. In recent years, some of the perovskite manganates such as $(Tb_{0.33}La_{0.67})_{0.67}Ca_{0.33}MnO_3$, $Y_{0.7}Ca_{0.3}MnO_3$, and $Th_{0.35}Ba_{0.37}Ca_{0.28}MnO_3$ [56] are considered to exhibit spin-glass behavior at low temperatures. Recently, spin-glass behavior has been reported in an uranium based nonmagnetic atom disorder compound, U_2AuGa_3 [57]. Some of the manganates like $Nd_{0.7}Sr_{0.3}MnO_3$ and $La_{0.7-x}Y_xCa_{0.3}MnO_3$ [58] show magnetic relaxation phenomena in the FM phase indicating magnetic frustration and disorder.

There is another interesting and well known phenomenon of spin-glasses called re-entrant spin-glass transition, which occurs near the phase boundary between the spin-

glass and FM phase [48, 59]. This re-entrant spin-glass behavior is reported in $Y_{0.7}Ca_{0.3}MnO_3$ [54] and very recently in Mn-rich $YMnO_3$ hexagonal manganates [60]. Therefore a study of re-entrant spin-glass transition in a dilute magnet by Abiko et al [61] has established a theoretical model that settles the most important issue of the re-entrant spin-glass transition.

Rare earth cobaltate of the type $Ln_{1-x}A_xCoO_3$ are somewhat similar in physical properties to the manganates. The spin-glass behavior in $La_{1-x}Sr_xCoO_3$ has been reported by a few workers [62]. Similarly, Burley et al [63] have reported the long-range ferromagnetism and glassy behavior in $La_{1-x}Ca_xCoO_3$ cobaltates.

1.8 RARE EARTH COBALTATES

Rare earth cobaltates with the perovskite structures, $Ln_{1-x}A_xCoO_3$ (Ln = trivalent rare earth, A = divalent alkaline earth), have been investigated for several years due to their novel magnetic and electronic properties which include temperature-induced spin-state transitions, cluster-glass like behavior, insulator-metal transition and so on [63-67]. The temperature induced spin-state transition from low-spin (LS) to high-spin (HS) or intermediate-spin (IS) state is well known for $LaCoO_3$ [64, 65, 68]. Recently pressure-induced transition has also been reported in the literature for $LaCoO_3$ as well as for doped cobaltate [69]. The physical properties of perovskite cobaltates are sensitively dependent on the doping concentration of the rare-earth site. Doping brings up mixed valences in the Co-ions, similar to the Mn-ions in the manganates as discussed earlier. The substitution of A^{2+} for Ln^{3+} in $Ln_{1-x}A_xCoO_3$ series [70] will favor the Co^{3+} to transform into Co^{4+}, which will interact ferromagnetically obeying the Zener double-exchange mechanism. On

the other hand, Co^{3+}-Co^{3+} and Co^{4+}-Co^{4+} interacts antiferromagnetically due to super-exchange interactions. Hence, there will be always a competition between these two interactions to dominate one over another giving rise to a tendency of electronic phase separation in the system [67]. Whether the ferromagnetism in cobaltates (similar to manganates) is mediated by a DE mechanism or not is clearly not understood at present. However, the absence of half filled t_{2g} orbitals is providing core spin and strong Hund's rule coupling, unlike manganates, making this mechanism less feasible. Similar to the manganates, the JT distortion of the CoO_6 octahedra has been reported by Fauth et al [71]. The JT distortion favored due to the IS state of Co^{3+} ($t_{2g}^5 e_g^1$) and Co^{4+} ($t_{2g}^4 e_g^1$) ions occur in the cobalt structure.

The magnetic phase diagram of A-site doped cobaltates, $La_{1-x}Sr_xCoO_3$ is shown in Fig. 1.19, to illustrate the ferromagnetic T_C with doping concentration. There are two distinct regions in the phase diagram. For $x > 0.2$, one observes the onset of FM transition (denoted by T_C).

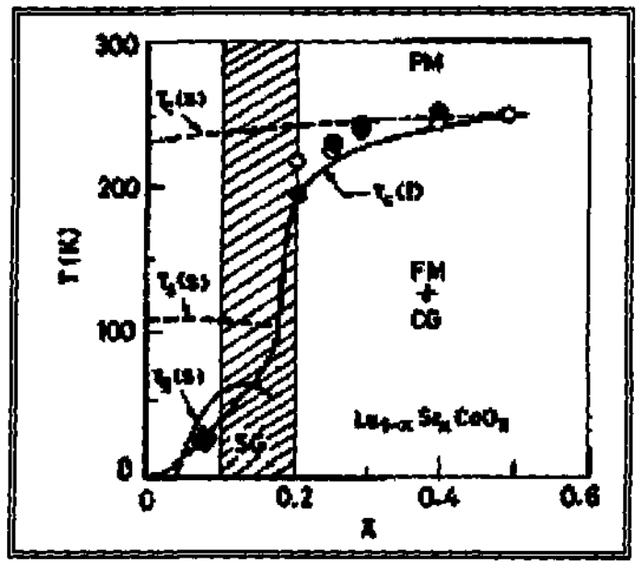

Figure 1.19 Magnetic phase diagram for $La_{1-x}Sr_xCoO_3$ [ref 26].

When $x < 0.1$, a spin-glass like phase is observed at lower temperatures, which has been discussed in details earlier. The value of MR even at T_C is much smaller in magnitude than the manganates. However, in the cobaltates large and negative MR has been reported in the insulating compositions. In such system, the maximum MR is observed where it shows SG-type behavior [26]. Recently, researchers have begun to take substantial interest in perovskite related phases containing the smaller rare earth ions of the type $Ln_{1-x}Sr_xCoO_3$ [72]. Rare earth cobaltates of the type $Ln_{1-x}Ca_xCoO_3$ shows no long-range ferromagnetism or insulator-metal transition, instead they exhibit electronic phase separation and/or glassy magnetic behavior at low temperatures [63, 73].

1.9 REFERENCES

1. G. H. Jonkar and J. H. Van Santen, Physica, **16**, 377 (1950); J. H. Van Santen and G. H. Jonkar, Physica, **16**, 599 (1950).
2. C. N. R. Rao, and B. Raveau (Eds), *Colossal Magnetoresistance, Charge Ordering and related properties of manganese Oxides* (World Scientific: Singapore, 1998); Y. Tokura (Eds), *Colossal Magnetoresistance Oxides* (London: Gorden and Breach, 1999).
3. E. Dagotto (Eds), *Nanoscale Phase Separation and Colossal Magnetoresistance* (Berlin: Springer, 2003); C. N. R. Rao, A. K. Kundu, M. M. Seikh and L. Sudheendra, Dalton Trans., **19**, 3003 (2004); V. B. Shenoy, D. D. Sarma and C. N. R. Rao, Chem. Phys. Chem., Preprint: to be published (2006).
4. A. P. Ramirez, J. Phys: Condens. Matter., **9**, 8171 (1997); E. Dagotto, T. Hotta and A. Moreo, Phys. Rep., **344**, 1 (2001); H. Y. Hwang, S. W. Cheong, P. G. Radaelli, M. Marezio and B. Batlogg, Phys. Rev. Lett., **75**, 914 (1995).
5. C. N. R. Rao and J. Gopalakrishnan (Eds), *New Directions in Solid State Chemistry*, 2nd edition (Cambridge University Press, 1997); C. N. R. Rao and B. Raveau (Eds), *Transition Metal Oxides: Structure, Properties and Synthesis of Ceramic Oxides*, 2nd edition (Wiley-VCH, 1998).
6. J. Kanamori, J. Phys.Chem. Solids, **10**, 87 (1959).
7. P. G. Radaelli, G. Iannone, M. Marezio, H. Y. Hwang, S. W. Cheong, J. D. Jorgensen, and D. N. Argyriou, Phys. Rev. B, **56**, 8265 (1997).

8. C. N. R. Rao, M. M. Seikh, and N. Chandrabhas, Top. Curr. Chem. **1**, 234 (2004).

9. R. H. Potze, G. A. Sawatzky and M. Abbate, Phys. Rev. B, **51**, 11501 (1995); M. A. Korotin, S. Yu. Ezhov, I. V. Solovyev, V. I. Anisimov, D. I. Khomskii, and G. A. Sawatzky, Phys. Rev. B, **54**, 5309 (1996); J. Wang, Z. D. Wang, W. Zhang, and D. Y. Xing, Phys. Rev. B, **66**, 064406 (2002); M. M. Seikh, Ph. D thesis, Indian Institute of Science, Bangalore (2005).

10. E. O. Wollan and W. C. Koehler, Phys. Rev., **100**, 545 (1955); W. C. Koehler and E. O. Wollan, J. Phys. Chem. Solid, **2**, 100, (1957).

11. J. B. A. A. Elemans, B. Van Laar, K. R. Van Der Veen and B. O. Loopstra, J. Solid State Chem., **3**, 238 (1971); R. Mahendiran, S. K. Tiwary, A. K. Raychaudhuri, T. V. Ramakrishnan, R. Mahesh, N. Rangavittal, and C. N. R. Rao, Phys. Rev. B, **53**, 3348 (1996); Y. Tokura and N. Nagaosa, Science, **288**, 462, (2000).

12. C. Zener, Phys. Rev., **81**, 440 (1951); C. Zener, Phys. Rev., **82**, 403 (1951); A. J. Millis, P. B. Littlewood and B. I. Shraiman, Phys. Rev. Lett., **74**, 5144 (1995); A. J. Millis, J. Appl. Phys., **81**, 5502 (1997).

13. J. B. Goodenough, Progress in Solid State Chem., **5**, 145 (1971); H. A. Kramers, Physica, **1**, 191 (1934).

14. M. A. Ruderman and C. Kittel , Phys. Rev. **96**, 99 (1954); T. Kasuya, Prog. Theor. Phys. **16**, 45 (1956); K. Yoshida, Phys. Rev. **106**, 893 (1957); P. W. Anderson and H. Hesegawa, Phys. Rev., **100**, 675 (1955); J. B. Goodenough, Phys. Rev.,

100, 564 (1955); J. B. Goodenough, Phys. Rev., **124**, 373 (1961); J. Kanamori, J. Phys. Chem. Solids, **10**, 87 (1959).

15. P. de Gennes, Phys. Rev., **118**, 141 (1960).

16. N. F. Mott, *Metal-Insulator Transitions* (Taylor and Francis, London, 1990); B. I. Shklovskii and A. L. Efros, *Electronic Properties of Doped Semiconductors* (Springer, Berlin, 1984).

17. M. N. Baibich, J. M. Broto, A. Fert, F. Nguyen Van Dau, F. Petroff, P. Etienne, G. Creuzet, A. Friederich, and J. Chazelas, Phys. Rev. Lett., **61**, 2472 (1988).

18. R. M. Kusters, J. Singleton, D. A. Keen, R. McGreevy, and W. Hayes, Physica B, **155**, 362 (1989).

19. R. von Helmolt, J. Wecker, B. Holzapfel, L. Schultz, and K. Samwer, Phys. Rev. Lett., **71**, 2331 (1993); K. Chahara, T. Ohno, M. Kasai, and Y. Kozono, Appl. Phys. Lett., **63**, 1990, (1990); S. Jin, T. H. Tiefel, M. McCormack, R. A. Fastnacht, R. Ramesh, and L. H. Chen, Science, **264**, 413, (1994); S. Jin, H. M. O. Bryan, T. H. Tiefel, M. McCormack, and W. W. Rhodes, Appl. Phys. Lett., **66**, 382, (1995); A. Urushibara, Y. Moritomo, T. Arima, A. Asamitsu, G. Kido, and Y. Tokura, Phys. Rev. B, **51**, 14103 (1995).

20. P. M. Levy, Solid State Phys., **47**, 367 (1994); P. M. Levy and S Zhang, J. Magn. Magn. Mater., **151**, 315, (1995).

21. P. Schiffer, A. P. Ramirez, W. Bao, and S. W. Cheong, Phys. Rev. Lett., **75**, 3336 (1995).

22. A. Arulraj, R. Mahesh, G. N. Subbanna, R. Mahendiran, A. K. Raychaudhuri and C. N. R. Rao, J. Solid State Chem., **127**, 87 (1996).

23. Y. Moritomo, A. Asamitu, H. Kuwahara, and Y. Tokura, Nature, **380**, 141, (1996); R. Mahesh, R. Mahendiran, A. K. Raychaudhuri and C. N. R. Rao, J. Solid State Chem., **122**, 448 (1996).

24. K. I. Kobayashi, T. Kimura, H. Sawada, K. Terakura and Y. Tokura, Nature, **395**, 677, (1998).

25. M. A. Subhramanian, B. H. Toby, A. P. Ramirez, W. J. Marshall, A. W. Sleight, and G. H. Kwei, Science, **273**, 81, (1996).

26. R. Mahendiran, A. K Raychaudhuri, A. Chainani and D. D. Sarma, J. Phys.: Condens. Mater., **7**, L561, (1995); R. Mahendiran and A. K. Raychaudhuri, Phys. Rev. B, **54**, 16044 (1996).

27. C. Martin, A. Maignan, D. Pelloquin, N. Nguyen, and B. Raveau, Appl. Phys. Lett., **71**, 1421, (1997).

28. C. N. R. Rao, J. Phys. Chem. B, **104**, 5877 (2000).

29. E. J. W. Verway, Nature, **144**, 327 (1939).

30. Y. Tokura, Y. Tomioka, H. Kuwahara, A. Asamitsu, Y. Moritomo and M. Kasai, J. Appl. Phys., **79**, 5288, (1996).

31. H. Kuwahara, Y. Tomioka, A. Asamitgu, Y. Moritomo and Y. Tokura, Science, **270**, 961 (1995).

32. Y. Tomioka, A. Asamitsu, H. Kuwahara, Y. Moritomo and Y. Tokura, Phys. Rev. B, **53**, 1689 (1996).

33. C. N. R. Rao, P. N. Santosh, R. S. Singh and A. Arulraj, J. Solid. State. Chem., **135**, 169 (1998); Y. Moritomo, H. Kuwahara, Y. Tomioka and Tokura, Phys. Rev. B, **55**, 7549 (1997).

34. C. N. R. Rao, A. Arulraj, P. N. Santosh, and A. K. Cheetham, Chem. Mat., **10**, 2714 (1998); P. M. Woodward, T. Vogt, D. E. Cox, A. Arulraj, C. N. R. Rao, P. Karen and A. K. Cheetam,, Chem. Mat., **10**, 3652, (1998); A. Arulraj, P. N. Santhosh, R. S. Gopalan, A. Guha, A. K. Raychaudhuri, N. Kumar and C. N. R. Rao, J. Phys.: Condens. Mater., **10**, 8497, (1998).

35. N. Kumar and C. N. R. Rao, J. Solid State Chem., **129**, 363 (1997).

36. D. E. Cox, P. G. Radaelli, M. Marezio, and S.W. Cheong, Phys. Rev. B, **57**, 3305 (1998).

37. A. Arulraj, A. Biswas, A. K. Roychaudhuri, C. N. R. Rao, P. M. Woodward, T. Vogt, D. E. Cox and A. K. Cheetham, Phys. Rev. B, **57**, R8115 (1996).

38. M. Uehara, S. Mori, C. H. Chen, and S. W. Cheong, Nature, **399**, 560 (1999); L. Sudheendra and C. N. R. Rao, J. Phys.: Condens. Mater., **15**, 3029, (2003).

39. L. M. Rodriguez-Martinez and J. P. Attfield, Phys. Rev. B, **54**, R15622 (1996).

40. P. V. Vanitha and C. N. R. Rao, J. Phys.: Condens. Mater., **13**, 11707, (2003); P. V. Vanitha, A. Arulraj, P. N. Santosh and C. N. R. Rao, Chem. Mater., **12**, 1666 (2000).

41. C. N. R. Rao, P. V. Vanitha and A. K. Cheetham, Chem. Euro. J., **9**, 829 (2003); C. N. R. Rao and P. V. Vanitha, Curr. Opinion Solid State Mater. Sci., **6**, 97 (2002).

42. A. Moreo, S. Yunoki and E. Dagotto, Science, **283**, 2034 (1999).

43. V. Podzorov, M. Uehara, M. E. Gershenson, T. Y. Koo and S. W. Cheong, Phys. Rev. B, **61**, R3784 (2000).

44. Ch. Ranner, G. Aeppli, B. G. Kim, Y. A. Soh and S. W. Cheong, Nature, **416**, 518 (2002).

45. P. M. Woodward, D. E. Cox, T. Vogt, C. N. R. Rao and A. K. Cheetham, Chem. Mat., **11**, 3528 (1999).

46. J. Wu, J. W. Lynn, C. J. Glinka, J. Burley, H. Zheng, J. F. Mitchell, and C. Leighton, Phys. Rev. Lett. **94**, 037201 (2005).

47. V. Cannella and J. A. Mydosh, Phys. Rev. B, **6**, 4220 (1972); D. Sherrington and Kirkpatrick, Phys. Rev. Lett., **35**, 1792 (1975).

48. L. Lundgren, P. Svedlindh, P. Nordblad, and O. Beckman, Phys. Rev. Lett., **51**, 911 (1983); K. Binder and A. P. Young, Rev. Mod. Phys., **58**, 801 (1986); J.A. Mydosh, *"Spin Glasses: An Experimental Introduction"* (Taylor and Francis, London, 1993);

49. G. Toulose, Commun. Phys., **2**, 115, (1977).

50. P. Nordblad, J. Phys.: Condens. Mater., **16**, S715 (2004).

51. P. Jonsson, R. Mathieu, P. Nordblad, H. Yoshino, H. A. Katori and A. Ito, Phys. Rev. B, **70**, 174402 (2004).

52. J. R. L de Almeida and D. J. Thouless, J. Phys. A: Math. Gen., **11**, 983, (1978).

53. D. S. Fisher and D. A. Huse, Phys. Rev. Lett., **56**, 1601 (1986).

54. R. Mathieu, P. Jonsson, D. N. H. Nam, and P. Nordblad, Phys. Rev. B **63**, 092401 (2001); R. Mathieu, P. Nordblad, D. N. H. Nam, N. X. Phuc, and N. V. Khiem, Phys. Rev. B **63**, 174405 (2001).

55. F. Maletta and W. Felsch, Phys. Rev. B, **20**, 1245 (1979).

56. J. M. De Teresa, M. R. Ibarra, J. García, J. Blasco, C. Ritter, P. A. Algarabel, C. Marquina, and A. del Moral, Phys. Rev. Lett., **76**, 3392 (1996); D. Sedmidubsky, J. Hejtmanek, M. Marysko, Z. Jirak, V. Hardy and C. Martin, J. Appl. Phys. **91**, 8260 (2001).

57. D. X. Li, T. Yamamura, S. Nimori, K. Yubuta, and Y. Shiokawa, Appl. Phys. Lett., **87**, 142505 (2005).

58. D. N. H. Nam, R. Mathieu, P. Nordblad, N. V. Khiem, and N. X. Phuc, Phys. Rev. B **62**, 1027 (2000); R. S. Freitas, L. Ghivelder, F. Damay, F. Dias, and L. F. Cohen, Phys. Rev. B **64**, 144404 (2001).

59. B. H. Verbeek, G. J. Nieuwenhuys, H. Stocker, and J. A. Mydosh, Phys. Rev. Lett., **40**, 586 (1978).

60. W. R. Chen, F. C. Zhang, J. Miao, B. Xu, X. L. Dong, L. X. Cao, X. G. Qiu, B. R. Zhao and P. Dai, Appl. Phys. Lett., **87**, 042508, (2005).

61. S. Abiko, S. Niidera, and F. Matsubara, Phys. Rev. Lett., **94**, 227202 (2005).

62. M. Itoh, I. Natori, S. Kubota, and K. Matoya, J. Phys. Soc. Japan **63**, 1486 (1994); D. N. H. Nam, K. Jonason, P. Nordblad, N. V. Khiem, and N. X. Phuc, Phys. Rev. B **59**, 4189 (1999); J. Wu, and C. Leighton, Phys. Rev. B **67**, 174408 (2003).

63. J. C. Burley, J. F. Mitchell, and S. Short, Phys. Rev. B **69**, 054401 (2004).

64. M. A. Senaris-Rodriguez, and J. B. Goodenough, J. Solid State Chem. **118**, 323 (1995).

65. T. Saitoh, T. Mizokawa, A. Fujimori, M. Abbate, Y. Takeda and M. Takano, Phys. Rev. B **56**, 1290 (1997).

66. P. L. Kuhns, M. J. R. Hoch, W.G. Moulton, A. P. Reyes, J. Wu, and C. Leighton Phys. Rev. Lett. **91**, 127202 (2003).

67. J. Wu, J. W. Lynn, C. J. Glinka, J. Burley, H. Zheng, J. F. Mitchell, and C. Leighton, Phys. Rev. Lett. **94**, 037201 (2005).

68. Y. Kobayashi, N. Fujiwara, S. Murata, K. Asai, and H. Yasuoka, Phys. Rev. B **62**, 410 (2000); C. N. R. Rao, M. M. Seikh, and N. Chandrabhas, Top. Curr. Chem. **1**, 234 (2004).

69. T. Vogt, J. A. Hriljac, N. C. Hyatt, and P. Woodward, Phys. Rev. B **67**, R140401 (2003); I. Fita, R. Szymczak, R. Puzniak, I. O. Troyanchuk, J. F. Finowicki, V. N. Varyukhin, and H. Szymczak, Phys. Rev. B **71**, 214404 (2005).

70. H. Taguchi, H. Shimada, and M. Koizumi, J. Solid State Chem. **41**, 329 (1982); S. Tsubouchi, T. Kyomen, M. Itoh, and M. Oguni, Phys. Rev. B **69**, 144406 (2004).

71. F. Fauth, E. Suard, and V. Caignert, Phys. Rev. B **65**, 060401 (2002).

72. K. H. Ryu, K. S. Roh, S. J. Lee, C. H. Yo, J. Solid State Chem. **105**, 550 (1993); B. Raveau, V. Pralong, V. Caignaert, M. Hervieu, A. Maignan, J. Phys.: Condens. Matter, **17**, 7371 (2005); R. L. Withers, M. James and D. J. Goossens, J. Solid State Chem. **174**, 198 (2003); M. James, D. Cassidy, D. J. Goossens and R. L. Withers, J. Solid State Chem. **177**, 1886 (2004).

73. H. Masuda, T. Fujita, T. Miyashita, M. Soda, Y. Yasui, Y. Kobayashi and M. Sato, J. Phys. Soc. Japan, **72**, 873 (2003).

2. ELECTRONIC PHASE SEPARATION IN RARE EARTH MANGANATES ($Ln_{1-x}A_xMnO_3$)

SUMMARY*

Rare earth manganates of the general formula $Ln_{1-x}A_xMnO_3$ (Ln = trivalent rare earth, A = divalent alkaline earth) have attracted considerable interest because of their fascinating physical properties. Electronic and magnetic properties of four series of rare earth manganates of the general formula $La_{0.7-x}Ln_xBa_{0.3}MnO_3$ (Ln = Pr, Nd, Gd and Dy) have been investigated to examine the effect of large size-disorder (σ^2) in a system where the average radius of the A-site cations, $\langle r_A \rangle$, remains high (1.216 -1.292 Å) and the Mn^{3+}/ Mn^{4+} ratio is kept constant. The size-disorder, as measured by the σ^2 parameter, has been varied over a wide range of 0.001 and 0.030 $Å^2$. As *x* is increased, the materials exhibit a decrease in the ferromagnetic (FM) T_C or lose ferromagnetism entirely. This is accompanied by an insulator-metal (I-M) transition, with the T_{IM} decreasing with increasing *x*, or an entirely insulating behavior. The insulating behavior and loss of ferromagnetism occurs when σ^2 is close to 0.02 $Å^2$. Thus, in the manganates series Ln = Gd and Dy, the non-magnetic insulating behavior occurs at *x* values of 0.5 and 0.3 respectively. Where an I - M transition with $T_{IM} < T_C$ indicates the presence of a FM-

*Based on these studies, papers have been published in: Solid State Comm. **125** 41 (2003), J. Phys.: Condens. Matter **17** 4171 (2005), J. Phys.: Condens. Matter **18** 4809 (2006).

insulating regime. The absence of long-range ferromagnetism in some of the compositions is accompanied by the divergence between the zero-field-cooled (ZFC) and the field-cooled (FC) magnetization data. The FM or non-magnetic insulating state is due to phase separation wherein FM clusters are present in an insulating matrix. The non-magnetic insulating compositions can be rendered FM and metallic by decreasing σ^2 while keeping $\langle r_A \rangle$ constant. This extraordinary effect of σ^2 on the properties of the rare earth manganates is noteworthy.

While $La_{0.7}Ba_{0.3}MnO_3$ is a FM metal (T_C = 340 K) with long-range ordering, $Nd_{0.7}Ba_{0.3}MnO_3$ shows a transition around 150 K with a small increase in magnetization, but remains an insulator at all temperatures. $Gd_{0.7}Ba_{0.3}MnO_3$ is non-magnetic and insulating at all temperatures. Thus, $Nd_{0.7}Ba_{0.3}MnO_3$ and $Gd_{0.7}Ba_{0.3}MnO_3$ represent insulators which are formally magnetic and non-magnetic respectively. Low-field dc magnetization and ac susceptibility measurements on $Nd_{0.7}Ba_{0.3}MnO_3$ reveal the presence of a transition around 150 K, and a complex behavior with different ordering/freezing transitions at 62, 46 and 36 K in the case of $Gd_{0.7}Ba_{0.3}MnO_3$, the last one being more prominent. The nature of the field-dependence of the magnetization combined with the slow magnetic relaxation, aging and memory effects suggest that $Nd_{0.7}Ba_{0.3}MnO_3$ is a cluster-glass below 150 K, a situation similar to that found in $La_{1-x}Sr_xCoO_3$. $Gd_{0.7}Ba_{0.3}MnO_3$, however, shows non-equilibrium dynamics characteristic of spin-glasses, below 36 K. The difference in the nature of the glassy behavior between $Gd_{0.7}Ba_{0.3}MnO_3$ and $Nd_{0.7}Ba_{0.3}MnO_3$ probably arises because of the larger disorder arising from the mismatch between the sizes of the A-site cations in the former. The disorder, in turn, promotes electronic phase separation. Furthermore, our results on $Nd_{0.7}Ba_{0.3}MnO_3$ and

$Gd_{0.7}Ba_{0.3}MnO_3$ suggest that the magnetic insulating states often reported in the rare earth manganates of the type $Ln_{1-x}A_xMnO_3$ are likely to be associated with glassy magnetic behavior.

Some of the compositions of the half-doped rare earth manganates of the type, $La_{0.5-x}Ln_xCa_{0.5}MnO_3$ (Ln = Pr, Nd) and $Nd_{0.5}Ca_{0.5-x}Sr_xMnO_3$ with relatively small A-site cation radius, $\langle r_A \rangle$, show an unusual behavior, wherein they become FM on cooling the charge-ordered (CO) state (charge-ordering temperature T_{CO} > ferromagnetic transition temperature T_C). With increase in $\langle r_A \rangle$, however, the T_C becomes greater than T_{CO}. Thus, plots of T_C and T_{CO} against $\langle r_A \rangle$ for $La_{0.5-x}Ln_xCa_{0.5}MnO_3$ (Ln = Pr, Nd) and $Nd_{0.5}Ca_{0.5-x}Sr_xMnO_3$ show cross-over from the $T_{CO} > T_C$ regime to the $T_C > T_{CO}$ regime around $\langle r_A \rangle$ values of 1.195 ± 0.003 Å and 1.200 ± 0.005 Å, respectively. Between T_C and T_{CO}, the CO and FM phases are likely to coexist. In $Nd_{0.5}Ca_{0.5}Mn_{1-x}M_xO_3$ (M = Cr, Ru), $T_{CO} > T_C$ when $x \leq 0.10$, suggesting the re-entrant nature of the FM transition. The reentrant transition is a result of electronic phase separation and accordingly in the temperature range between T_{CO} and T_C, the CO and FM phases coexist.

2.1 INTRODUCTION

Electronic phase separation (EPS) in metal oxides has emerged to become a phenomenon of importance, because of the diversity of properties found in rare earth manganates of the type $Ln_{1-x}A_xMnO_3$ [1-4]. EPS gives rise to a variety of effects resulting in unusual magnetic and electron transport properties depending on x or the carrier concentration as well as the relative size of *Ln* and *A* ions. At relatively small carrier concentration, the high-conducting ferromagnetic (FM) region form separate droplets inside the insulating antiferromagnetic (AFM) matrix. In this case, concentration of the charge carriers in a portion of the crystal, when they cause appearance of the FM metallic and /or AFM insulating states, leads to the mutual charging of both phases (due to comparable energies of the states). We have seen in first chapter few possible scenarios of phase separation schematically and it is also evident from previous discussion that the different phases in rare earth manganates are governed by some external and internal factors. These factors can be induce different phases under one condition, such as temperature or pressure etc. As the different phases are separated from each other by the insulating regions, the crystal as a whole is an insulator at low temperature. Thus, FM clusters present randomly in an AFM host matrix often give rise to a glassy magnetic behavior. As the FM clusters grows in size to become reasonably size domains, due to the effect of temperature, composition or some other factors, the system acquires the characteristics of a genuine phase separated system. On increasing the temperature, the phase-separated state should be broken, and the impurity distribution over the crystal

should become uniform. These scenarios roughly represent the experimental observations and therefore EPS has been observed recently in real space with atomic scale resolution [1]. The coexistence of the different types of electronic phases in $La_{1-x}A_xMnO_3$ at various doping levels has been studied by various experimental techniques, which depends on the length scale [1-3]. Several recent papers on rare earth manganates reveal that in addition to microscopic phase separation, there can be macroscopic phase separation where the length scale is between 3-200 nm [2, 4, 5]. Structural and magnetic information from X-ray and neutron diffraction bear signatures of EPS, when the length scale is large (few hundred of nanometers). Evidence of phase separation is also obtained from magnetization and electron transport measurements, which has been used in our present study. Our investigations on rare earth manganates have shown the occurrence of EPS as well as disordered and frustrated ferromagnetic behavior for large A-site cations. Direct observational evidence is provided by images employing transmission electron microscopy, scanning probe microscopy and photo-emission spectroscopy. The phase separation reported by Uehara et al [5] was considered as disorder induced phase separation, rather than EPS, which was verified by Moreo et al [6]. The size of the clusters depends on the magnitude of the disorder. The smaller the disorder, larger would be the size of FM clusters. There are several reports on the EPS in the literature by different researchers [1, 7-9]. All these results are compatible with the theoretical model [6, 10]. These studies suggest that the EPS could also be the reason behind the large CMR effect in the rare earth manganates. The electronic phase separation scenario bridges the gap between the Zener double exchange model and the lattice distortion models.

2.2 SCOPE OF THE PRESENT INVESTIGATIONS

The scope of the investigations carried out on rare earth manganates is presented in this section. Novel effects of cation size-disorder, electronic phase separation and related aspects of the hole-doped rare earth manganates have been studied. We have also probed the re-entrant ferromagnetic transition in rare earth manganates with relatively small size A-site cations, arising from electronic phase separation.

2.2.1 Novel effects of size-disorder on the electronic and magnetic properties of rare earth manganates $La_{0.7-x}Ln_xBa_{0.3}MnO_3$ (Ln =Pr, Nd, Gd and Dy) with large $\langle r_A \rangle$

Among the several novel properties exhibited by the rare earth manganates, charge ordering and electronic phase separation are of particular interest [1, 11-14, 15-17]. Both these properties are highly sensitive to the $\langle r_A \rangle$, and the disorder arising from the size mismatch between the A-site cations [14, 17-20]. A detailed study of several compositions of $La_{0.7-x}Ln_xCa_{0.3}MnO_3$ series of manganates has shown the occurrence of electronic phase separation above a critical composition x_c [5, 19]. In this series of manganates, $\langle r_A \rangle$ decreases markedly with increase in x, accompanied by an increase in size-disorder. Above x_c, the materials become insulating and do not show ferromagnetism. The x_c value corresponds to the critical $\langle r_A \rangle$ value, $\langle r_A^c \rangle$, of 1.18 Å. Electronic phase separation occurs in the region of $\langle r_A^c \rangle$ [5, 19]. In order to fully appreciate the effect of the size mismatch between A-site cations, we considered it important to investigate a series of manganates, where the $\langle r_A \rangle$ remains substantially large and well above the $\langle r_A^c \rangle$

throughout the series. However, in this series the size-disorder increases significantly. $La_{0.7}Ba_{0.3}MnO_3$ with $\langle r_A \rangle$ of 1.292 Å is a good FM metal with a FM transition temperature, T_C, of around 350 K [21]. However, the T_C is lower than the value expected on the basis of the large A-site cation radius, because of the mismatch between the A-site cations [16-20]. Thus, the size disorder, σ^2, (see page 27 for definition of σ^2) is quite large, the value being 0.014 $Å^2$. $Pr_{0.7}Ba_{0.3}MnO_3$ [21, 22] with a $\langle r_A \rangle$ of 1.266 Å and σ^2 of 0.018 $Å^2$, shows a distinct FM transition around 190 K due to long-range FM ordering and an insulator-metal (I-M) transition at a lower temperature (155 K). The properties of $Nd_{0.7}Ba_{0.3}MnO_3$ with a $\langle r_A \rangle$ of 1.255 Å and σ^2 of 0.020 $Å^2$, however, appear to be quite different with an unusual insulating behavior [23]. We have investigated the effect of substitution of La in $La_{0.7}Ba_{0.3}MnO_3$ by the smaller rare earth ions Pr, Nd, Gd and Dy, on the magnetic and electron transport properties, to understand the evolution of the insulating behavior accompanying the disappearance of ferromagnetism, primarily arising from size-disorder. It is to be noted that in a given series of manganates, the size-disorder increases considerably with x, although the $\langle r_A \rangle$ remains in the range of 1.216 - 1.292 Å, and the carrier concentration i.e. the Mn^{3+}/Mn^{4+} ratio is constant. In order to evaluate the effect of size-disorder quantitatively, we have varied σ^2 in two series of manganates of the type $Ln_{0.7-x}Ln'_xA_{0.3-y}A'_yMnO_3$, wherein $\langle r_A \rangle$ is kept constant at 1.266 and 1.216 Å, corresponding to the $\langle r_A \rangle$ of $Pr_{0.7}Ba_{0.3}MnO_3$ and $Gd_{0.7}Ba_{0.3}MnO_3$ respectively.

2.2.2 Glassy behavior in the ferromagnetic and the non-magnetic insulating states of the rare earth manganates, $Ln_{0.7}Ba_{0.3}MnO_3$ (Ln = Nd and Gd)

As discussed in preceding section, in $La_{0.7-x}Ln_xCa_{0.3}MnO_3$ series of manganates, electronic phase separation is found to occur above a critical composition x_c, specially in

the regime when $\langle r_A \rangle$ is close to 1.18 Å or lower and favored by large size-disorder [18, 20]. In this system, $\langle r_A \rangle$ decreases with increasing x affecting the e_g bandwidth. A study of $La_{0.250}Pr_{0.375}Ca_{0.375}MnO_3$ by Deac et al [24] have shown that two types of magnetic relaxation, one at low fields associated with the reorientation of FM domains and another at higher fields due to the transformation between FM and non-FM phases. The presence of FM-clusters and associated magnetic relaxation phenomena well below T_C has been reported in $La_{0.7-x}Y_xCa_{0.3}MnO_3$ by Freitas et al [25]. $Nd_{0.7}Sr_{0.3}MnO_3$ with a well defined FM transition T_C exhibits aging phenomena in the FM phase indicating magnetic frustration and disorder [26]. Lopez et al [27] have provided evidence for two competing magnetic phases in $La_{0.5}Ca_{0.5}MnO_3$ based on the magnetic relaxation study. Previous investigations of the magnetic and electron transport properties of $La_{0.7-x}Ln_xBa_{0.3}MnO_3$ (Ln = Pr, Nd, and Gd) where the $\langle r_A \rangle$ remains relatively large over the entire range of compositions ($\geq$ 1.216 Å) have shown that the FM or non-magnetic insulating compositions can be rendered to FM and metallic by decreasing the size-disorder. An insulating FM state is found in $Nd_{0.7}Ba_{0.3}MnO_3$, but $Gd_{0.7}Ba_{0.3}MnO_3$ is insulating and non-magnetic down to low temperatures, although the carrier concentration (Mn^{3+}/Mn^{4+} ratio) is the same as in $La_{0.7}Ba_{0.3}MnO_3$ which is a genuine FM metal [23, 28]. In this investigation we focus our interest on $Nd_{0.7}Ba_{0.3}MnO_3$ and $Gd_{0.7}Ba_{0.3}MnO_3$ and have carried out a detailed study of the magnetic properties by employing measurements of low-field dc magnetization, ac susceptibility, magnetic-relaxation and memory effects. The study has revealed the presence of glassy magnetic phases in both these manganates, albeit of different varieties.

2.2.3 Occurrence of re-entrant FM transitions in rare-earth manganates on cooling the charge-ordered states: A consequence of electronic phase separation

There have been extensive investigations on rare earth manganates of the general formula $Ln_{1-x}A_xMnO_3$ (Ln = trivalent rare earth, A = divalent alkaline earth) over the last few years in order to understand the various phenomena and properties exhibited by them [1, 11, 13, 14, 29]. In particular, the competition between charge ordering and charge delocalization has received much attention. Charge ordering is specially favored in the manganates when the average radius of the A-site cations, $\langle r_A \rangle$ is relatively small [14]. Charge ordering is destroyed by the application of magnetic field or by the substitution of certain cations in the B-site, provided the $\langle r_A \rangle$ is sufficiently large ($\langle r_A \rangle \geq 1.17$Å) [30-32]. If $\langle r_A \rangle$ is very small, such external factors have little effect on the charge ordering. The $\langle r_A \rangle$ regime of 1.17-1.20 Å is especially interesting. In this regime the manganates show charge ordering near the room temperature and undergo a re-entrant transition to a FM state on cooling ($T_C < T_{CO}$). Thus, $Nd_{0.5}Ca_{0.5}MnO_3$ ($\langle r_A \rangle$ = 1.17Å) is a charge ordered insulator (T_{CO} = 240 K) and does not show ferromagnetism at any temperature [33]. $Nd_{0.25}La_{0.25}Ca_{0.5}MnO_3$ ($\langle r_A \rangle$ = 1.185Å), shows charge ordering at 239 K and undergoes a FM transition on cooling to ~140 K [34]. By contrast, $La_{0.5}Ca_{0.5}MnO_3$ with a $\langle r_A \rangle$ of 1.198 Å has a FM Curie temperature, T_C, of 225 K and T_{CO} = 135 K [2]. In the intermediate temperature range between T_C and T_{CO}, these compositions show the coexistence of phases.

Investigations of the manganates $La_{0.5-x}Ln_xCa_{0.5}MnO_3$ (Ln = Pr, Nd) in the $\langle r_A \rangle$ region of 1.17-1.20 Å showed that the T_C increases while T_{CO} decreases with increase in $\langle r_A \rangle$. The cross over between T_C and T_{CO} takes place around $\langle r_A \rangle = 1.195 \pm 0.003$Å [36].

While this is an interesting observation, there are very few experimental points in the region around 1.195Å. We have, therefore examined the manganates of the type $La_{0.5-x}Ln_xCa_{0.5}MnO_3$ (Ln = Pr, Nd) in the $\langle r_A \rangle$ region of 1.194 - 1.197Å. We also considered it important to explore whether a series of manganates obtained by substitution of Ca by Sr in $Nd_{0.5}Ca_{0.5}MnO_3$ would exhibit such re-entrant transition and if so how the T_C and T_{CO} will vary with $\langle r_A \rangle$. We have investigated the series of compositions $Nd_{0.5}Ca_{0.5-x}Sr_xMnO_3$ for this purpose. It may be noted that earlier studies of this system of manganates have not paid attention to the re-entrant transition and relative values of T_C and T_{CO} [33]. The present study shows that there is indeed a re-entrant transition with $T_{CO} > T_C$ and that the curve T_{CO} - $\langle r_A \rangle$ and T_C - $\langle r_A \rangle$ curves intersect around a $\langle r_A \rangle$ value of 1.200 ± 0.005 Å in $Nd_{0.5}Ca_{0.5-x}Sr_xMnO_3$. An examination of the available data on $Nd_{0.5}Ca_{0.5}Mn_{1-x}M_xO_3$ (M = Cr, Ru), shows that $T_{CO} > T_C$ in these manganates as well, with a cross over around same value of dopant concentration, although $\langle r_A \rangle$ remains constant. Between T_{CO} and T_C, the manganates are phase-separated showing the presence of both CO and FM phases.

2.3 EXPERIMENTAL PROCEDURES

2.3.1 Synthesis of samples

Polycrystalline samples of the respective compositions were prepared by the conventional ceramic method. This method depends on the inter-diffusion between the rare earth and transition metal oxide powders and therefore it becomes necessary to use fine powders. The reaction also depends upon a few parameters, among them the most important being the diffusion length. In order to favor diffusion and obtain single phase compounds, we have to keep the reaction sintering temperature high so that the diffusion length 'l' exceeds the particle size, which is given by $l = \sqrt{(2kt)}$, where, k = diffusion rate constant and t = sintering time. These parameters depend on the respective precursor materials [38].

Rare earth manganates were prepared by starting with a stoichiometric mixture of rare earth oxide with respective alkaline earth carbonate and transition metal oxide thoroughly mixed in an agate mortar with propanol and milled for few hours. After the powder mixed homogenously and dried, the mixture transferred to an alumina/platinum crucible and preheated to 1173-1373 K for 12-24 h with repeated intermediate grindings [39]. The preheated sample was then ground thoroughly and palletized under a constant pressure of 50-60 kN in a steel dye. The pellets were then transferred into platinum boat and finally sintered at 1473-1673 K for 24 h at different atmosphere, which depends upon the precursor materials as discussed below.

(i) Preparation of $La_{0.7-x}Ln_xBa_{0.3}MnO_3$ (Ln = Pr, Nd, Gd and Dy)

Polycrystalline samples of $La_{0.7-x}Ln_xBa_{0.3}MnO_3$ (Ln = Pr, Nd, Gd and Dy) were prepared by the solid state reaction method. Stoichiometric mixtures of the respective rare earth oxides, $BaCO_3$ and MnO_2 were weighed in the desired proportions and milled for few hours with propanol. The mixtures were dried, and calcined in air at 1223 K followed by heating at 1273 K and 1373 K for 12 h in air. The powders thus obtained were pelletized and the pellets were sintered at 1673 K for 24 h in air. Two series of manganates of the general formula $Ln_{0.7-x}Ln'_xA_{0.3-y}A'_yMnO_3$, with fixed $\langle r_A \rangle$ values of 1.266 and 1.216 Å were prepared by the same method.

(ii) Preparation of $La_{0.5-x}Ln_xCa_{0.5}MnO_3$ (Ln = Pr, Nd) and $Nd_{0.5}Ca_{0.5-x}Sr_xMnO_3$

Polycrystalline samples of $La_{0.5-x}Nd_xCa_{0.5}MnO_3$, $La_{0.5-x}Pr_xCa_{0.5}MnO_3$ and $Nd_{0.5}Ca_{0.5-x}Sr_xMnO_3$ were prepared by the solid state reactions method. Stoichiometric mixtures of the respective rare earth oxides, alkaline earth carbonates and MnO_2 were ground and heated at 1173 K in air followed by heating at 1273 and 1473 K for 12 h in air. The powders thus obtained were pelletized and the pellets sintered at 1673 K for 12 h in air. To improve the oxygen stoichiometry the samples were annealed in oxygen at 1173 K.

2.3.2 Characterization

(a) Powder X-ray diffraction (XRD)

The phase purity of the polycrystalline samples was established by recording the X-ray diffraction patterns using a Seiferts 3000 TT diffractometer. The data were recorded in the 2θ range of 10°-90° using Cu-Kα radiation (1.5406 Å). The lattice

parameters were calculated from the XRD patterns using PROSZKI and CELREF-software packages.

(b) Composition analysis

The composition analysis of the powder sample was carried out by Energy Dispersive X-ray (EDX) analysis using a LEICA S440I scanning electron microscope fitted with a Si-Li detector. The oxygen stoichiometry was determined by iodometric titrations [40]. The error in oxygen content estimation was within ± 0.02.

(c) Resistivity measurements

The electrical resistivity measurements were carried out by standard four-probe method. The samples were mounted on a copper head using insulating tape and the contacts between the samples and the copper wires were made by silver epoxy which acts as electrode. The measurements were carried out in constant current mode in the temperature range of 20-320 K.

(d) Magnetization measurements

The magnetic properties of the samples were investigated by using a vibrating sample magnetometer (Lakeshore, VSM 7300), a Quantum Design MPMSXL superconducting quantum interference device (SQUID) magnetometer and a non-commercial low field SQUID magnetometer system [41]. The temperature dependence of the zero-field-cooled (ZFC) and field-cooled (FC) magnetization was measured in different applied magnetic fields. Hysteresis loops were recorded at some different temperatures in the low temperature phases of the system. The dynamics of the magnetic response was studied by ac-susceptibility measurements at different frequencies and measurements of the relaxation of the low field ZFC magnetization.

In the temperature dependent ZFC magnetization, the sample was cooled to lowest temperature in the absence of field, then the field was applied at the lowest temperature and the data were recorded on re-heating the sample. In the FC measurements the sample was cooled in the applied field to lowest temperature and the data were recorded on re-heating the sample, keeping the field applied. In the relaxation experiments, the sample was cooled in zero-field from a reference temperature to a measuring temperature, T_m and kept there during a wait time, t_w. After the wait time, a small probing field was applied and the magnetization was recorded as a function of time elapsed after the field application [42].

2.4 RESULTS AND DISCUSSION

2.4.1 Novel effects of size-disorder on the electronic and magnetic properties of rare earth manganates of the type $La_{0.7-x}Ln_xBa_{0.3}MnO_3$ (Ln =Pr, Nd, Gd and Dy) with large $\langle r_A \rangle$

All the manganate compositions of the formula $La_{0.7-x}Ln_xBa_{0.3}MnO_3$ (Ln = Pr, Nd, Gd and Dy) could be indexed on an orthorhombic structure with the *Pnma* space group.

Table 2.1 Crystal Structure and properties of $La_{0.7-x}Ln_xBa_{0.3}MnO_3$ (Ln = Pr, Nd, Gd and Dy)

Composition	$\langle r_A \rangle$ (Å)	σ^2 (Å^2)	Space group	Lattice parameters (Å)[a]			T_c (K)	T_{IM} (K)
				a	b	$c/\sqrt{2}$		
$x = 0.0$	1.292	0.014	*Pnma*	5.534	5.529	5.529	340	—
			Ln = Pr					
$x = 0.1$	1.289	0.014	*Pnma*	5.529	5.514	5.527	320	—
$x = 0.3$	1.281	0.016	*Pnma*	5.527	5.523	5.519	285	270
$x = 0.5$	1.274	0.017	*Pnma*	5.517	5.510	5.503	235	210
$x = 0.6$	1.270	0.017	*Pnma*	5.520	5.500	5.507	210	175
$x = 0.7$	1.266	0.018	*Pnma*	5.512	5.495	5.505	190	150
			Ln = Nd					
$x = 0.3$	1.276	0.017	*Pnma*	5.511	5.513	5.524	250	240
$x = 0.5$	1.266	0.018	*Pnma*	5.507	5.506	5.507	190	160
$x = 0.7$	1.255	0.020	*Pnma*	5.498	5.497	5.498	150	—
			Ln = Gd					
$x = 0.1$	1.281	0.016	*Pnma*	5.527	5.524	5.525	280	275
$x = 0.2$	1.270	0.019	*Pnma*	5.527	5.516	5.517	210	190
$x = 0.3$	1.259	0.021	*Pnma*	5.521	5.511	5.511	150	120
$x = 0.5$	1.238	0.025	*Pnma*	5.496	5.491	5.497	—	—
$x = 0.6$	1.227	0.026	*Pnma*	5.496	5.487	5.488	—	—
$x = 0.7$	1.216	0.027	*Pnma*	5.479	5.471	5.477	—	—
			Ln = Dy					
$x = 0.1$	1.279	0.017	*Pnma*	5.530	5.515	5.525	270	270
$x = 0.2$	1.266	0.020	*Pnma*	5.521	5.508	5.511	190	170
$x = 0.3$	1.252	0.023	*Pnma*	5.510	5.501	5.497	—	—
$x = 0.4$	1.239	0.026	*Pnma*	5.507	5.496	5.496	—	—

[a] Uncertainty is approximately ±0.004.

We have presented the lattice parameters of the various compositions in Table 2.1 along with the values of $\langle r_A \rangle$ and the size variance σ^2. The lattice parameters as well as the volume of the unit cell vary linearly with $\langle r_A \rangle$ as expected.

In Fig. 2.1, we show the magnetization and resistivity data of $La_{0.7-x}Pr_xBa_{0.3}MnO_3$ series of manganates. The T_C value decreases progressively with increasing x reaching a value of 190 K in $Pr_{0.7}Ba_{0.3}MnO_3$. The value of the saturation magnetization decreases only slightly with the increase in x (35 to 29 emu/g at 60 K in the x = 0.0 - 0.7 range).

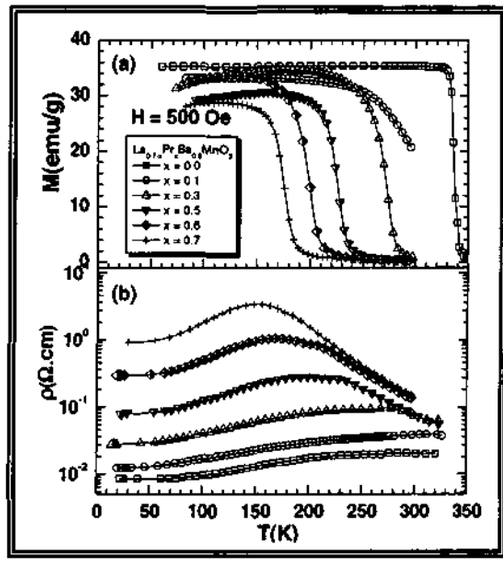

Figure 2.1 Temperature variation of (a) magnetization and (b) electrical resistivity of $La_{0.7-x}Pr_xBa_{0.3}MnO_3$.

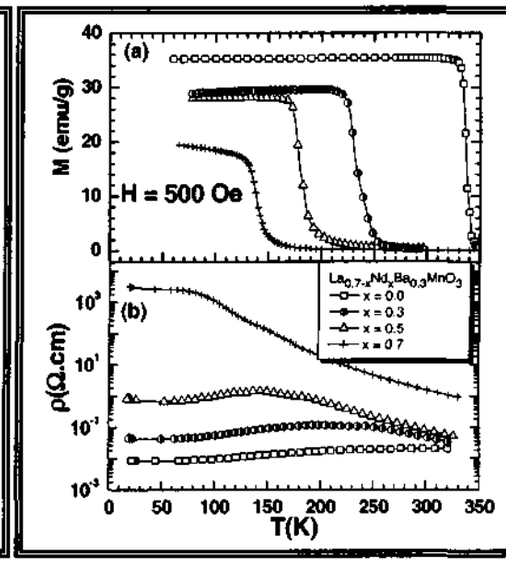

Figure 2.2 Temperature variation of (a) magnetization and (b) electrical resistivity of $La_{0.7-x}Nd_xBa_{0.3}MnO_3$.

The material is metallic at room temperature up to x = 0.3 and exhibits a broad I-M transition when $x \geq$ 0.3, the transition temperature, T_{IM}, decreasing with increasing x. $Pr_{0.7}Ba_{0.3}MnO_3$ itself shows the I-M transition around 150 K (T_{IM}) which is lower than the T_C value. This value of T_{IM} is somewhat higher than that reported by Heilman et al

[22]. It is interesting that, as x approaches 0.7, the difference between T_C and T_{IM} increases, with the latter becoming considerably lower than T_C. $Pr_{0.7}Ba_{0.3}MnO_3$ is, therefore, a ferromagnetic insulator in the regime between T_C and T_{IM} (190 - 150 K). The magnetization and resistivity data of $La_{0.7-x}Nd_xBa_{0.3}MnO_3$ are shown in Fig. 2.2. Here again, the T_C value decreases with increasing x, and there is a marked decrease in the value of the saturation magnetization as well. There is a sharp increase in magnetization with an apparent T_C of ~ 150 K, in $Nd_{0.7}Ba_{0.3}MnO_3$. But the saturation moment is small, suggesting there may be no long-range ferromagnetic ordering in the material. Thus, the saturation magnetization is 30 emu/g at x = 0.3 and $Nd_{0.7}Ba_{0.3}MnO_3$ (x = 0.7) does not exhibit clear saturation down to low temperatures. The highest value of magnetization obtained for $Nd_{0.7}Ba_{0.3}MnO_3$ is 18 emu/g compared to 35 emu/g in $La_{0.7}Ba_{0.3}MnO_3$ (60 K).

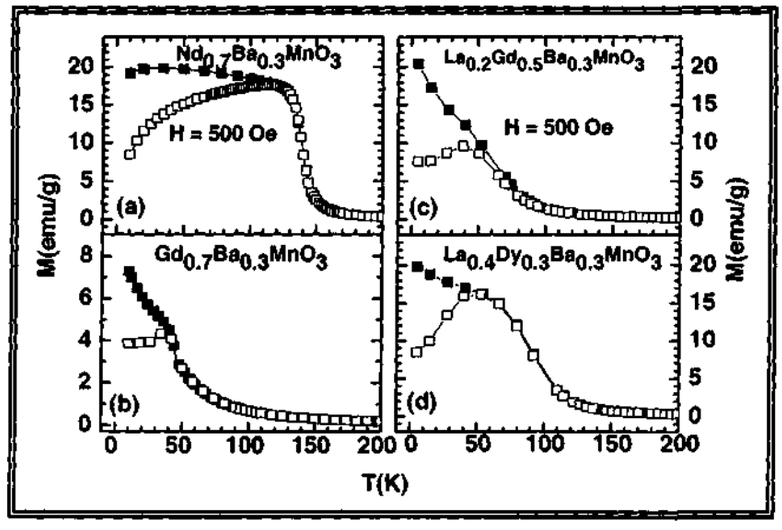

Figure 2.3 Temperature variation of the magnetization, M, of (a) $Nd_{0.7}Ba_{0.3}MnO_3$ (b) $Gd_{0.7}Ba_{0.3}MnO_3$ (c) $La_{0.2}Gd_{0.5}Ba_{0.3}MnO_3$ and (d) $La_{0.4}Dy_{0.3}Ba_{0.3}MnO_3$ (at H = 500 Oe). The solid symbols represent FC and open symbols represent ZFC data respectively.

The saturation magnetic moments in $Nd_{0.7}Ba_{0.3}MnO_3$ and $La_{0.7}Ba_{0.3}MnO_3$ are 0.8 and 1.5 μ_B respectively, while that in $Pr_{0.7}Ba_{0.3}MnO_3$ is 1.2 μ_B. Accordingly, the ZFC and FC data,

show considerable divergence below T_C (Fig. 2.3(a)), unlike in $Pr_{0.7}Ba_{0.3}MnO_3$. The resistivity behavior of $La_{0.7-x}Nd_xBa_{0.3}MnO_3$ is quite different from that of $La_{0.7-x}Pr_xBa_{0.3}MnO_3$. The $La_{0.7-x}Nd_xBa_{0.3}MnO_3$ compositions show a broad I-M transition when $x = 0.3$ and $x = 0.5$, but the 0.7 composition is an insulator with high resistivity. The resistivity behavior of $Nd_{0.7}Ba_{0.3}MnO_3$ found by us differs from the earlier report [23] to some extent. We do not find a distinct I-M transition in this material nor two resistivity peaks around T_{IM}. We barely see a shoulder around T_C as shown in Fig. 2.3(b). Since, $Nd_{0.7}Ba_{0.3}MnO_3$ does not show long-range ferromagnetic ordering; it would appear that the material contains ferromagnetic clusters in the insulating matrix. The double peaks in resistivity data reported earlier [23] or the shoulder near T_C found by us also suggest such phase separation. Ferromagnetic clusters in an insulating matrix would also be present in other compositions ($0.0 < x < 0.7$) where $T_C < T_{IM}$.

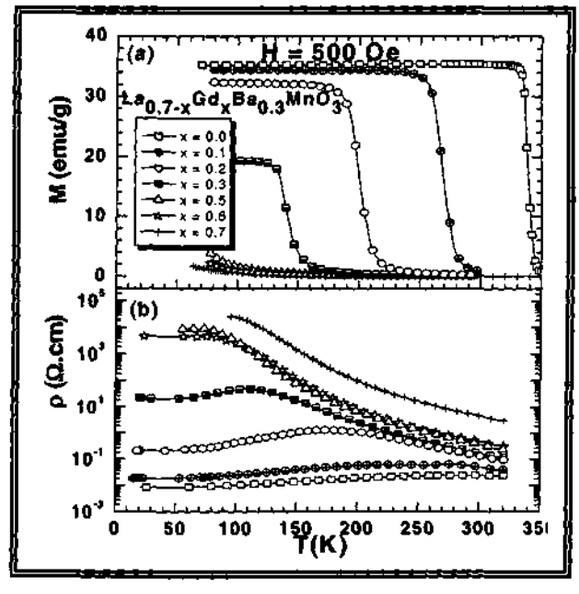

Figure 2.4 Temperature variation of (a) the magnetization, (H = 500 Oe) and (b) the electrical resistivity of $La_{0.7-x}Gd_x Ba_{0.3}MnO_3$.

In the $La_{0.7-x}Gd_xBa_{0.3}MnO_3$ series, progressive substitution of La by Gd, causes the ferromagnetic features to disappear entirely when $x \geq 0.5$ (Fig. 2.4(a)). Even when $x = 0.3$,

the T_C is only 155 K and the saturation magnetization is 20 emu/g at 60 K. The $x \geq 0.5$ compositions exhibit divergence between the ZFC and FC magnetization data (see Figs. 2.3(b) and (c)), indicating the absence of long-range ferromagnetic ordering. AC susceptibility measurements reveal a weakly frequency-dependent peak at 50 and 40 K respectively in the $x = 0.5$ and 0.7 compositions. These compositions also fail to show the I-M transitions in the resistivity data, whereas the samples with $x < 0.5$ show distinct I-M transitions. The compositions with $x > 0.5$ are insulating just as $Nd_{0.7}Ba_{0.3}MnO_3$ and the resistivity of $Gd_{0.7}Ba_{0.3}MnO_3$ is higher than that of $Nd_{0.7}Ba_{0.3}MnO_3$ (Fig. 2.4(b)). In the $La_{0.7-x}Dy_xBa_{0.3}MnO_3$ series, ferromagnetism does not occur for $x > 0.2$ (Fig. 2.5(a)). The $x = 0.2$ composition shows an apparent T_C of 180 K, but the saturation magnetization is very low (18 emu/g). The $x = 0.2$ composition shows the I-M transition, but all the compositions with $x > 0.2$ are insulating, the resistivity being higher than that of the corresponding Gd and Nd substituted manganates. The ZFC and FC data of the $x = 0.3$ composition shows divergence (Fig. 2.3(d)), indicating the absence of long-range ferromagnetic ordering.

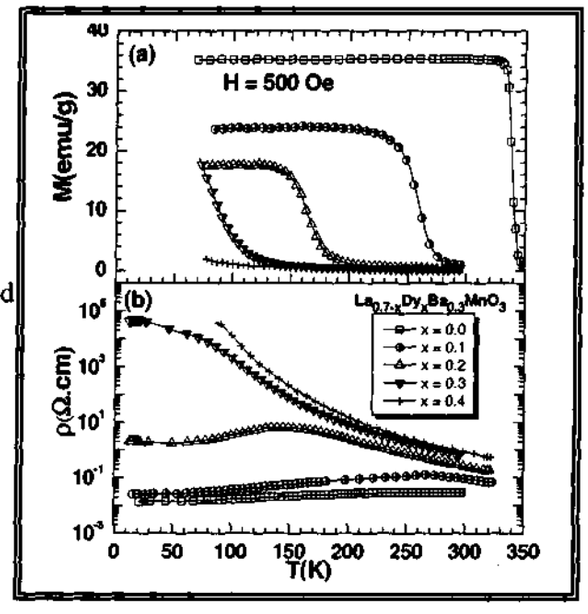

Figure 2.5 Temperature variation of (a) the magnetization (H = 500 Oe) and (b) the electrical resistivity of $La_{0.7-x}Dy_x Ba_{0.3}MnO_3$.

In both the $La_{0.7-x}Gd_xBa_{0.3}MnO_3$ and $La_{0.7-x}Dy_xBa_{0.3}MnO_3$ series of manganates, ferromagnetism disappears as x increases, accompanied by an insulating behavior. The apparent ferromagnetic transitions with a low saturation magnetization observed for x = 0.3 and 0.2 at 150 and 180 K respectively in the Gd and Dy derivatives, and associated with T_{IM} values lower than T_C, pointing to the presence of a ferromagnetic insulating state. It is likely that in all the compositions where the ferromagnetic insulating state occurs, there is phase separation wherein ferromagnetic clusters are present in an insulating matrix. It is interesting that the difference between T_C and T_{IM} manifests itself only when σ^2 is considerably large. In the four series of $La_{0.7-x}Ln_xBa_{0.3}MnO_3$ studied by us, the difference between T_C and T_{IM} starts emerging when the σ^2 = 0.016 Å^2, although the $\langle r_A \rangle$ is relatively large, being around 1.28 Å. Clearly the size disorder plays a crucial role in determining the properties of these manganates.

Table 2.2 Crystal structures of $Ln_{0.7-x}Ln'_xA_{0.3-y}A'_yMnO_3$ with fixed $\langle r_A \rangle$

Composition	σ^2 (Å^2)	Space group	Lattice parameters (Å)			V (Å^3)
			a	b	$c/\sqrt{2}$	
		$\langle r_A \rangle$ = 1.266 Å				
$La_{0.7}Ba_{0.14}Sr_{0.16}MnO_3$	0.008	*Pnma*	5.520	5.496	5.596	236
$La_{0.7}Ba_{0.21}Ca_{0.09}MnO_3$	0.011	*Pnma*	5.537	5.508	5.501	237
$Pr_{0.7}Ba_{0.3}MnO_3$	0.018	*Pnma*	5.512	5.495	5.505	236
$La_{0.5}Dy_{0.2}Ba_{0.3}MnO_3$	0.021	*Pnma*	5.521	5.508	5.511	237
		$\langle r_A \rangle$ = 1.216 Å				
$La_{0.7}Sr_{0.08}Ca_{0.22}MnO_3$	0.001	*Pnma*	5.467	5.468	5.476	232
$Nd_{0.7}Ba_{0.06}Sr_{0.24}MnO_3$	0.008	*Pnma*	5.474	5.464	5.469	232
$Pr_{0.7}Ba_{0.125}Ca_{0.125}MnO_3$	0.009	*Pnma*	5.485	5.474	5.474	233
$Nd_{0.7}Ba_{0.165}Ca_{0.135}MnO_3$	0.013	*Pnma*	5.490	5.473	5.469	233
$Sm_{0.7}Ba_{0.24}Ca_{0.06}MnO_3$	0.021	*Pnma*	5.483	5.472	5.473	233
$Gd_{0.7}Ba_{0.3}MnO_3$	0.028	*Pnma*	5.479	5.471	5.477	233

In order to investigate the effect of size-disorder quantitatively, we have examined the compositions with constant $\langle r_A \rangle$ values corresponding to $Pr_{0.7}Ba_{0.3}MnO_3$ and $Gd_{0.7}Ba_{0.3}MnO_3$ respectively, and varied the σ^2. In Table 2.2, we listed the structural parameters of two series of manganates. The magnetization and resistivity data of the compositions with $\langle r_A \rangle$ = 1.266 Å are shown in Fig. 2.6. We see that the T_C increases with decreasing σ^2 and the material becomes metallic at the lowest value of σ^2 = 0.008 Å^2, while I-M transitions occur in the σ^2 range of 0.02-0.01 Å^2. This is indeed a nice result in that a system normally showing an I-M transition becomes metallic as the size-disorder is decreased. The effect of size-disorder is seen more vividly when the $\langle r_A \rangle$ value is 1.216 Å, corresponding to $Gd_{0.7}Ba_{0.3}MnO_3$, a non-magnetic insulating material.

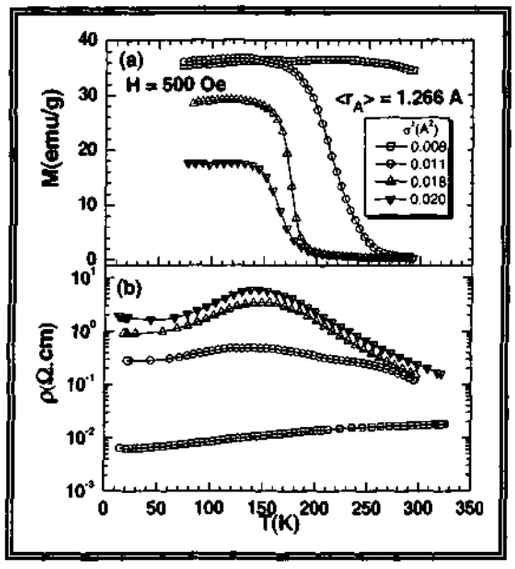

Figure 2.6 Temperature variation of (a) magnetization and (b) the electrical resistivity of $Ln_{0.7-x}Ln'_xA_{0.3-y}A'_yMnO_3$ with a fixed $\langle r_A \rangle$ value of 1.266 Å.

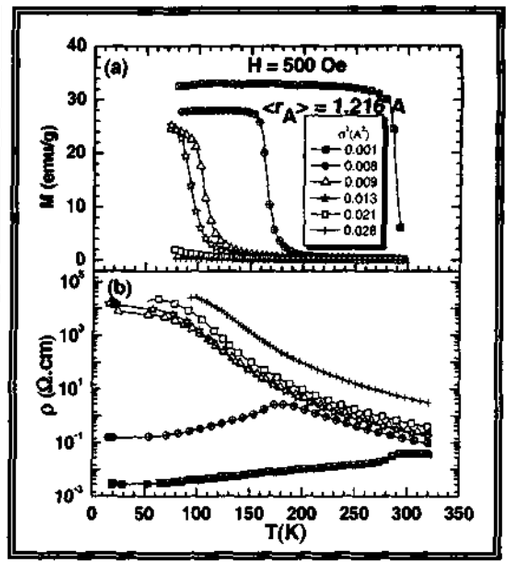

Figure 2.7 Temperature variation of (a) magnetization and (b) the electrical resistivity of $Ln_{0.7-x}Ln'_xA_{0.3-y}A'_yMnO_3$ with a fixed $\langle r_A \rangle$ value of 1.216 Å.

However, when the size-disorder is decreased, the material becomes ferromagnetic, with the T_C going up to ~ 300 K at the lowest value of σ^2 (Fig. 2.7(a)). As σ^2 decreases, the insulating behavior also gives way to metallic behavior. The T_C values (in Figs. 2.6(a) and 2.7(a)) vary linearly with σ^2 both slopes of 10 235 ± 2191 K $Å^{-2}$ and 17 068 ± 3260 K $Å^{-2}$ for $\langle r_A \rangle$ of 1.266 Å and $\langle r_A \rangle$ of 1.216 Å, respectively. The corresponding values of intercepts, T^0_C, are 374 ± 5 K and 305 ± 3 K, respectively. These values are comparable to those reported in the literature for other series of manganates [19, 43].

Conclusions

The electronic and magnetic properties of the four series of $La_{0.7-x}Ln_xBa_{0.3}MnO_3$ (Ln = Pr, Nd, Gd and Dy) manganates have revealed certain interesting aspects, wherein the average radius of the A-site cation generally remains large (1.216-1.292 Å), but the size disorder is considerable. Since the band narrowing due to small $\langle r_A \rangle$ is avoided, the predominant effect in these materials is due to size-disorder. It is interesting that these materials show a progressive decrease in the FM T_C, eventually giving rise to a non-FM insulating behavior. Accordingly, with increasing x or σ^2, the material exhibits a ferromagnetic insulating phase due to the presence of FM clusters in the insulating matrix. At large x or σ^2, where some of the compositions lose ferromagnetism and become insulating, there is evidence for clusters with short-range FM interaction. In the insulating regime caused by size-disorder, there is clearly phase separation due to the presence of FM clusters in an insulating matrix. The phase separation is minimized or eliminated by decreasing σ^2, as evidenced from the change of the non-magnetic insulating phase to a FM metallic state.

2.4.2 Glassy behavior in the ferromagnetic and the non-magnetic insulating states of the rare earth manganates, $Ln_{0.7}Ba_{0.3}MnO_3$ (Ln = Nd and Gd)

Rare earth manganates $La_{0.7}Ba_{0.3}MnO_3$, $Nd_{0.7}Ba_{0.3}MnO_3$ and $Gd_{0.7}Ba_{0.3}MnO_3$ possess orthorhombic structures (*Pnma* space group) and the lattice parameters decrease with the decrease in the size of the rare earth ion as expected. In Fig. 2.8, we show the variation of lattice parameters and cell volume with $\langle r_A \rangle$ to demonstrate this feature. The $\langle r_A \rangle$ values of $La_{0.7}Ba_{0.3}MnO_3$, $Nd_{0.7}Ba_{0.3}MnO_3$ and $Gd_{0.7}Ba_{0.3}MnO_3$ are 1.292, 1.255 and 1.216 Å respectively, the corresponding values of the size-disorder parameter, σ^2, being 0.014, 0.020 and 0.027 $Å^2$ respectively. Thus, $Gd_{0.7}Ba_{0.3}MnO_3$ has the smallest $\langle r_A \rangle$ and the largest σ^2.

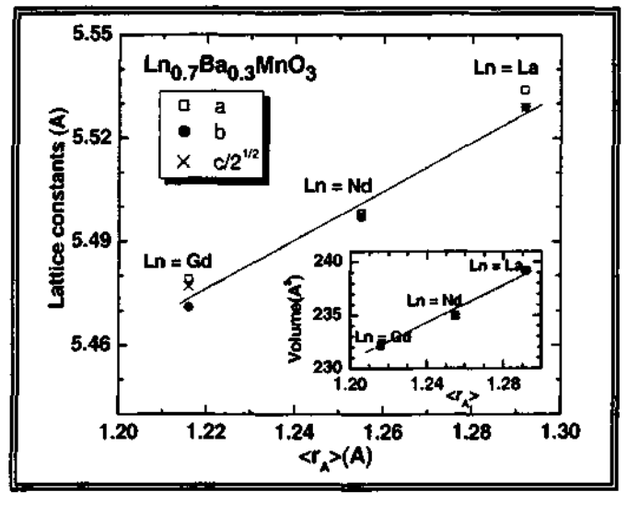

Figure 2.8 Variation of lattice - parameters and cell volume (inset-figure) with $\langle r_A \rangle$ of $Ln_{0.7}Ba_{0.3}MnO_3$ with Ln = La, Nd and Gd.

In Figure 2.9, we show the dc magnetization behavior of $La_{0.7}Ba_{0.3}MnO_3$, $Nd_{0.7}Ba_{0.3}MnO_3$ and $Gd_{0.7}Ba_{0.3}MnO_3$ under FC conditions (500 Oe). $La_{0.7}Ba_{0.3}MnO_3$ shows a sharp increase in the FC magnetization around 340 K (T_C) corresponding to the ferromagnetic transition. There is evidence for saturation, the values of the saturation magnetization and the corresponding magnetic moment being 35 emu/g and 1.5 μ_B/f.u. $Nd_{0.7}Ba_{0.3}MnO_3$ shows an increase in the magnetization around 150 K, but the maximum

magnetization value found is 18 emu/g (0.8 μ_B/f.u.) at 40 K. $Gd_{0.7}Ba_{0.3}MnO_3$ shows no evidence for a magnetic transition and the magnetization value is 5 emu/g (0.25 μ_B/f.u.) at 40 K. Clearly, the magnetic properties of the three manganates are distinctly different from one another. Whereas $La_{0.7}Ba_{0.3}MnO_3$ shows metallic behavior below T_C, $Nd_{0.7}Ba_{0.3}MnO_3$ and $Gd_{0.7}Ba_{0.3}MnO_3$ show insulating behavior over the entire temperature range (Fig. 2.9(b)). Thus, $Nd_{0.7}Ba_{0.3}MnO_3$ is insulating at and below the 150 K transition and $Gd_{0.7}Ba_{0.3}MnO_3$ is a non-magnetic insulator at all temperatures.

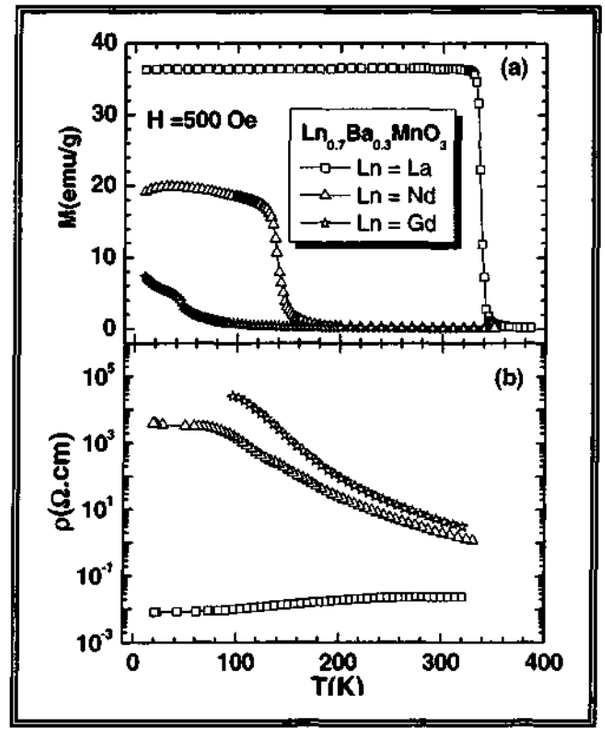

Figure 2.9 Temperature dependence of (a) the FC magnetization, M, (at H = 500 Oe) and (b) the electrical resistivity, ρ, of $Ln_{0.7}Ba_{0.3}MnO_3$ with Ln = La, Nd and Gd. Note that $Nd_{0.7}Ba_{0.3}MnO_3$ is insulating at 150 K where there is weak magnetic transition.

Magnetization data of $La_{0.7}Ba_{0.3}MnO_3$ at low fields were similar to those obtained at higher field showing little divergence between the ZFC and FC data. In Fig. 2.10, we

present the low-field ZFC and FC magnetization data of $Nd_{0.7}Ba_{0.3}MnO_3$ and $Gd_{0.7}Ba_{0.3}MnO_3$. The FC magnetization of $Nd_{0.7}Ba_{0.3}MnO_3$ shows the transition around 150 K. $Gd_{0.7}Ba_{0.3}MnO_3$ exhibits a rather complex behavior below 62 K where irreversibility between the ZFC and FC magnetization data first appears (Fig. 2.10(b)). The low temperature region is discussed later, but it is noteworthy that there are three characteristic temperatures: 62 K (onset of significant irreversibility between the ZFC and FC magnetization curves), 46 K (a maximum in the FC curve) and 36 K (a maximum in the ZFC curve), all indicating different ordering and/or freezing processes in the system.

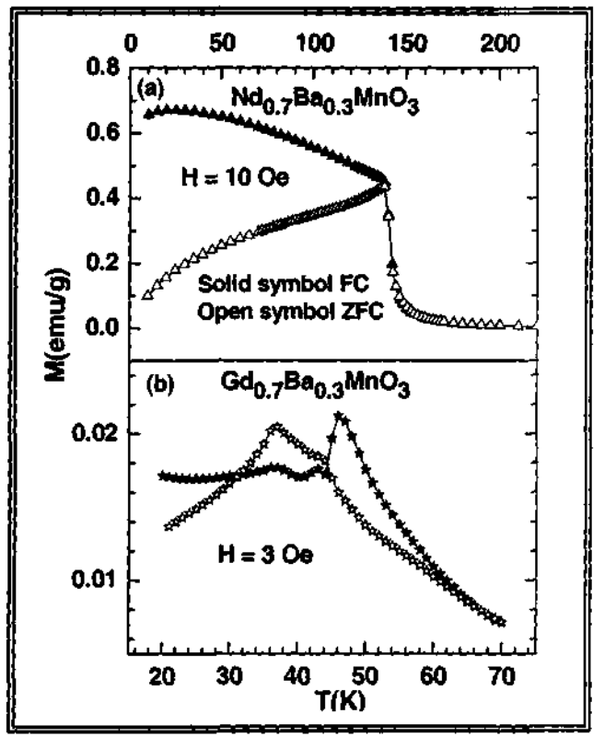

Figure 2.10 Temperature dependence of the ZFC (open symbols) and FC (solid symbols) magnetization, M, of (a) $Nd_{0.7}Ba_{0.3}MnO_3$ (at H = 10 Oe) and (b) $Gd_{0.7}Ba_{0.3}MnO_3$ (at H = 3 Oe). The features of the M-T curves remain same when the magnetic field is in the 1-10 Oe range.

Figure 2.11 shows the field-variation of magnetization at three different temperatures for $Nd_{0.7}Ba_{0.3}MnO_3$ and $Gd_{0.7}Ba_{0.3}MnO_3$. Below 150 K, $Nd_{0.7}Ba_{0.3}MnO_3$ shows a behavior similar to a soft ferromagnet, the magnetization approaching saturation at high fields. $Gd_{0.7}Ba_{0.3}MnO_3$ does not show the M-H behavior of a ferromagnet at low temperatures, and exhibit no tendency for saturation even at high fields. The shape of the M-H curve and the absence of saturation even at high fields found in $Gd_{0.7}Ba_{0.3}MnO_3$ are reminiscent of magnetization curves of spin glasses [44]. The M-H behavior becomes nearly linear (paramagnetic) at 200 K in both the manganates.

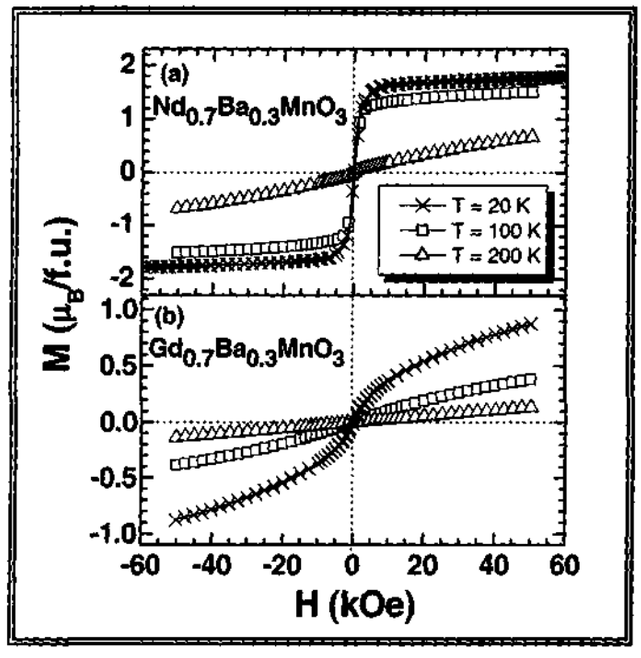

Figure 2.11 Typical hysteresis curves for (a) $Nd_{0.7}Ba_{0.3}MnO_3$ (b) $Gd_{0.7}Ba_{0.3}MnO_3$ at different temperatures.

The temperature dependence of the ac susceptibility of $Nd_{0.7}Ba_{0.3}MnO_3$ and $Gd_{0.7}Ba_{0.3}MnO_3$ is presented at different frequencies in Fig. 2.12. The in-phase $\chi'(T)$ component of the ac susceptibility reveals similar features as the ZFC-magnetization at low-field in both the manganates. $Nd_{0.7}Ba_{0.3}MnO_3$ shows a sharp maximum below 150 K,

which is frequency-independent. However, there is weak frequency dependence at temperatures below 140 K, a behavior noted earlier in $Nd_{0.7}Sr_{0.3}MnO_3$ [26]. $Gd_{0.7}Ba_{0.3}MnO_3$ shows a shoulder around 62 K, a weak anomaly just above 46 K and a maximum at 36 K. The $\chi'(T)$ data become strongly frequency-dependent below 36 K. This transition could arise from the presence of small magnetic clusters in a non-magnetic matrix. Other examples of oxide systems where only short-range ferromagnetic correlations occur are known [26, 45].

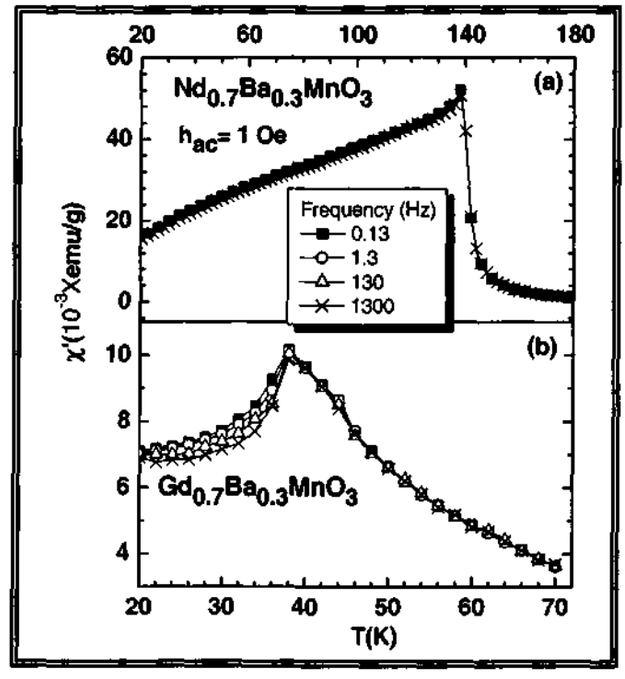

Figure 2.12 Temperature dependence of the in-phase ac-susceptibility at different frequencies for (a) $Nd_{0.7}Ba_{0.3}MnO_3$ and (b) $Gd_{0.7}Ba_{0.3}MnO_3$.

Time-dependent ZFC magnetization measurements show that both $Nd_{0.7}Ba_{0.3}MnO_3$ and $Gd_{0.7}Ba_{0.3}MnO_3$ exhibit logarithmically slow dynamics and aging at low temperatures. In Fig. 2.13, we show the time-dependent ZFC magnetization, m(t), measured at T_m = 40 K, and the corresponding relaxation rates S(t) = 1/H

$[dM_{ZFC}(T,t_w,t)/dlog_{10}(t)]$ for $Nd_{0.7}Ba_{0.3}MnO_3$. The applied field was 1 Oe and the wait times were t_w = 100, 1000 and 10000 s. The results of similar measurements on $Gd_{0.7}Ba_{0.3}MnO_3$ at 30 K are presented in Fig. 2.14. The wait time dependence of the magnetic relaxation illustrated in Figs. 2.13 and 2.14 show that both the manganates are subject to magnetic aging at low temperatures. Relaxation experiments (not shown) at 80 K (Nd) and 40 K (Gd) reveal slow relaxation and aging behavior at these temperatures as well, but with a much decreased relaxation rate compared to that at low temperatures.

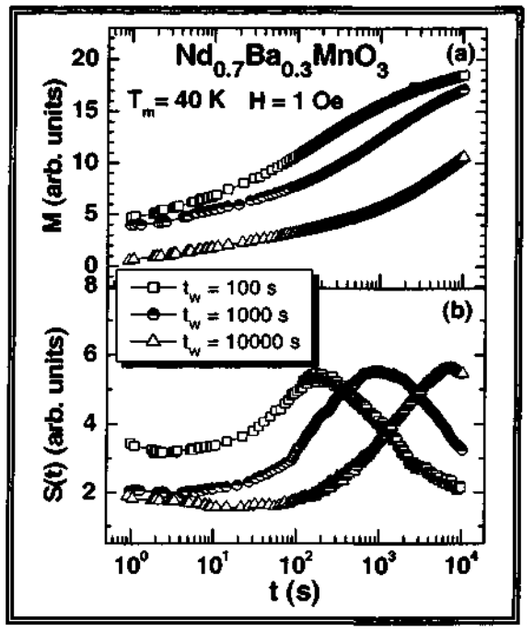

Figure 2.13 ZFC-relaxation measurements on $Nd_{0.7}Ba_{0.3}MnO_3$ at T_m = 40 K for different waiting times.

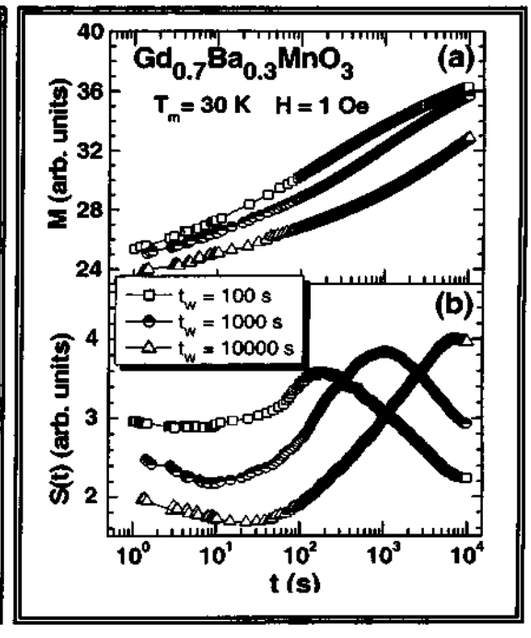

Figure 2.14 ZFC-relaxation measurements on $Gd_{0.7}Ba_{0.3}MnO_3$ at T_m = 30 K for different waiting times.

Time-dependent thermo-remanent magnetization (TRM) measurements at the same temperatures yielded similar results for both systems. Magnetic aging is a signature of spin-glasses [44] and explained within the droplet (or domain growth) model the

maximum in the relaxation rate is associated with a crossover between quasi-equilibrium and non-equilibrium dynamics [46]. The slow relaxation and aging behavior of $Nd_{0.7}Ba_{0.3}MnO_3$ and $Gd_{0.7}Ba_{0.3}MnO_3$ demonstrate that magnetic disorder and frustration occur in the low temperature phases.

Glassy dynamics in spin glasses is also manifested by a memory effect that can be demonstrated by dc-magnetization or low frequency ac-susceptibility experiments. We have employed zero-field-cooled magnetization vs. temperature experiments [42] to investigate possible memory phenomena in the two manganates. The experiment includes a reference measurement, according to the ZFC protocol described earlier, and a similar ZFC memory experiment, the protocol of which only includes one additional feature, the cooling down of the sample is halted at a stop temperature for some hours. In a spin-glass experiment, the memory curve acquires a weak dip at the temperature where the zero-field cooling was halted. To illustrate the memory effect, it is convenient to plot the difference between the reference and the memory curve. A spin glass phase (ordinary or re-entrant) has a pronounced memory behavior, whereas a disordered and frustrated ferromagnetic phase shows little or no memory effect. In the case of $Nd_{0.7}Ba_{0.3}MnO_3$, we carried out the ZFC experiment by cooling the sample from a reference temperature of 170 K to 90 K, where the magnetic field (10 Oe) was applied and the magnetization recorded on reheating the sample to 170 K. The ZFC memory curve was recorded in a similar way with the additional feature that the cooling in zero field was stopped at 120 K for 3 hours. Figure 2.15(a) shows the two curves. A weak dip can barely be discerned in the memory curve (labelled 120 K). The difference plot showing $M_{mem}(T)$-$M_{ref}(T)$, shown as an inset in Fig. 2.15, reveals a broad but shallow memory of the stop at 120 K. In

contrast, the corresponding experiment on the $Gd_{0.7}Ba_{0.3}MnO_3$ sample shows a prominent memory dip. The experiment was performed starting from 70 K and cooling the sample continuously to 20 K, with an intermediate stop at 30 K for 3 hours in the memory measurement. Fig. 2.15(b) shows the two curves. There is a significant difference between the reference and the memory curves. The difference plot shown in the inset of Fig. 2.15(b) reveals a deep, broad memory dip. The dip abruptly ceases above 36 K. The memory behavior of $Gd_{0.7}Ba_{0.3}MnO_3$ at 36 K is clearly that of a spin-glass.

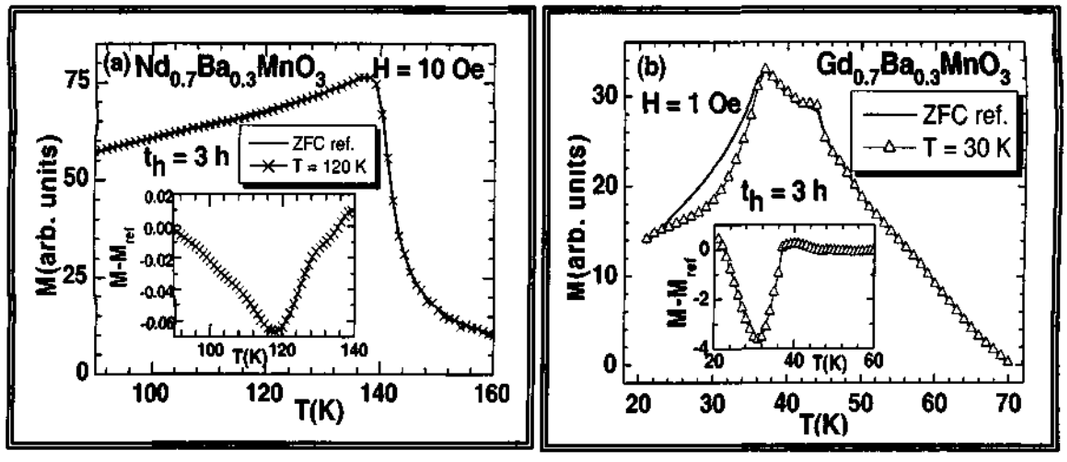

Figure 2.15 ZFC-magnetization memory experiment on (a) $Nd_{0.7}Ba_{0.3}MnO_3$; the temperature dependence of ZFC magnetization, M, (reference curve) and on imprinting memories at temperature stops (120 K) during cooling for 3 hours (H = 10 Oe) and the inset shows difference (M_{mem}-M_{ref}) plot. (b) $Gd_{0.7}Ba_{0.3}MnO_3$; the temperature dependence of ZFC magnetization, M, (reference curve) and on imprinting memory at 30 K during cooling for 3 hours (H = 1 Oe). The inset shows the difference (M_{mem}-M_{ref}) plot.

Conclusions

The present study on $Nd_{0.7}Ba_{0.3}MnO_3$ shows an increase in magnetization at 150 K, but the value of magnetization is small at low temperature. It is also an insulator. It

shows a pronounced aging behavior, but a rather weak memory effect below 150 K, probably due to the presence of FM clusters in an insulating matrix. $Nd_{0.7}Ba_{0.3}MnO_3$ appears to be a cluster glass or a magnetically disordered system similar to $La_{1-x}Sr_xCoO_3$ [47]. $Gd_{0.7}Ba_{0.3}MnO_3$ appears to contain small magnetic clusters, giving rise to a spin-glass state below 36 K. Low-field magnetization experiments indicate that some kind of ordering/or freezing process occurs in this manganate even around 62 K, with an additional process at 46 K. The origin of these features is difficult to establish from macroscopic magnetization data. The small proportion of the clusters responsible for the weak 62 K transition does not result in a distinct glassy transition or a FM-like transition. This behavior of $Gd_{0.7}Ba_{0.3}MnO_3$ is attributed to the large size mismatch between the A-site cations or large σ^2 value (0.028 $Å^2$), the mismatch being considerably smaller in $Nd_{0.7}Ba_{0.3}MnO_3$ [23]. Such size mismatch favors chemical/electronic inhomogeneities. To our knowledge, this is a unique case of a perovskite manganate showing a size disorder-induced spin-glass behavior, occurring in spite of the relatively large A-site cations radius ($\langle r_A \rangle$ = 1.216 Å). It appears that the so-called FM insulating state or non-magnetic insulating state often reported in the rare earth manganates of the type $Ln_{1-x}A_xMnO_3$ arises from the glassy behavior of the magnetic clusters in these materials, generally associated with electronic phase separation.

2.4.3 Occurrence of re-entrant FM transitions in rare-earth manganates on cooling the charge-ordered states: A consequence of electronic phase separation

In Table 2.3 and 2.4, we have presented the values of the lattice parameters, $\langle r_A \rangle$ and σ^2 along with insulator-metal transition (T_{IM}), ferromagnetic transition (T_C) and the

charge ordering transition temperature, T_{CO} for $La_{0.5-x}Ln_xCa_{0.5}MnO_3$ (Ln = Pr, Nd) and $Nd_{0.5}Ca_{0.5-x}Sr_xMnO_3$ series of manganates. The T_C values were obtained from the M-T curves, taking the point at which there is an abrupt increase in M as the T_C. The T_{CO} values were also obtained from the inverse M vs T plots. The value of T_{IM} or T_p is obtained from the electrical resistivity measurements, which corresponds to the maximum in the ρ-T curve.

Table 2.3 Structure and properties of $La_{0.5-x}Ln_xCa_{0.5}MnO_3$(Ln = Nd, Pr)

Composition	$\langle r_A \rangle$ (Å)	σ^2 (Å^2)	Lattice parameter (Å)			Mn^{4+} (%)	T_C (K)	T_p (K)
			a	*b*	*c*			
$La_{0.42}Nd_{0.08}Ca_{0.5}MnO_3$	1.194	0.00029	5.4105	7.6367	5.4258	45	218	~177
$La_{0.45}Nd_{0.05}Ca_{0.5}MnO_3$	1.195	0.00025	5.4149	7.6471	5.4241	46	229	169
$La_{0.45}Pr_{0.05}Ca_{0.5}MnO_3$	1.196	0.00021	5.4150	7.6372	5.4307	46	235	~172
$La_{0.48}Pr_{0.02}Ca_{0.5}MnO_3$	1.197	0.00022	5.4124	7.6447	5.4401	46	140	~138

Table 2.4 Structure and properties of $Nd_{0.5}Ca_{0.5-x}Sr_xMnO_3$

Composition	$\langle r_A \rangle$ (Å)	σ^2 (Å^2)	Lattice parameter (Å)			Space group	Mn^{4+} (%)	T_C (K)	T_p (K)	T_{CO} (K)
			a	*b*	*c*					
$Nd_{0.5}Ca_{0.5}MnO_3$	1.172	0.0001	5.401	7.619	5.385	*Pnma*	47	-	-	240
$Nd_{0.5}Ca_{0.25}Sr_{0.25}MnO_3$	1.204	0.0038	5.4129	7.6331	5.4126	*Pnma*	46	155	(155)	214 ± 4
$Nd_{0.5}Ca_{0.2}Sr_{0.3}MnO_3$	1.211	0.0043	5.4189	7.6404	5.4143	*Pnma*	47	195	(178)	-
$Nd_{0.5}Ca_{0.15}Sr_{0.35}MnO_3$	1.217	0.0047	5.4167	7.6406	5.4345	*Imma*	49	218	202	110 ± 3
$Nd_{0.5}Ca_{0.1}Sr_{0.4}MnO_3$	1.224	0.0050	5.4205	7.6330	5.4542	*Imma*	49	235	220	124 ± 3
$Nd_{0.5}Ca_{0.05}Sr_{0.45}MnO_3$	1.230	0.0053	5.4257	7.6279	5.4655	*Imma*	48	250	236	144 ± 2
$Nd_{0.5}Sr_{0.5}MnO_3$	1.236	0.0054	5.426	7.634	5.475	*Imma*	49	267	249	150

We show the temperature variation of magnetization of $La_{0.5-x}Ln_xCa_{0.5}MnO_3$ (Ln = Pr, Nd) with composition in the $\langle r_A \rangle$ regime of 1.194-1.197Å in Fig. 2.16(a). The data clearly show how the T_C increases with increase in $\langle r_A \rangle$ as expected. The plot of the

inverse magnetization vs temperature in the inset of Fig. 2.16(a) shows a clear minimum as evidence for charge ordering in the $\langle r_A \rangle$ = 1.194 Å case, but we could not obtain reliable values of the charge ordering transition temperature, T_{CO}, in other samples. The temperature variation of resistivity of these materials (Fig. 2.16(b)) shows the occurrence of insulator-metal transitions in all the materials in this $\langle r_A \rangle$ range. Although the I-M transition is broad, the data show that metallicity manifests itself when the material becomes ferromagnetic.

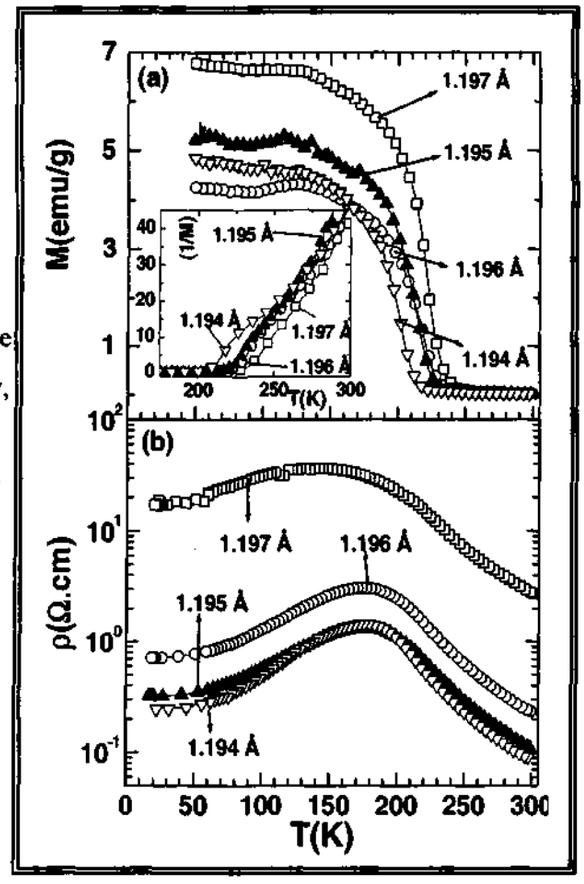

Figure 2.16 Temperature variation of the (a) magnetization, M, and (b) resistivity, ρ, of $La_{0.5-x}Ln_xCa_{0.5}MnO_3$ (Ln =Pr, Nd). Inset in figure (a) shows the variation of inverse magnetization with temperature. Values of $\langle r_A \rangle$ are shown (in Å).

Clearly, the manganate compositions in this $\langle r_A \rangle$ regime are ferromagnetic and metallic at low temperatures. The FM T_C values from Fig. 2.16(a) can be used along with the data from earlier studies to examine the relative variations of T_C and T_{CO} with $\langle r_A \rangle$

[36]. We compared the available T_C and T_{CO} data in Fig. 2.17. At $\langle r_A \rangle > 1.195$ Å, T_C values can be obtained reliably, but not the T_{CO}, the latter being associated with large uncertainties. Although the data suffer from the fact that we do not have sufficient T_{CO} data between $\langle r_A \rangle$ values 1.193 Å and 1.20 Å, the data do show that T_C and T_{CO} curves intersect each other around $\langle r_A \rangle$ value of 1.195 ± 0.003 Å.

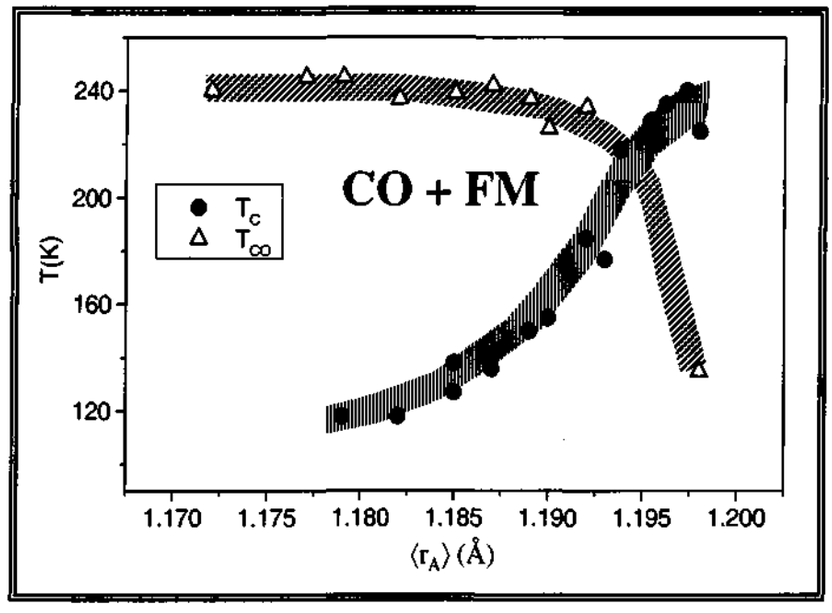

Figure 2.17 Variation of the ferromagnetic Curie temperature, T_C, and the CO transition temperature, T_{CO}, with $\langle r_A \rangle$ in $La_{0.5-x}Ln_xCa_{0.5}MnO_3$ (Ln = Nd, Pr). In the temperature range between T_{CO} and T_C, the charged-ordered and FM phases coexist.

We have carried out magnetization measurements on $Nd_{0.5}Ca_{0.5-x}Sr_xMnO_3$ system. When $x = 0.5$, the material shows the well known ferromagnetic transition around 250 K and undergoes charge ordering transition on cooling at 150 K, the material becoming antiferromagnetic around the same temperature (Fig. 2.18). Both the ferromagnetic and charge ordering transitions are sharp in this composition. As mentioned earlier, the $x = 0$ composition ($Nd_{0.5}Ca_{0.5}MnO_3$), shows only charge ordering (T_{CO} = 240 K), but no

ferromagnetism. The $Nd_{0.5}Ca_{0.5-x}Sr_xMnO_3$, compositions with x = 0.25-0.45 show ferromagnetic transitions in magnetization data (Fig. 2.18), with the T_C increasing with increase in x. Thus, the x = 0.25 composition has a T_C close to 150 K.

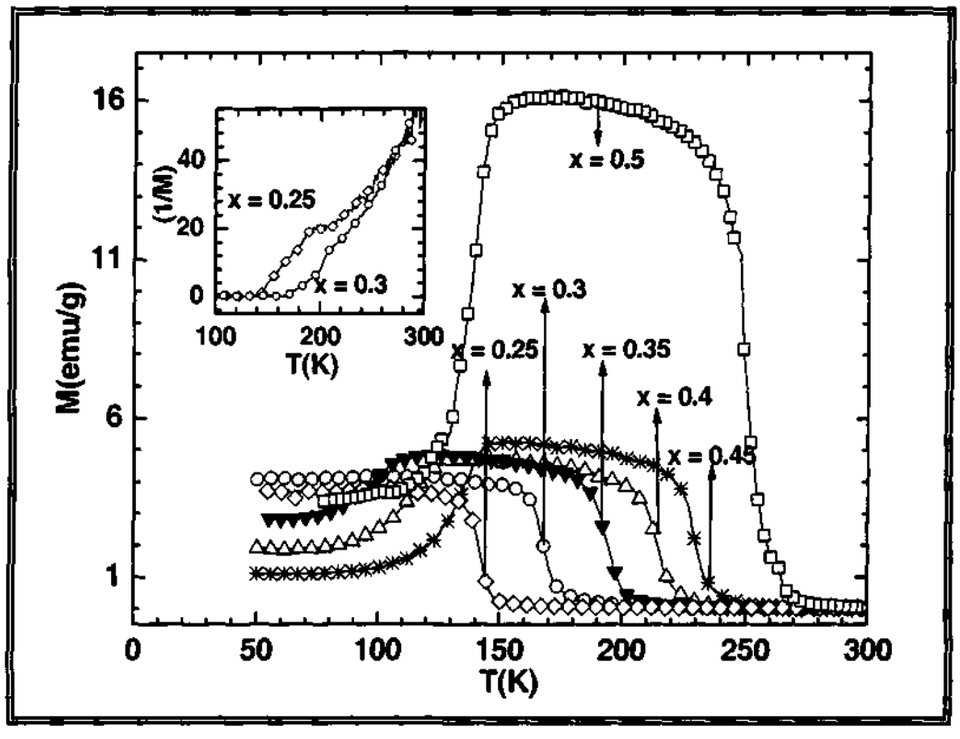

Figure 2.18 Temperature variation of magnetization of $Nd_{0.5}Ca_{0.5-x}Sr_xMnO_3$. The inset shows the variation of inverse magnetization with temperature.

However it is noteworthy that when x < 0.35, there is no sharp drop in magnetization data corresponding to the charge ordering transition. We can however, obtain the T_{CO} values for x = 0.35-0.45 compositions, from the magnetization data. The compositions with x = 0.25 and 0.30 are more like $Nd_{0.5}Ca_{0.5}MnO_3$ and the temperature variation of the inverse magnetization show a dip corresponding to T_{CO} (see inset of Fig. 2.18). The T_{CO} values of x = 0.25 and x = 0.1 compositions are 214 K and 230 K respectively. In Fig. 2.19 we have plotted the data obtained by us on the T_C and T_{CO} of

$Nd_{0.5}Ca_{0.5-x}Sr_xMnO_3$ against $\langle r_A \rangle$ along with data on two compositions ($0.0 < x < 0.25$) from the literature [33]. Although there is some scattering in the points, the data clearly show that when $\langle r_A \rangle$ < 1.20 Å, the $T_C < T_{CO}$, suggesting that we can consider the FM transition to be re-entrant in nature, just as the $La_{0.5-x}Ln_xCa_{0.5}MnO_3$ (Ln =Pr, Nd) (Fig. 2.17). Furthermore, the T_C - $\langle r_A \rangle$ and T_{CO} - $\langle r_A \rangle$ curves in Fig. 2.19, cross each other around $\langle r_A \rangle$ = 1.200 ± 0.005 Å, which is close to the cross-over $\langle r_A \rangle$ value found in $La_{0.5-x}Ln_xCa_{0.5}MnO_3$ (Fig. 2.17), within experimental error. It is possible that over the entire $\langle r_A \rangle$ range of 1.17-1.24 Å, there is co-existence of the charge-ordered and FM phases. This would certainly be true below T_C as evidenced from the diffraction data [48].

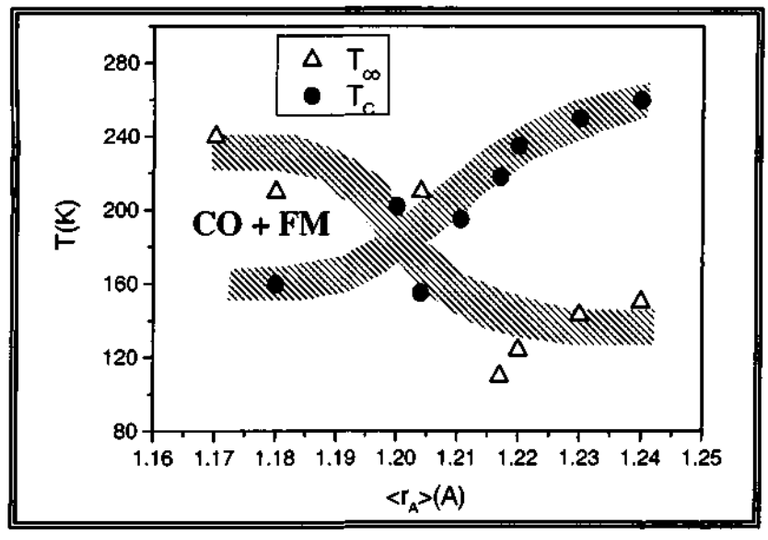

Figure 2.19 Variation of ferromagnetic Curie temperature, T_C, and the CO transition temperature, T_{CO}, with $\langle r_A \rangle$ in $Nd_{0.5}Ca_{0.5-x}Sr_xMnO_3$. In the temperature range between T_{CO} and T_C, the charged-ordered and FM phases coexist.

In Fig. 2.20, we have plotted the available data for $Nd_{0.5}Ca_{0.5}Mn_{1-x}M_xO_3$ (M = Cr, Ru), where $\langle r_A \rangle$ is constant (1.17Å) [30-32]. With the substitution of Cr and Ru in the Mn site, the material shows ferromagnetism as well as charge ordering. The T_{CO} generally

decreases with increase in x, while T_C increases specially in the case of Ru substitution. It appears that this ferromagnetic transition is re-entrant in nature in these manganate compositions. Fig. 2.20 also suggests that T_C and T_{CO} curves cross each other at a specific value of x. In the temperature range between T_{CO} and T_C, the charged-ordered and FM phases coexist.

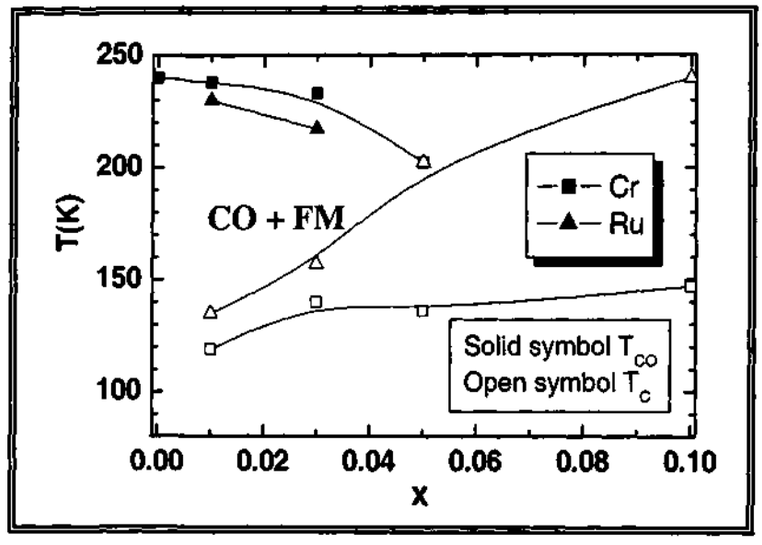

Figure 2.20 Variation of ferromagnetic Curie temperature, T_C, and the CO transition temperature, T_{CO}, with x in $Nd_{0.5}Ca_{0.5}Mn_{1-x}M_xO_3$ (M = Cr, Ru).

The reason we find that $T_{CO} > T_C$ in manganates with small $\langle r_A \rangle$ ($\langle r_A \rangle < 1.20$ Å), is probably because of electronic phase separation. It is known that only when $\langle r_A \rangle < 1.20$ Å or 1.19 Å, charge-ordering and associated effects occur in the rare earth manganates [5, 19]. The so-called FM transition is thus a consequence of electronic phase separation. The T_C's at small $\langle r_A \rangle$ do not really correspond to genuine FM transitions, and accordingly the saturation magnetization values of these samples at low temperatures are small. It is only at large $\langle r_A \rangle$, ($\langle r_A \rangle \geq 1.20$ Å) that genuine FM phases associated with high T_C values get manifested.

Conclusions

In the current investigations magnetic and electron transport properties of three series of rare earth manganates can be understood in terms of electronic phase separation. The system becomes FM metallic on cooling the CO insulating state and this behavior is favored for small $\langle r_A \rangle$ value. In these systems, the T_C increases with increase in $\langle r_A \rangle$ while T_{CO} decreases and accordingly the cross over between T_{CO} and T_C takes place around $\langle r_A \rangle$ value of 1.195 and 1.20 Å for two series of manganates. It appears that in the intermediate temperature range between T_{CO} and T_C, the FM metallic and CO insulating phases coexist for these compositions and such electronic phase separation is expected to be favored by small $\langle r_A \rangle$ values [19].

2.5 REFERENCES

1. E. Dagotto (Eds), *Nanoscale Phase Separation and Colossal Magnetoresistance* (Berlin: Springer, 2003); C. N. R. Rao, A. K. Kundu, M. M. Seikh and L. Sudheendra, Dalton Trans., **19**, 3003 (2004).
2. P. Schiffer, A. P. Ramirez, W. Bao and S. W. Cheong, Phys. Rev. Lett., **75**, 3336 (1995); P. G. Radaelli, D. E. Cox, M. Marezio and S. W. Cheong, Phys. Rev. B, **55**, 3015 (1997).
3. G. Allodi, R. D. Renzi, G. Guidi, F. Licci and M. W. Pieper, Phys. Rev. B, **56**, 6036 (1997).
4. H. Kawano, R. Kajimoto, M. Kubota, and H. Yoshizawa, Phys. Rev. B, **53**, 2202 (1996).
5. M. Uehara, S. Mori, C. H. Chen and S. W. Cheong, Nature, **399**, 560 (1999).
6. A. Moreo, M. Mayr, A. Feiguin, S. Yunoki and E. Dagotto, Phys. Rev. Lett., **84**, 5568 (2000).
7. C. Ritter, R. Mahendiran, M. R. Ibarra, L. Morellon, A. Maignan, B. Raveau and C. N. R. Rao, Phys. Rev. B, **61**, R9229 (2000).
8. Y. Endoh, K. Hiroda, S. Ishihara, S. Okamoto, Y. Murakami, A. Nishizawa, T. Fukuda, H. Kimura, H. Nojiri, K. Kaneko and Maekawa, Phys. Rev. Lett., **82**, 4328 (1999).
9. Y. Yamada, O. Hino, S. Nohdo, R. Kanao, T. Inami and S. Katano, Phys. Rev. Lett., **77**, 904 (1996).

10. S. Yunoki, T. Hotta and E. Dagotto, Phys. Rev. Lett., **84**, 3714 (2000).

11. C. N. R. Rao, and B. Raveau (Eds), *Colossal Magnetoresistance, Charge Ordering and related properties of Manganese Oxides* (World Scientific: Singapore, 1998).

12. Y. Tokura (Eds), *Colossal Magnetoresistance Oxides* (London: Gorden and Breach, 1999).

13. A. P. Ramirez, J. Phys: Condens. Matter., **9**, 8171 (1997).

14. N. Kumar and C. N. R. Rao, J. Solid. State. Chem., **129**, 363 (1997).

15. E. Dagotto, Science, **309**, 257 (2005) and the references therein.

16. V. B. Shenoy, D. D. Sarma and C. N. R. Rao, Chem. Phys. Chem., Preprint: to be published (2006).

17. C. N. R. Rao and P. V. Vanitha, Curr. Opin. Solid State Mater. Sci., **6**, 97 (2002).

18. C. N. R. Rao, J. Phys. Chem. B, **104**, 5877 (2000).

19. L. Sudheendra and C. N. R. Rao, J. Phys.: Condens. Matter, **15**, 3029 (2003).

20. L. M. Rodriguez-Martinez and J. P. Attfield, Phys. Rev. B, **54**, R15622 (1996); L. M. Rodriguez-Martinez and J. P. Attfield, Phys. Rev. B, **63**, 024424 (2000).

21. H. L. Ju, J. Gopalakrishnan, J. L. Peng, Qi Li, G. C. Xiong, T. Venkatesan, and R. L. Greene, Phys. Rev. B, **51**, 6143 (1995); A. Barnabe, M. Fillange, A. Maigan, M. Hervieu and B. Raveau, Chem. Mat., **10**, 252 (1998).

22. A. K. Heilman, Y.Y. Xue, B. Lorenz, B. J. Campbell, J. Cmaidalka, R. L. Meng, Y. S. Wang, and C. W. Chu, Phys. Rev. B, **65**, 214423 (2002); M. Ellouze, W. Boujelben, A. Cheikhrouhou, H. Fuess and R. Madar, Solid State Commun., **124**, 125 (2002).

23. A. Maignan, C. Martin, M. Hervieu, B. Raveau and J. Hejtmanek, Solid State Commun., **107**, 363 (1998); I. O. Troyanchuk, D. D. Khalyavin, S. V. Trukhanov and H. Szymczak, J. Phys.: Condens. Matter, **11**, 8707 (1999).

24. I. G. Deac, S. V. Diaz, B. G. Kim, S. W. Cheong, and P. Schiffer, Phys. Rev. B, **65**, 174426 (2002).

25. R. S. Freitas, L. Ghivelder, F. Damay, F. Dias and L. F. Cohen, Phys. Rev. B, **64**, 144404 (2001).

26. D. N. H. Nam, R. Mathieu, P. Nordblad, N. V. Khiem, and N. X. Phuc, Phys. Rev. B, **62**, 1027 (2000).

27. J. Lopez, P. N. Lisboa-Filho, W. A. C. Passos, W. A. Oritz, F. M. Araujo-Moreira, O. F. de Lima, D. Schaniel and K. Ghosh, Phys. Rev. B, **63**, 224422 (2001).

28. I. O. Troyanchuk, I. M. Kolesova, H. Szymczak and A. Nabialek, J. Mag. Mag. Mater., **176**, 267 (1997).

29. C. N. R. Rao, A. Arulraj, A. K. Cheetham and B. Raveau, J. Phys. Condens. Matter, **12**, R83 (2000).

30. H. Kuwahara, Y. Tomioka, A. Asamitgu, Y. Moritomo and Y. Tokura, Science **270**, 961 (1995).

31. P. V. Vanitha, R. S. Singh, S. Natarajan and C. N. R. Rao, J. Solid. State. Chem., **137**, 365 (1998).

32. P. V. Vanitha, A. Arulraj, A. R. Raju and C. N. R. Rao, C. R. Acad. Sci. Paris, **2**, 595 (1999).

33. C. N. R. Rao, P. N. Santosh, R. S. Singh and A. Arulraj, J. Solid. State. Chem., **135**, 169 (1998).

34. A. Arulraj, A. Biswas, A. K. Roychaudhuri, C. N. R. Rao, P. M. Woodward, T. Vogt, D. E. Cox and A. K. Cheetham, Phys. Rev. B, **57**, R8115 (1998).

35. S. Mori, C. H. Chen and S. W. Cheong, Phys. Rev. Lett., **81**, 3972 (1998).

36. P. V. Vanitha and C. N. R. Rao, J. Phys: Condens. Matter., **13**, 11707 (2001).

37. C. W. Chang, A. K. Debnath and J. G. Lin, Phys. Rev. B, **65**, 24422 (2001).

38. A. R. West, *Solid state chemistry and its applications* (John Wiley & Sons: Singapore, 2004); C. N. R. Rao and J. Gopalakrishnan (Eds), *New Directions in Solid State Chemistry*, 2nd edition (Cambridge University Press, 1997).

39. M. M. Seikh, Ph. D thesis, Indian Institute of Science, Bangalore (2005).

40. F. Licci, G. Turrili and P. Ferro, J. Mag. Mag. Mater., **164**, L268 (1996); M. Karooinen, M. Matvejeff, K. Salomaki and H. Yamauchi, J. Mater. Chem., **12**, 1761 (2002).

41. J. Magnusson, C. Djurberg, P. Granberg, and P. Nordblad, Rev. Sci. Instru. **68**, 3761 (1997).

42. R. Mathieu, P. Jonsson, D. N. H. Nam, and P. Nordblad, Phys. Rev. B **63**, 092401 (2001).

43. F. Damay, C. Martin, A. Maignan and B. Raveau, J. Appl. Phys., **82**, 6181 (1997).

44. J. A. Mydosh, in *"Spin Glasses: An Experimental Introduction"* Taylor and Francis, London (1993); K. Binder and A. P. Young, Rev. Mod. Phys., **58**, 801 (1986).

45. R. Mathieu, P. Nordblad, D. N. H. Nam, N. X. Phuc and N. V. Khiem, Phys. Rev. B, **63**, 174405 (2001).

46. D. S. Fisher, and D. A. Huse, Phys. Rev. B, **38**, 373 (1988).

47. M. Itoh, I. Natori, S. Kubota, and K. Matoya, J. Phys. Soc. Japan, **63**. 1486 (1994); D. N. H. Nam, K. Jonason, P. Nordblad, N. V. Khiem and N. X. Phuc, Phys. Rev. B, **59**, 4189 (1999).

48. Y. Moritomo, Phys. Rev. B, **60**, 10374 (1999).

3. ELECTRONIC PHASE SEPARATION AND RELATED ASPECTS OF RARE EARTH COBALTATES ($Ln_{1-x}A_xCoO_3$)

SUMMARY*

Investigations have been carried out on magnetic and electron transport properties of the following four series of rare earth cobaltates: $La_{0.7-x}Ln_xCa_{0.3}CoO_3$ (Ln = Pr, Nd, Gd and Dy). These materials were first studied in the form of polycrystalline pellets. Compositions close to $x = 0.0$ contain large ferromagnetic (FM) clusters or domains, and show Brillouin-like features of the field-cooled magnetization with fairly high values of ferromagnetic T_C. They also exhibit low electrical resistivities with near-zero temperature coefficients. When $x > 0.0$, however, the zero-field-cooled magnetization generally shows non-monotonic behavior with a peak slightly below T_C. The ac-susceptibility data show a prominent peak corresponding to the T_C near $x = 0.0$ compositions. The ferromagnetic T_C varies linearly with x or the average radius of the A-site cations, $\langle r_A \rangle$. With an increase in x or a decrease in $\langle r_A \rangle$, the magnetization value at any given temperature markedly decreases. Ac-susceptibility measurements show a prominent transition arising from-

*Based on these studies, papers have been published in: J. Phys.: Condens. Matter **6** 415 (2004), J. Magn. Magn. Mater. **281** 261 (2004), J. Phys. Chem. Solids **65** 95 (2004), J. Phys.: Condens. Matter **16** 7955 (2004), Solid State Comm. **134** 307 (2005), Phys. Rev. B **72** 144423 (2005), J. Solid State Chem. **179** 923 (2006).

small magnetic clusters having slight spin-glass characteristics. Electrical resistivity increases with increase in x, showing a significant increase around a critical value of x or $\langle r_A \rangle$, at which composition the small clusters also begin to dominate. These properties can be understood in terms of a phase separation scenario wherein large magnetic clusters give way to smaller clusters with increase in x, with both types of clusters being present in certain compositions. The changes in magnetic and electrical properties occur simultaneously because the large FM clusters are hole-rich and the small clusters are hole-poor. Moreover, variable-range-hopping appears to occur at low temperatures.

The above studies reveal that the properties of $Ln_{0.7}Ca_{0.3}CoO_3$ are strongly influenced by the $\langle r_A \rangle$ value. Thus, unlike $La_{0.7}Ca_{0.3}CoO_3$, $Pr_{0.7}Ca_{0.3}CoO_3$ and $Nd_{0.7}Ca_{0.3}CoO_3$ do not show distinct FM transitions; instead, they exhibit weak magnetic transitions, even at low temperatures. A detailed study of the magnetic properties of polycrystalline $Pr_{0.7}Ca_{0.3}CoO_3$ and $Nd_{0.7}Ca_{0.3}CoO_3$ shows that the materials are magnetically inhomogeneous, exhibiting properties similar to those of frustrated magnetic systems. In both of these cobaltates, small FM clusters are apparently embedded in the antiferromagnetic (AFM) matrix.

The results of our investigations of polycrystalline $La_{0.7}Ca_{0.3}CoO_3$ motivated us to study the magnetic and electron transport properties of single crystalline $La_{0.7}Ca_{0.3}CoO_3$ in detail. This oxide attains a spontaneous FM moment below 170 K and exhibits a re-entrant spin-glass behavior below 100 K. In the ordered and the re-entrant phases, the low-field magnetic properties are strongly direction dependent, showing considerably higher magnetization values perpendicular to the c-axis than parallel. Magnetic relaxation measurements show that both the FM and the re-entrant spin-glass phases are non-

equilibrium states, where the system exhibits magnetic aging that is characteristic of spin-glasses, as well as disordered and frustrated ferromagnets.

To examine the effect of small A-site cations on the magnetic properties of $Ln_{0.7}Ca_{0.3}CoO_3$, we have investigated single-crystalline $Pr_{0.7}Ca_{0.3}CoO_3$ and $Nd_{0.7}Ca_{0.3}CoO_3$ using low-field dc-magnetization, ac-susceptibility, magnetic-relaxation and memory effect measurements. Both $Pr_{0.7}Ca_{0.3}CoO_3$ and $Nd_{0.7}Ca_{0.3}CoO_3$ show frequency-dependent transitions at 70 and 55 K, respectively, in the ac-susceptibility data, which is associated with the onset of spin-glass behavior. Their magnetic relaxation behavior exhibits age dependence effects, and memory effects are found in the ZFC-magnetization behavior. These characteristics establish spin-glass behavior in both these cobaltates, which is distinctly different from that of $La_{0.7}Ca_{0.3}CoO_3$ and $La_{0.5}Sr_{0.5}CoO_3$ where a well-defined FM transitions occur, albeit without long-range ordering.

We have also investigated the magnetic and electron transport properties of $Gd_{0.5}Ba_{0.5}CoO_3$ for a comparison with the analogous FM cobaltates such as $Ln_{0.5}A_{0.5}CoO_3$ (Ln = La, Nd and A = Ba, Sr). Our results show that $Gd_{0.5}Ba_{0.5}CoO_3$, which exhibits A-site cation ordering at room temperature, does not become a genuine ferromagnet at low temperatures. The FM phase observed at 280 K changes to an AFM state on cooling to 230 K. The AFM state is rendered to FM state on the application of high magnetic fields. Such properties can be understood on the basis of phase separation induced by the large A-site cation-disorder, due to the size mismatch.

We have also investigated three series of cobaltates $Gd_{0.5-x}Ln_xBa_{0.5}CoO_3$ (Ln = La and Nd) and $La_{0.5-x}Nd_xBa_{0.5}CoO_3$ to demonstrate the effect of $\langle r_A \rangle$ on the magnetic and electrical properties. Thus, the anomalous magnetic properties of $Gd_{0.5}Ba_{0.5}CoO_3$ (such as

the transitions in the range 220-290 K) disappear, even with a small substitution of La or Nd in place of Gd, and a gradual evolution of ferromagnetism occurs at low temperatures (130 - 190 K). On the other hand, $Gd_{0.5}Ba_{0.5-x}Sr_xCoO_3$ shows increasing FM properties with the increase in x, despite the decrease in $\langle r_A \rangle$, suggesting the novel role of size-disorder. Studies of $Ln_{0.5-x}Ln'_xA_{0.5-y}A'_yCoO_3$ with fixed $\langle r_A \rangle$ values 1.317 and 1.289 Å (with the latter corresponding to $Gd_{0.5}Ba_{0.5}CoO_3$) reveal that, on decreasing the size-disorder, the materials become FM with relatively higher T_C values. These cobaltates also exhibit size-disorder controlled insulator-metal transitions, wherein the compositions with higher disorder are insulators.

Magnetic and electron transport properties of $Ln_{0.5}Ba_{0.5}CoO_3$ with Ln = Dy and Er have been studied to examine the effects of large cation size-disorder. The Dy compound shows a small magnetic anomaly around 290 K, similar to the Gd-derivative, whereas the Er compound is essentially paramagnetic due to the large cation size-disorder. The physical properties of $Dy_{0.5}Ba_{0.5}CoO_3$ are consistent with the presence of size-disorder in $Gd_{0.5}Ba_{0.5}CoO_3$ and it appears that such size-disorder give rise to electronic phase separation in these systems. Compositions with the same $\langle r_A \rangle$ (as in $Dy_{0.5}Ba_{0.5}CoO_3$ and $Er_{0.5}Ba_{0.5}CoO_3$) but with smaller size-disorder show progressive evolution of ferromagnetism and metallic properties with decreasing size-disorder parameter, σ^2.

3.1 INTRODUCTION

The physical properties of the rare earth cobaltates $Ln_{1-x}A_xCoO_3$ (Ln = trivalent rare earth and A = divalent alkaline earth) are somewhat similar to that of the rare earth manganates. Due to their fascinating physical properties, considerable research has been carried out on rare earth cobaltates for last few decades [1-6]. Unlike perovskite manganates, the rare earth cobaltates show spin-state transitions. The growth of interest in perovskite cobaltates $LaCoO_3$ and $La_{1-x}A_xCoO_3$ is due to the expectation that, in addition to the lattice, charge and spin degrees of freedom found in many other transition metal oxides, the cobalt oxides also display a degree of freedom in the "spin-state" at the cobalt site. One of the fundamental aspects of the transition metal chemistry is ligand field theory, which provides the possible explanation for the spin-state transitions of rare earth cobaltate. For a particular cobalt ion, when the ligand field strength is progressively increased by chemical means, a change from a high-spin to a low-spin ground state occurs at the cobalt ion. Such a change can also occur by the application of some other external perturbation without any chemical composition change. This perturbation induced electronic spin-state transition in rare earth cobaltates has been of great interest in recent years. Perturbations which can initiate such a spin-state transition may be temperature, pressure or some other factors [4-6]. The spin-state transition was reported in $LaCoO_3$ several years ago [1-3]. Other rare earth cobaltates also show evidence for a spin-state transition. Moreover, the transition temperature increases with a decrease in rare earth ion size [2].

Magnetic and electron transport properties of $LaCoO_3$ as a function of temperature have been investigated by several researchers for the last few decades [1, 3]. The physical properties of the cobaltates are sensitive to doping concentration at the rare earth site. Accordingly, the other parameters such as the average radius of the A-site cation, $\langle r_A \rangle$, and size-disorder parameter, σ^2, also vary due to doping at the rare earth site. These parameters crucially control the rare earth cobaltate properties, which are similar to the manganates [7, 8]. In the $La_{1-x}Sr_xCoO_3$ system, the studies till date have concentrated on the observed competition between ferromagnetism and cluster/spin-glass behavior. Doping with Sr^{2+} introduces hole into the system. It also introduces size variance in the A-site, which has been shown to affect the physical properties of cobaltates as discussed in first chapter. Studies on $La_{1-x}Ca_xCoO_3$ samples have suggested that there are no major differences from the Sr-doped system. Ferromagnetism is observed in both systems, with the Curie temperature being lower in Ca-doped materials at a fixed doping level. Magnetic and electron transport properties of different rare earth cobaltates have been investigated to examine the effect of $\langle r_A \rangle$ and σ^2 on these systems. Thus, while $La_{0.7}Ca_{0.3}CoO_3$ ($\langle r_A \rangle$ = 1.354 Å) shows ferromagnetism associated with metallicity at low temperature, $Ln_{0.7}Ca_{0.3}CoO_3$ with a smaller $\langle r_A \rangle$ of 1.179 Å (Ln = Pr) and 1.168 Å (Ln = Nd) shows no long-range ferromagnetism or insulator-metal transition [9]. Instead, the latter two systems exhibit electronic phase separation and/or spin-glass like behavior at low temperatures. A detailed study on rare earth cobaltates has shown the occurrence of electronic phase separation and glassy magnetic behavior for small $\langle r_A \rangle$, and a large σ^2 value. There is growing interest for small $\langle r_A \rangle$, rare earth cobaltates of the type Ln_1.

$_xSr_xCoO_3$ due to their fascinating physical properties. Recently, Kobayashi et al [5] have also reported the existence of room temperature ferromagnetism in this type of system.

3.2 SCOPE OF THE PRESENT INVESTIGATIONS

We present the results of our investigations on rare earth cobaltates in this section. Specifically, we explore the effect of A-site cation radius and size-disorder on the electron transport properties, as well as the factors that influence the electronic phase separation and/or spin-glass behavior.

3.2.1 Magnetic and electron transport properties of the rare-earth cobaltates, $La_{0.7-x}Ln_xCa_{0.3}CoO_3$ (Ln = Pr, Nd, Gd and Dy): A case of phase separation

It has been reported by several researchers [7, 10-12] that the rare earth manganates $La_{0.7-x}Ln_xCa_{0.3}MnO_3$ (Ln = Pr, Nd, Gd and Y) undergo electronic phase separation beyond a critical composition x_c. The $x < x_c$ compositions exhibit ferromagnetism and metallicity; however, for $x > x_c$, the materials become non-magnetic insulators and experience a sharp decline in magnetic moment [10-13]. Such property changes despite the constant carrier concentration or Mn^{4+}/ Mn^{3+} ratio are indeed noteworthy. Accordingly, many of the rare earth cobaltates show ferromagnetism and metallicity, depending on the composition and the A-site cation size. The cobaltates also show some unusual features in their magnetic properties, as discussed in previous sections. For example, Itoh et al [14] have reported a spin-glass behavior in $La_{1-x}Sr_xCoO_3$ when $0.0 \leq x \leq 0.18$ and a cluster-glass behavior when $0.18 \leq x \leq 0.5$. Ganguly et al [15] reported long-range freezing of super-paramagnetic clusters when $x < 0.3$. For $x = 0.5$, a

cluster-glass magnetic behavior has been reported by Kumar et al [16], who ascribed this property to magneto-crystalline anisotropy. Wu et al [17] suggested that $La_{1-x}Sr_xCoO_3$ is best described as being dominated by glassy ferromagnetism and magnetic phase separation. Similarly, Burley et al [18] reported long-range ferromagnetism and glassiness in $La_{1-x}Ca_xCoO_3$, as well as a structural phase transition for $x > 0.1$.

We considered it important to investigate the magnetic and electron transport properties of $La_{0.7-x}Ln_xCa_{0.3}CoO_3$ (Ln = Pr, Nd, Gd and Dy), in view of the comparable nature of the cobaltates and the manganates, and also because of the likelihood that phase separation may occur in the cobaltate system as well because of the presence of strongly correlated electrons [7]. While the carrier concentration remains constant in $La_{0.7-x}Ln_xCa_{0.3}CoO_3$, the $\langle r_A \rangle$ and the associated factors vary. Furthermore, the Ca-substituted cobaltates were considered more likely to exhibit phase separation and related effects due to the smaller $\langle r_A \rangle$ or the e_g band-width compared to the Sr-substituted materials. We first studied the physical properties of $La_{0.7-x}Ln_xCa_{0.3}CoO_3$ in the form of polycrystalline pellets.

Properties of the rare earth manganates of $Ln_{1-x}A_xMnO_3$ are crucially controlled by the $\langle r_A \rangle$ [7, 8, 19-21]. For example, $La_{0.7}Ca_{0.3}MnO_3$ ($\langle r_A \rangle$ = 1.205 Å) shows an insulator to metal transition and ferromagnetism, with the metallicity being associated with ferromagnetism at low temperatures [7, 19, 22], $Pr_{0.7}Ca_{0.3}MnO_3$ with a smaller $\langle r_A \rangle$ of 1.179 Å shows no ferromagnetism or insulator to metal transition. Instead, it exhibits charge ordering, orbital ordering and electronic phase separation [7, 19, 23]. We were interested in exploring whether the analogous cobaltates $Ln_{1-x}A_xCoO_3$ exhibit similar features. In these cobaltate systems, the $x = 0.3$ composition is FM and metallic when Ln

= La and A = Sr or Ca [14, 24-28] and also when Ln = Pr and A = Sr [13, 28-30]. These properties essentially arise because of the presence of Co^{3+}-O- Co^{4+} states, where both Co^{3+} and Co^{4+} possibly being in the intermediate-spin states [24, 31]. Electron transfer between the Co^{3+} and Co^{4+} ions is rapid and the materials are considered to be itinerant electron ferromagnets. The cluster-glass behavior has also been observed at low temperatures in these materials [14], but this has not been entirely established [25, 27]. We considered it important to investigate the properties of polycrystalline $Pr_{0.7}Ca_{0.3}CoO_3$ and $Nd_{0.7}Ca_{0.3}CoO_3$, with smaller $\langle r_A \rangle$ values of 1.179 and 1.168 Å respectively, to examine how their properties vary from those of $La_{0.7}Ca_{0.3}CoO_3$.

3.2.2 Non-equilibrium magnetic properties of single crystalline rare earth cobaltates, $Ln_{0.7}Ca_{0.3}CoO_3$ (Ln = La, Pr and Nd)

Previous investigations of the magnetic and electron transport properties of the polycrystalline samples of $La_{0.7-x}Ln_xCa_{0.3}CoO_3$ (Ln = Pr, Nd, Gd and Dy) reinforce the phase-separation scenario with the coexistence of large carrier-rich FM clusters and carrier-poor smaller clusters. The parent compound $La_{0.7}Ca_{0.3}CoO_3$ shows a divergence between ZFC and FC magnetization, and the $M_{FC}(T)$ curve does not show saturation even at low temperatures. In order to fully understand the unusual behavior of $La_{0.7}Ca_{0.3}CoO_3$, we have carried out detailed magnetic measurements on single crystal sample at very low fields and also along different crystallographic directions. More importantly, we have studied the magnetic relaxation to throw light on the nature of phase separation. The study has revealed that the FM phase below 170 K is a non-equilibrium phase similar to that observed in prototype re-entrant ferromagnets while below 100 K a low-temperature re-entrant spin-glass phase emerges.

Rare earth cobaltates $Ln_{1-x}A_xCoO_3$ show interesting magnetic and electron transport properties those are sensitive to the $\langle r_A \rangle$ [28, 31]. Some compositions show ferromagnetic characteristics, but the ferromagnetism in these materials is generally not associated with long-range order [14]. Magnetic properties of these cobaltates are instead considered to be akin to those of cluster or spin-glasses [14, 17]. $La_{0.7}Ca_{0.3}CoO_3$ shows a behavior somewhat like a ferromagnetic material with a marked increase in magnetization around 170 K, $Pr_{0.7}Ca_{0.3}CoO_3$ and $Nd_{0.7}Ca_{0.3}CoO_3$ with smaller $\langle r_A \rangle$ values, do not show such distinct transitions [32]. The last two cobaltates exhibit low magnetization values down to low temperatures and an inhomogeneous magnetic behavior. In order to understand the nature of magnetism in these cobaltates, we have carried out a detailed study on single crystals at low fields along different directions, in addition to ac susceptibility and relaxation measurements. The study establishes that both $Pr_{0.7}Ca_{0.3}CoO_3$ and $Nd_{0.7}Ca_{0.3}CoO_3$ dynamically behave as spin-glasses at low temperatures.

3.2.3 Cation size-disorder as the crucial determinant of the unusual magnetic and electronic properties of $Gd_{0.5}Ba_{0.5}CoO_3$

The rare-earth cobaltates $Ln_{0.5}A_{0.5}CoO_3$ have been investigated extensively for the past several years [24, 28, 31, 33, 34]. A majority of the cobaltates, especially those with A = Sr, are FM and many of them exhibit metallic behavior. The ferromagnetic T_C in these cobaltates increases with the increase in $\langle r_A \rangle$. When A = Ba, ferromagnetism occurs with Ln = La, Pr and Nd, but when Ln = Gd, the material shows an unusual magnetic behavior. Furthermore, $Gd_{0.5}Ba_{0.5}CoO_3$ is an insulator, unlike $La_{0.5}Ba_{0.5}CoO_3$ which is metallic [35-38]. It has been pointed out that the $\langle r_A \rangle$ as well as the cation size-disorder

arising from the size mismatch play important roles in determining the properties of the cobaltates [38]. It is to be noted that the $\langle r_A \rangle$ and the variance σ^2, which measures the cation size-disorder [39], are 1.485 Å and 0.0156 Å^2, respectively, in $La_{0.5}Ba_{0.5}CoO_3$, compared to 1.289 Å and 0.033 Å^2 in the case of $Gd_{0.5}Ba_{0.5}CoO_3$. A careful examination of the literature on the magnetic and electronic properties of $Gd_{0.5}Ba_{0.5}CoO_3$ reveals some inconsistencies and do not provide a clear picture.

$Gd_{0.5}Ba_{0.5}CoO_3$ is reported to develop spontaneous magnetization around 280 K, but the magnetization drops sharply around 230 K to an antiferromagnetic state. The highest magnetization value or the highest magnetic moment achieved is rather small. The material is insulating at all temperatures and shows a resistivity transition around 350 K [37, 38]. There is some evidence for cation ordering in the Ba-substituted rare-earth cobaltates around this temperature [37, 38, 40]. The 280 K transition has been classified as FM or meta-magnetic. The magnetic transitions in $Gd_{0.5}Ba_{0.5}CoO_3$ and other cobaltates of this family such as $La_{0.5}(Nd_{0.5})Ba_{0.5}CoO_3$ have not been distinguished, and have all been treated as FM transitions. There are, however, considerable differences amongst these cobaltates. The magnetic transitions in $La_{0.5}(Nd_{0.5})Ba_{0.5}CoO_3$ are distinctly FM, showing a sharp increase in magnetization at T_C, and the T_C itself is rather low (130-190 K) [35, 38]. $Gd_{0.5}Ba_{0.5}CoO_3$, with a much smaller A-site cation, should have been associated with an even lower T_C. No definitive resistivity anomaly occurs at the 230 K magnetic transition, although it somewhat resembles the charge ordering transition in $Nd_{0.5}Sr_{0.5}MnO_3$ [41, 42]. Considering this experimental situation, we considered it important to carefully investigate the magnetic and electronic properties of $Gd_{0.5}Ba_{0.5}CoO_3$.

From the previous study, it is clear that, the large value of σ^2 in the $Gd_{0.5}Ba_{0.5}CoO_3$ (0.033 $Å^2$) compared to $La_{0.5}Ba_{0.5}CoO_3$ (0.016 $Å^2$) could be responsible for the absence of ferromagnetism and metallicity in the former. In order to understand the unusual properties of $Gd_{0.5}Ba_{0.5}CoO_3$, we have carefully investigated cobaltates of the type $Gd_{0.5-x}Ln_xBa_{0.5}CoO_3$ (Ln = La and Nd) and $Gd_{0.5}Ba_{0.5-x}Sr_xCoO_3$, wherein the $\langle r_A \rangle$ varies progressively with increase in *x*. The latter system is of particular interest because $Gd_{0.5}Sr_{0.5}CoO_3$ with a smaller $\langle r_A \rangle$ shows a FM transition (T_C ~ 140 K), unlike $Gd_{0.5}Ba_{0.5}CoO_3$. In addition, we have studied several cobaltate compositions, where $\langle r_A \rangle$ was kept constant, but the magnitude of size-disorder, σ^2, was varied. For this purpose, cobaltate compositions, $Ln_{0.5-x}Ln'_xA_{0.5-y}A'_yCoO_3$, with fixed $\langle r_A \rangle$ values of 1.317 and 1.289 Å corresponding to $Nd_{0.5}Ba_{0.5}CoO_3$ and $Gd_{0.5}Ba_{0.5}CoO_3$ respectively have been investigated. In these studies, we have determined the oxygen stoichiometry of the samples by redox titrations and ensured that none of the observed trends in the properties arise from the differences in the oxygen content. The present study established that the unusual properties of $Gd_{0.5}Ba_{0.5}CoO_3$ associated mainly with the disorder caused by the size mismatch between the Gd and Ba ions.

3.2.4 Effects of large cation size-disorder on the magnetic properties of the rare earth cobaltates, $Ln_{0.5}Ba_{0.5}CoO_3$ (Ln = Dy and Er)

Our detailed investigations of $Gd_{0.5}Ba_{0.5}CoO_3$ have revealed that its distinctive properties mainly arise due to the disorder caused by the size mismatch between A-site cations. If size-disorder plays such a crucial role in the $Ln_{0.5}Ba_{0.5}CoO_3$ cobaltate series, then rare earth ions of smaller than Gd should exhibit unusual magnetic and electrical properties. Therefore, it is possible that a very small rare earth ion in $Ln_{0.5}Ba_{0.5}CoO_3$ may

even eliminate the magnetic anomaly, rendering the material to be paramagnetic. In order to investigate the effect of increased size-disorder in $Ln_{0.5}Ba_{0.5}CoO_3$, we have studied the properties of $Dy_{0.5}Ba_{0.5}CoO_3$ and $Er_{0.5}Ba_{0.5}CoO_3$ with the σ^2 values of 0.037 and 0.042 $Å^2$, respectively. Additionally, we have examined the properties of $Gd_{0.5-x}Ln_xBa_{0.5}CoO_3$ (Ln = Dy, Er), wherein $\langle r_A \rangle$ decreases progressively with increasing x. In order to examine the effect of size-disorder quantitatively we have studied cobaltate compositions where $\langle r_A \rangle$ was kept constant, but σ^2 were varied. For this purpose, cobaltate compositions, $Ln_{0.5-x}Ln'_xA_{0.5-y}A'_yCoO_3$, with fixed $\langle r_A \rangle$ values of 1.277 and 1.266 Å corresponding to $Dy_{0.5}Ba_{0.5}CoO_3$ and $Er_{0.5}Ba_{0.5}CoO_3$ respectively have been investigated.

3.3 EXPERIMENTAL PROCEDURES

3.3.1 Synthesis of polycrystalline samples

Polycrystalline samples of the respective compositions were prepared by the conventional ceramic method as mentioned in chapter 2.3.1 (see page 57).

(i) Preparation of $La_{0.7-x}Ln_xCa_{0.3}CoO_3$ (Ln = Pr, Nd, Gd and Dy):

Polycrystalline samples of $La_{0.7-x}Ln_xCa_{0.3}CoO_3$ (Ln = Pr, Nd, Gd and Dy) were prepared by the conventional solid-state reaction method. Stoichiometric mixtures of the respective rare earth oxides, $CaCO_3$ and Co_3O_4 were weighed in desired proportions and milled for few hours with propanol. After the mixed powders were dried, they were calcined in air at 1223 K followed by heating at 1273 and 1373 K for 12 h in air. The powders thus obtained were pelletized and the pellets were sintered at 1473 K for 12 h in air. To improve the oxygen stoichiometry the samples were annealed in an oxygen atmosphere at a lower temperature ($\leq$ 1173 K). The oxygen stoichiometry was determined by iodometric titrations [43]. The estimated oxygen stoichiometry in the $Ln_{0.7}Ca_{0.3}CoO_{3-\delta}$ (Ln = La, Pr and Nd) were 2.97, 3.00 and 2.95, respectively, in the La, Pr and Nd derivatives. The oxygen stoichiometry in the other series of cobaltates was found to be 2.97 ± 0.03.

(ii) Preparation of $Ln_{0.5}Ba_{0.5}CoO_3$ (Ln = La, Nd, Gd, Dy and Er)

Polycrystalline samples of $Ln_{0.5}Ba_{0.5}CoO_3$ (Ln = La, Nd, Gd, Dy and Er) and $Gd_{0.5}Sr_{0.5}CoO_3$, were prepared by the conventional ceramic method. Stoichiometric

mixtures of the respective rare earth oxides, alkaline earth carbonates and Co_3O_4 were weighed in desired proportions and milled for few hours with propanol. The mixtures were dried, and calcined in air at 1173 K followed by heating at 1273 and 1373 K for 12 h in air. The powders thus obtained were pelletized and the pellets were sintered at 1473 K for 12 h in air. To improve the oxygen stoichiometry the samples were annealed in an oxygen atmosphere at a lower temperature (< 1073 K). The oxygen stoichiometry was determined by iodometric titrations [43]. The oxygen stoichiometry in the $Ln_{0.5}Ba_{0.5}CoO_{3-\delta}$ (Ln = La, Nd, Gd, Dy and Er) studied by us was generally around 2.95 ± 0.05. The estimated oxygen contents are 2.95, 2.94, 2.90, 2.91 and 2.90 in the La, Nd, Gd, Dy and Er derivatives respectively. In $Gd_{0.5}Sr_{0.5}CoO_3$, the exact oxygen stoichiometry was 2.95.

(iii) Preparation of $Gd_{0.5-x}Ln_xBa_{0.5}CoO_3$ (Ln = La, Nd, Dy and Er), $La_{0.5-x}Nd_xBa_{0.5}CoO_3$ and $Gd_{0.5}Ba_{0.5-x}Sr_xCoO_3$

Polycrystalline samples of $Gd_{0.5-x}Ln_xBa_{0.5}CoO_{3-\delta}$ (Ln = La, Nd, Dy and Er), $La_{0.5-x}Nd_xBa_{0.5}CoO_{3-\delta}$ and $Gd_{0.5}Ba_{0.5-x}Sr_xCoO_{3-\delta}$ were prepared by the conventional ceramic method. Stoichiometric mixtures of the respective rare earth oxides, alkaline earth carbonates and Co_3O_4 were weighed in desired proportions and milled for few hours with propanol. After the mixed powders were dried, they were calcined in air at 1173 K followed by heating at 1273 and 1373 K for 12 h in air. The powders, thus obtained were pelletized and the pellets were sintered at 1473 K for 12h in air. To improve the oxygen stoichiometry the samples were annealed in an oxygen atmosphere at a lower temperature (< 1073 K). The oxygen stoichiometry in the cobaltates prepared by us was around 2.94 ± 0.06.

3.3.2 Preparation of single-crystalline samples

Floating zone melting technique:

It is well known that polycrystalline samples are easier to prepare as compared to single crystal materials. Inspite of that researcher are interested in preparation of high quality single crystals which eliminate the impurities and defects in the material. There are several methods to grow single crystals: the Czochralski method, flux method, skull melting and Bridgman and Stockbarger methods [44]. The most popular technique for rare earth manganates and cobaltates single crystal, however, is the floating zone melting technique. The advantage of this technique is that it does not require any container; therefore, the contamination from the container wall is completely avoided. Moreover, the uniform distribution of chemical constituents can be obtained by eliminating heterogeneous nucleation.

Figure 3.1 shows the schematic diagram of the floating zone image furnace. The furnace used in the present study was SC-M35HD, Nichiden Machinery Ltd., Japan. It consists of a pair of halogen lamps to generate infrared radiation, a pair of ellipsoidal mirror to focus the radiation onto the sample, a quartz tube enclosing the floating region for maintaining the required atmosphere, and two pulleys that can move independently or in a synchronized manner to control the growth rate. The growth rate can be varied from 0.1-99 mm/h. The maximum lamp temperature can be achieved upto 2400 K and the corresponding maximum pressure inside the quartz tube is of six atmosphere pressure. Infrared radiation coming from a pair of halogen lamps is focused onto the polycrystalline rods by using a pair of gold coated concave ellipsoidal mirrors.

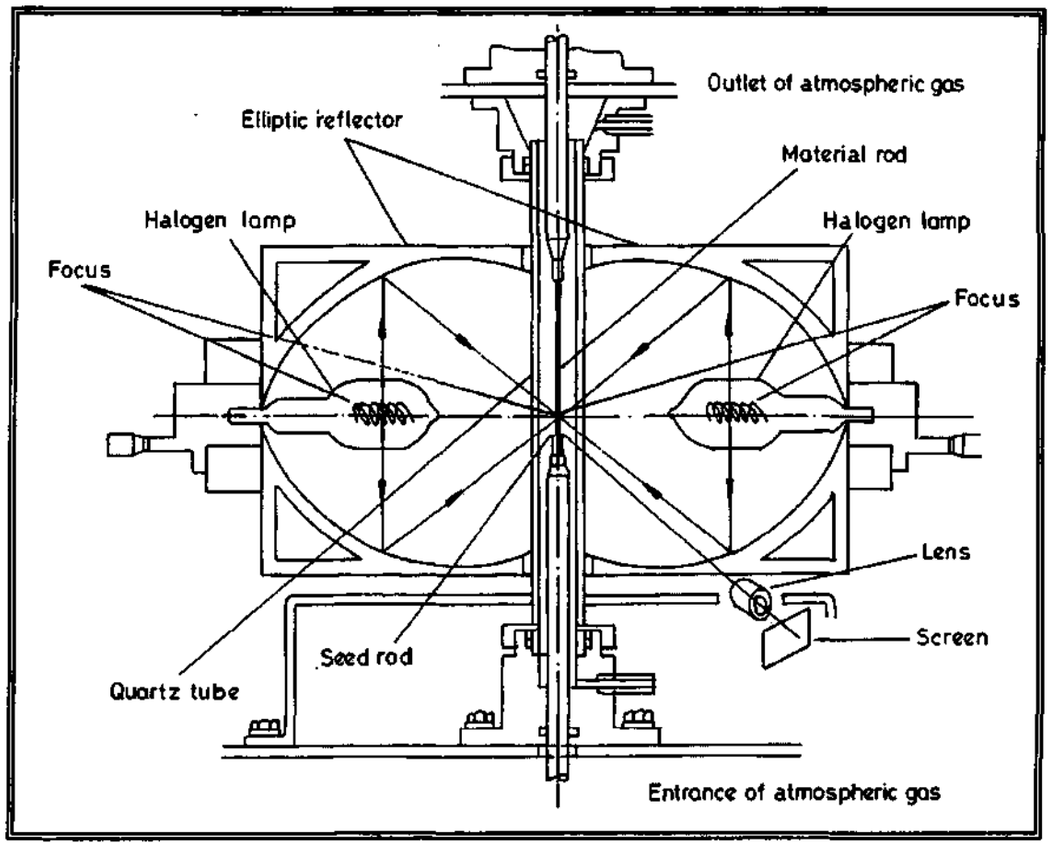

Figure 3.1 The cross section of the floating zone melting furnace

At the focal point the rods melt. The melts between the two connecting feed and seed rods are held by surface tension force without any other support and hence the name floating zone melting technique. The stability of the molten zone can be controlled by changing the temperature, pressure, atmosphere, rod rotation speed and molten zone pulling rate. Fig. 3.2 shows the schematic presentation of different stages of the crystal growth using the floating zone furnace.

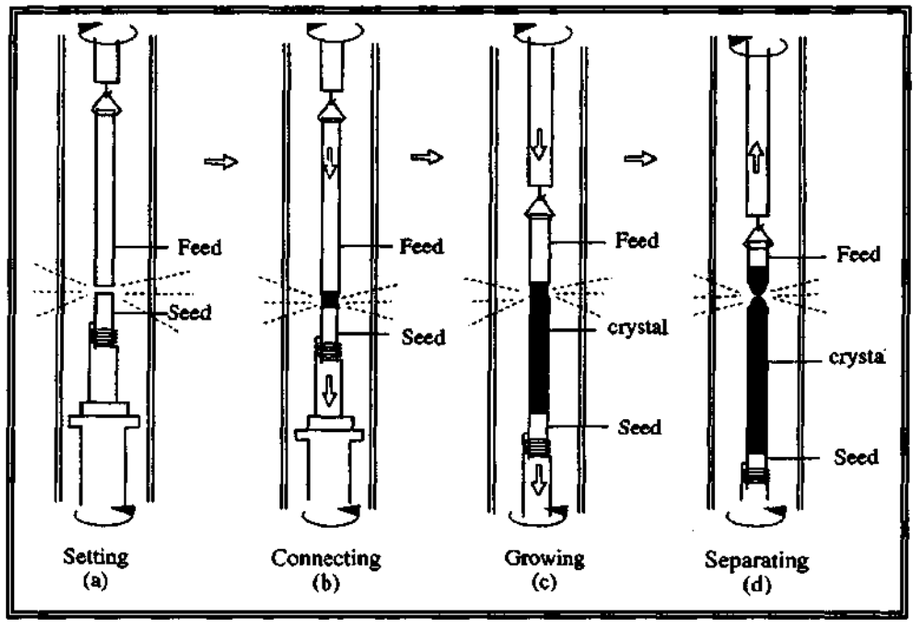

Figure 3.2 Crystal growths inside the furnace

Fig. 3.3 shows the image of a crystal grown by the floating zone melting technique, in an oxygen atmosphere with a growth rate of 7 mm/h. The crystal diameter is generally 4 mm and length is around 25 mm.

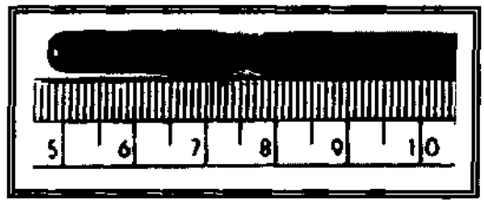

Figure 3.3 Image of $La_{0.7}Ca_{0.3}CoO_3$ single crystal

(i) Preparation of $La_{0.7}Ca_{0.3}CoO_3$

We used a floating-zone furnace to grow a $La_{0.7}Ca_{0.3}CoO_3$ single crystal. Polycrystalline rods (feed and seed) were prepared by conventional solid-state reaction

method as discussed in the preceding section. Stoichiometric mixtures of the starting materials La_2O_3, $CaCO_3$ and Co_3O_4 were weighed in the desired proportions and milled for a few hours. After the mixed powder was dried, it was calcined in air at 1223 K and after few intermediate grinding the powder was finally sintered at 1473 K for 24 h in air. The sample was then reground and mono-phasic polycrystalline powder was hydrostatically pressed and sintered at 1473 K for 24 h in air to obtain feed and seed rods with a diameter of 4 mm and a length of 100 mm. The single crystal was then grown under an oxygen flow of 3 lit/min at a growth rate of 7 mm/h. A part of the crystal was cut off and ground to a fine powder on which an X-ray diffraction was measured.

(ii) Preparation of $Pr_{0.7}Ca_{0.3}CoO_3$ and $Nd_{0.7}Ca_{0.3}CoO_3$

Single crystals of $Pr_{0.7}Ca_{0.3}CoO_3$ and $Nd_{0.7}Ca_{0.3}CoO_3$ were grown by the floating-zone furnace. The polycrystalline rods (feed and seed) were prepared by conventional the solid-state reaction method, starting with stoichiometric mixtures of the rare earth oxides, with $CaCO_3$ and Co_3O_4. The monophasic polycrystalline powders were hydrostatically pressed and sintered at 1473 K for 24 h in air to obtain feed and seed rods with a diameter of 3-4 mm and a length of 90-100 mm. Single crystals were grown under an oxygen flow of 2-4 lit/min at a growth rate of 3-7 mm/h. A small part of the crystals were cut off and ground to fine powder on which an X-ray diffraction was measured.

3.3.3 Characterization

The phase purity, composition analysis and the physical properties of the polycrystalline and single crystal samples were established by various techniques, which have been discussed in the experimental section of chapter 2.3.2 (see page 58).

3.4 RESULTS AND DISCUSSION

3.4.1 Magnetic and electron transport properties of the rare-earth cobaltates, $La_{0.7-x}Ln_xCa_{0.3}CoO_3$ (Ln = Pr, Nd, Gd and Dy): A case of phase separation

The crystal structure and lattice parameters of polycrystalline $La_{0.7-x}Ln_xCa_{0.3}CoO_3$ (Ln = Pr, Nd, Gd and Dy) cobaltates are presented in Table 3.1 along with the $\langle r_A \rangle$ value. The $\langle r_A \rangle$ values were calculated using the Shannon radius for 12-coordination in the case of rhombohedral cobaltates and for 9-coordination in the case of the orthorhombic ones.

Table 3.1 Crystal structures of $La_{0.7-x}Ln_xCa_{0.3}CoO_3$ (Ln = Pr, Nd, Gd and Dy)

Composition x	$\langle r_A \rangle$ (Å)	Space group	Lattice parameters (Å)			V (Å^3)
			a	b	c	
0.0	1.354	$R\bar{3}C$	5.3906	—	—	111.6
			Ln = Pr			
0.1	1.347	$R\bar{3}C$	5.3869	—	—	111.2
0.2	1.340	$R\bar{3}C$	5.3837	—	—	111.0
0.3	1.194	*Pnma*	5.3836	7.5858	5.3679	219.2
0.5	1.187	*Pnma*	5.3723	7.5686	5.3663	218.2
0.6	1.183	*Pnma*	5.3652	7.5731	5.3593	217.8
0.7	1.179	*Pnma*	5.3577	7.5774	5.3436	216.9
			Ln = Nd			
0.1	1.345	$R\bar{3}C$	5.3784	—	—	110.7
0.2	1.336	$R\bar{3}C$	5.3761	—	—	110.6
0.3	1.189	*Pnma*	5.3795	7.5867	5.3732	219.3
0.4	1.184	*Pnma*	5.3700	7.5741	5.3642	218.4
0.49	1.179	*Pnma*	5.3667	7.5766	5.3641	218.1
0.7	1.168	*Pnma*	5.346	7.5638	5.3287	215.5
			Ln = Gd			
0.1	1.338	$R\bar{3}C$	5.3797	—	—	110.7
0.2	1.322	$R\bar{3}C$	5.3785	—	—	110.4
0.24	1.179	*Pnma*	5.3838	7.5846	5.3797	219.7
0.3	1.1725	*Pnma*	5.3813	7.5814	5.3624	218.8
			Ln = Dy			
0.1	1.337	$R\bar{3}C$	5.3759	—	—	110.1
0.195	1.179	*Pnma*	5.3960	7.5990	5.3729	220.3
0.3	1.165	*Pnma*	5.3813	7.5783	5.3583	218.5

In Fig. 3.4, we show the temperature dependence of the dc magnetization of a few compositions of polycrystalline $La_{0.7-x}Ln_xCa_{0.3}CoO_3$ (Ln = Pr, Nd). Both the ZFC and FC magnetization data are shown in the figure. The FC curve of the x = 0.0 composition shows a Brillouin-type temperature dependence, and a T_C value of around 170 K. With increase in x, the ZFC data show lower magnetization values and a non-monotonic behavior. Accordingly, we see a peak in the ZFC data, at a temperature, T_P, the peak temperature being slightly lower than the T_C value from the FC data. The maximum value of the magnetization attained as well as the apparent T_C value decrease with increasing x or decreasing $\langle r_A \rangle$. At large x, we notice the appearance of a shoulder-like feature in the magnetization curve, the feature becoming clearly noticeable at $x \geq 0.6$ and $x \geq 0.4$ respectively in the Pr- and Nd-substituted series of cobaltates.

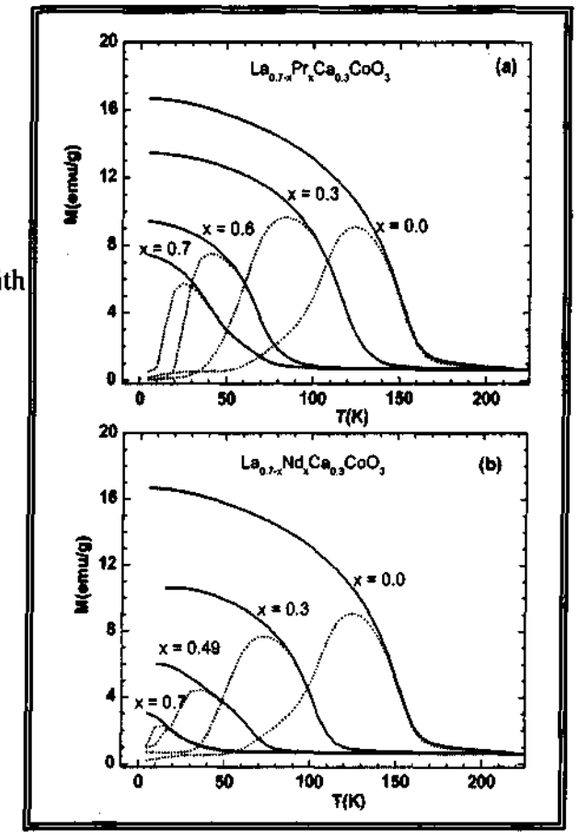

Figure 3.4 Temperature variation of the magnetization of $La_{0.7-x}Ln_xCa_{0.3}CoO_3$ with (a) Ln = Pr and (b) Ln = Nd. ZFC data in broken curves and FC data in solid curves (at 1 kOe).

Accordingly, ac-susceptibility measurements of $La_{0.7}Ca_{0.3}CoO_3$ (x = 0.0, $\langle r_A \rangle$ = 1.354 Å) show one major frequency-independent transition around 150 K corresponding to the FM transition, while $Pr_{0.7}Ca_{0.3}CoO_3$ (x = 0.7, $\langle r_A \rangle$ = 1.179 Å) shows two distinct transitions, the low temperature one with a greater frequency dependence as shown in Fig. 3.5(c). $La_{0.4}Pr_{0.3}Ca_{0.3}CoO_3$ ($\langle r_A \rangle$ = 1.194 Å) also shows a single transition corresponding to the T_C which is frequency independent just as $La_{0.7}Ca_{0.3}CoO_3$. The frequency-independent high-temperature transition in $Pr_{0.7}Ca_{0.3}CoO_3$ is due to the large magnetic clusters (the so-called cluster-glass [14, 31]) as in the x = 0.0 composition and the low-temperature transition is due to small magnetic clusters which seem to show some spin-glass characteristics. Thus, with the increase in x or decrease in $\langle r_A \rangle$ in the $La_{0.7-x}Ln_xCa_{0.3}CoO_3$ system, the large ferromagnetic clusters seem to progressively give way to the small clusters, giving rise to magnetic phase separation.

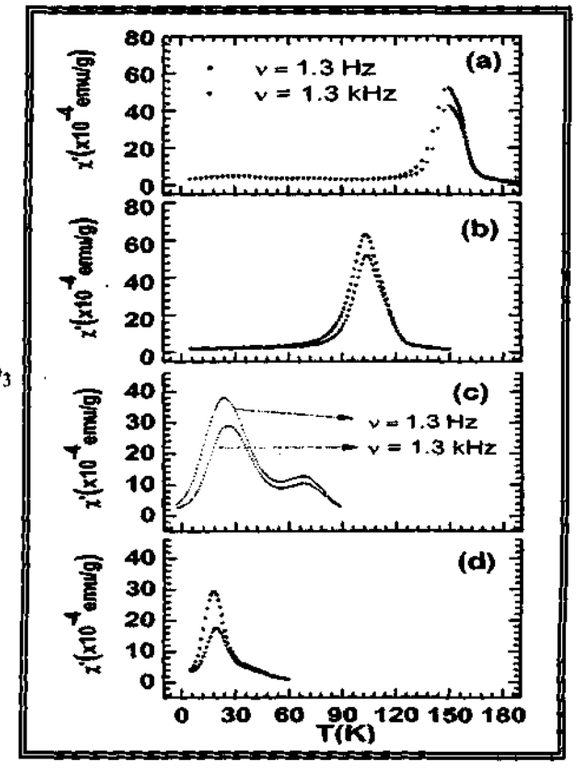

Figure 3.5 Temperature variation of the ac-susceptibility of (a) $La_{0.7}Ca_{0.3}CoO_3$ (b) $La_{0.4}Pr_{0.3}Ca_{0.3}CoO_3$ (c) $Pr_{0.7}Ca_{0.3}CoO_3$ and (d) $Nd_{0.7}Ca_{0.3}CoO_3$ at two different frequencies.

The presence of very weak features at low temperatures in the ac-susceptibility data of $La_{0.7}Ca_{0.3}CoO_3$ (Fig 3.5(a)) indicates that the proportion of small clusters is negligible at $x = 0.0$. In $Nd_{0.7}Ca_{0.3}CoO_3$, on the other hand, we only see a frequency-dependent low-temperature transition around 20 K due to the small magnetic clusters (Fig. 3.5(d)).

The magnetic properties of the Gd- and Dy-substituted compositions, $La_{0.7-x}Ln_xCa_{0.3}CoO_3$ (Ln = Gd, Dy) shown in Fig. 3.6 are similar to those of the Pr- and Nd-substituted compositions, except that at low temperatures (< 30 K) an increase in magnetization is noticed. Such an increase arising from the contribution from the Gd and Dy ions has been observed earlier [45].

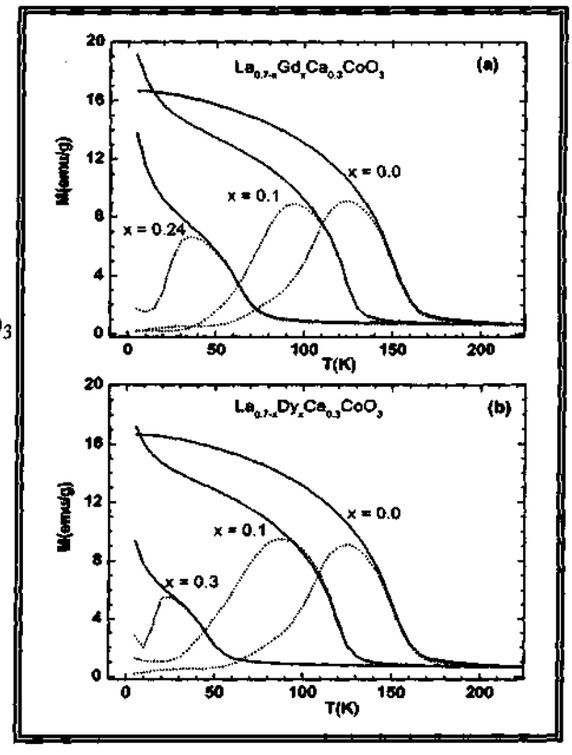

Figure 3.6 Temperature variation of the magnetization of (a) $La_{0.7-x}Gd_xCa_{0.3}CoO_3$ and (b) $La_{0.7-x}Dy_xCa_{0.3}CoO_3$. ZFC data in broken curves and FC data in solid curves (1 kOe).

The T_C values obtained from FC magnetization data in the four series of cobaltates are plotted against x in Fig. 3.7. The T_C value decreases linearly with increasing x. These data can be rationalized in terms of the average radius of A-site

cations, $\langle r_A \rangle$. Thus, a plot of T_C versus $\langle r_A \rangle$ is sensibly linear as can be seen from the inset of Fig. 3.7.

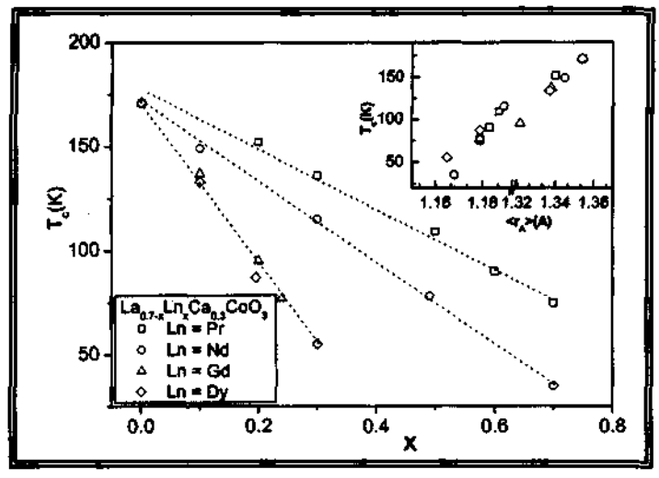

Figure 3.7 Variation of the ferromagnetic T_C with x in-$La_{0.7-x}Ln_xCa_{0.3}CoO_3$. The inset shows the variation of T_C with $\langle r_A \rangle$ (Å).

We have recorded M-H curves of the four series of cobaltates and show typical data for two series of compounds in Fig. 3.8. The hysteresis curves do not show saturation in all the compositions. The absence of saturation is a characteristic of a glassy system.

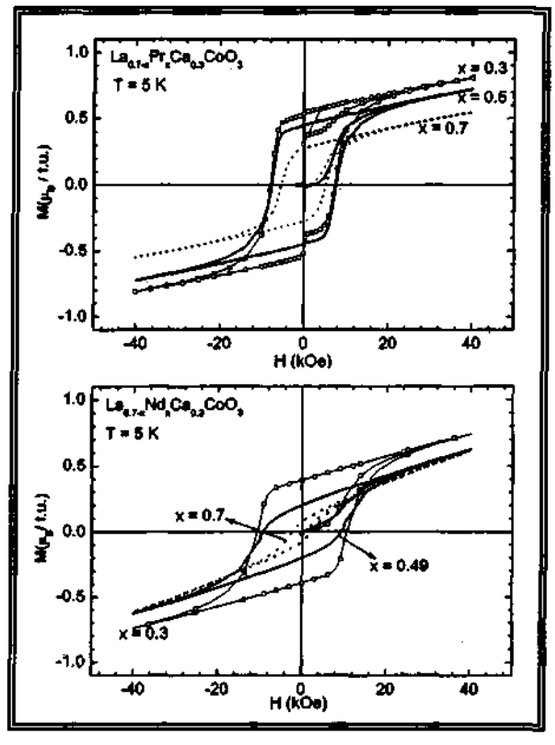

Figure 3.8 Typical hysteresis curves of $La_{0.7-x}Ln_xCa_{0.3}CoO_3$ at 5 K (Ln = Pr, Nd).

Furthermore, the remanent magnetization, M_r, decreases with increase in x or decrease in $\langle r_A \rangle$. We have plotted M_r at 50 K against $\langle r_A \rangle$ in Fig. 3.9, where we have also shown the variation of the magnetization, M, with $\langle r_A \rangle$ at this temperature. Both M and M_r increase with $\langle r_A \rangle$, but their values become rather low when $\langle r_A \rangle \leq 1.18$ Å.

The electrical resistivities of the cobaltates show trends which are consistent with the magnetic properties. In Fig. 3.10 we show typical resistivity data for two series of cobaltates. The temperature coefficient of resistivity changes from a near-zero value to a negative value around x_c in some of the series, but in all the four series the magnitude of resistivity shows a marked increase around a critical composition x_c or a critical radius $\langle r_A^c \rangle$ of ~1.18 Å. We observed this behavior at x = 0.490 and 0.195 for the Nd and Dy series respectively (Fig. 3.10).

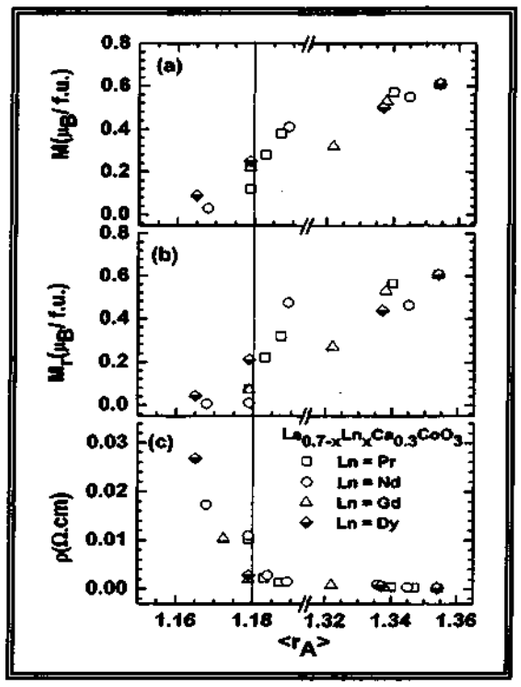

Figure 3.9 Variation of (a) the magnetic moment, μ_B, (b) remanent magnetization, M_r, and (c) the electrical resistivity in $La_{0.7-x}Ln_xCa_{0.3}CoO_3$ with $\langle r_A \rangle$ (Å) (50 K)

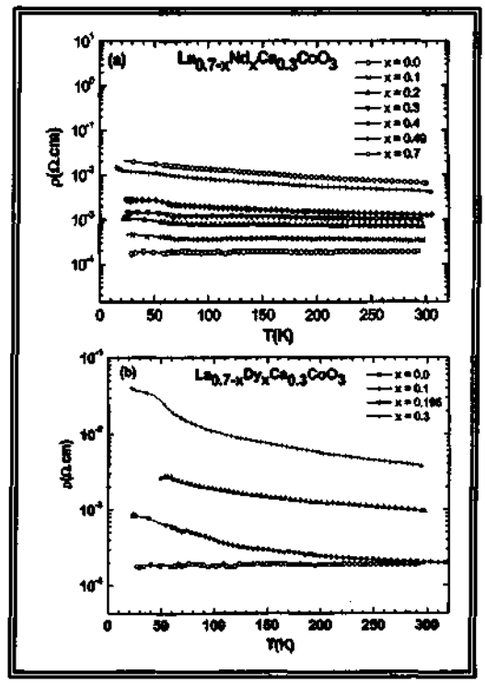

Figure 3.10 Temperature variation of the electrical resistivity of $La_{0.7-x}Ln_xCa_{0.3}CoO_3$ (Ln = Nd and Dy).

In order to rationalize the resistivity data in the four series of cobaltates, we have plotted the resistivity data at 50 K against $\langle r_A \rangle$ in Fig. 3.9 (c). There is a noticeable increase in the resistivity with decreasing $\langle r_A \rangle$, with a change in slope around 1.18 Å. It is to be noted that below this value of the A-site cation radius, electronic phase separation and charge-ordering occur in the rare earth manganates [13].

The $\langle r_A \rangle$ value of 1.18 Å in the cobaltates corresponds to $x \approx$ 0.6, 0.49, 0.24 and 0.195 respectively in the Pr, Nd, Gd and Dy substituted series of cobaltates and we denote these compositions as x_c. It appears that the small magnetic cluster regime becomes prominent around x_c or $\langle r_A^c \rangle$. The low-temperature peak in the ac-susceptibility data is frequency-dependent; the small magnetic cluster regime at small $\langle r_A \rangle$ in the $La_{0.7-x}Ln_xCa_{0.3}CoO_3$ system can be considered as the regime to be magnetically inhomogeneous. The inhomogeneous nature of the cobaltates prevails over the entire range of compositions (x = 0.0 – 0.7). It seems that around a composition close to x_c or $\langle r_A \rangle$, there is a marked change in the distribution of the magnetic species. Thus, when $x < x_c$ or $\langle r_A \rangle > \langle r_A^c \rangle$, relatively large ferromagnetic clusters or domains are present in the system, resulting in large magnetization and T_C values. When $x > x_c$ or $\langle r_A \rangle < \langle r_A^c \rangle$, the magnetic clusters become small in size. The ferromagnetic clusters being hole-rich, the electrical resistivity data show changes around the same compositions as the magnetization data, the compositions with $\langle r_A \rangle > \langle r_A^c \rangle$ exhibiting lower resistivities and near-zero temperature coefficients of resistivity. While one may treat the change in the nature of magnetic species around x_c or $\langle r_A^c \rangle$ as a mere change in size distribution, we consider it more appropriate to treat it as a case of phase separation since we observe more than one transition in the ac-susceptibility data and the resistivity changes parallel

the changes in the magnetic properties. The phase separated regime here involves the coexistence of large ferromagnetic clusters which are hole-rich and small clusters which are hole-poor.

It is instructive to examine the nature of the spin-states of cobalt in the $La_{0.7-x}Ln_xCa_{0.3}CoO_3$ system. We can estimate the magnetic moment of the cobalt ion from the inverse magnetic susceptibility data at high temperatures (180–300 K). The susceptibility value as well as the slope of the inverse susceptibility-temperature plot gives an average magnetic moment value of 4.5 μ_B per cobalt ion in all the series of cobaltates. This value suggests that in the 180 –300 K range, the cobalt ions are in the intermediate-spin (IS) and or high-spin (HS) states. The IS and HS states of Co^{3+} correspond to the electronic configurations $t_{2g}^5e_g^1$ (S = 1) and $t_{2g}^4e_g^2$ (S = 2) respectively, and those of Co^{4+} to $t_{2g}^4e_g^1$ (S = 3/2) and $t_{2g}^3e_g^2$ (S = 5/2). Investigations of the spin-state transitions in the cobaltates have shown that at high temperatures, the cobalt ions are mostly in the IS or the HS state [46]. At low temperatures, some of the cobalt ions may go to the low-spin (LS) state, corresponding to the t_{2g}^6 (S = 0) and t_{2g}^5 (S = 1/2) configurations in Co^{3+} and Co^{4+} ions respectively. The ferromagnetic clusters present prominently at $x < x_c$ or $\langle r_A \rangle > \langle r_A^c \rangle$ involve cobalt ions in the IS or HS states. The ferromagnetic regime will therefore be hole-rich, the size of the clusters or the domains decreasing with increasing x or decreasing $\langle r_A \rangle$. We would, therefore, expect a magnetic percolation threshold as well as electrical percolation in the system. We find that a plot of log ρ versus log $|\langle r_A \rangle - \langle r_A^c \rangle|$ is linear with a negative slope of around 0.5 at 50 K.

We have explored whether the resistivity behavior of $La_{0.7-x}Ln_xCa_{0.3}CoO_3$ conforms to activated hopping, defined by $\log \rho \propto (1/T^n)$ where n = 1, 2 or 4. Here, n = 1

corresponds to a simple Arrhenius behavior. When n = 2, the hopping is referred to as nearest-neighbor hopping (NNH), controlled by Coulombic forces. When n = 4, there would be variable range hopping (VRH) and the hopping dynamics is controlled by the collective excitation of the charge carriers [47].

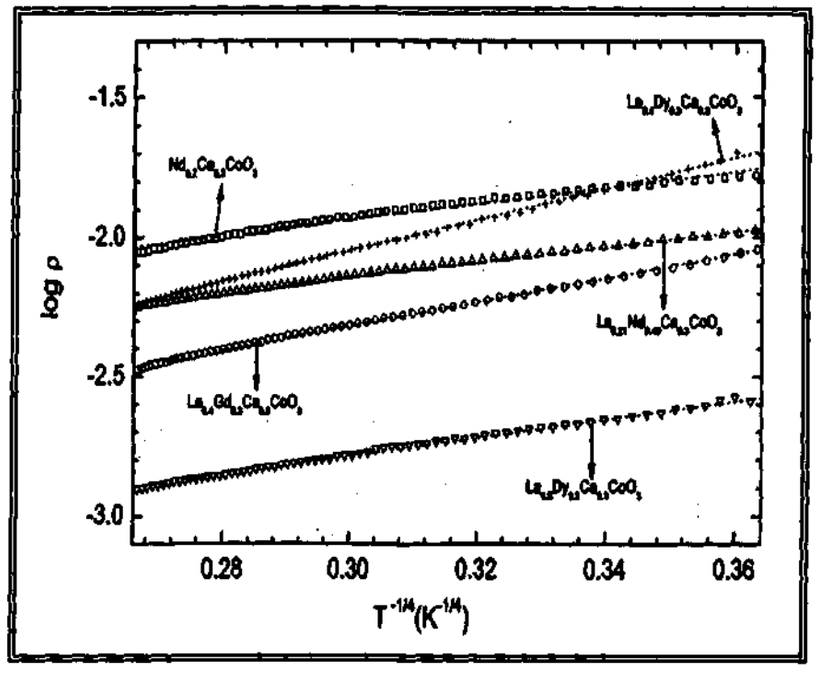

Figure 3.11 Fits of the resistivity data for $La_{0.7-x}Ln_xCa_{0.3}CoO_3$ for $x > x_c$ to the $T^{-1/4}$ law in the 49 – 200 K range. The symbols represent experimental data points and broken lines represent the linear fits.

The resistivity data in the 49 – 200 K range could be fitted to a $T^{-1/2}$ dependence with the standard deviation varying between 0.008 and 0.016. The standard deviation for the $T^{-1/4}$ fits is generally much smaller (0.005 – 0.012). In Fig. 3.11, we show typical fits to the $T^{-1/4}$ law. The occurrence of VRH in the cobaltates is consistent with the earlier studies of Rao et al [48] on the rare earth cobaltates.

Conclusions

Our investigations on the magnetic and electrical properties of polycrystalline $La_{0.7-x}Ln_xCa_{0.3}CoO_3$ (Ln = Pr, Nd, Gd and Dy) can be understood in terms of a phase separation scenario wherein large carrier-rich ferromagnetic clusters and carrier-poor smaller clusters coexist at some compositions. Accordingly, at large x, we observe two prominent magnetic transitions, the one at low temperatures being associated with the small clusters. Since the ferromagnetic clusters prominent at small x are hole-rich, we observe a change in the electrical resistivity behavior at a critical value x_c, where the size distribution of magnetic clusters undergoes significant changes. The critical value of x in the four series of cobaltates corresponds to the critical value of radius, $\langle r_A^c \rangle$, of 1.18 Å, a value where rare earth manganates of the type $La_{0.7-x}Ln_xCa_{0.3}MnO_3$ (Ln = Nd, Gd and Y) are known to exhibit charge ordering and phase separation prominently [13]. It appears that around $\langle r_A^c \rangle$ or x_c, a significant change occurs in the e_g band-width and the charge carriers become more localized, causing changes in the magnetic and electron transport properties. It is well to recall that the electrical resistivity and ferromagnetism in the cobaltates are linked to the presence of the Co^{3+}-O- Co^{4+} species with the appropriate spin states of cobalt ions.

$Ln_{0.7}Ca_{0.3}CoO_3$ (Ln = La, Pr and Nd)

Preliminary measurements (at 1 kOe) of the dc magnetic susceptibilities of polycrystalline samples $Ln_{0.7}Ca_{0.3}CoO_3$ with Ln = La, Pr and Nd showed that while $La_{0.7}Ca_{0.3}CoO_3$ clearly exhibits a ferromagnetic-type transition (T_C~175 K), $Pr_{0.7}Ca_{0.3}CoO_3$ and $Nd_{0.7}Ca_{0.3}CoO_3$ do not show distinct ferromagnetic transitions down to 50 K (Fig. 3.12(a)). There is a slight increase in the susceptibility of $Pr_{0.7}Ca_{0.3}CoO_3$

around 75 K, but this is not due to a genuine ferromagnetic transition. The magnetic behavior of a single crystal of $Pr_{0.7}Ca_{0.3}CoO_3$ is similar to that of the polycrystalline sample (see inset of Fig. 3.12(a)). On the basis of the $\langle r_A \rangle$ values, the ferromagnetic T_C's of $Pr_{0.7}Ca_{0.3}CoO_3$ and $Nd_{0.7}Ca_{0.3}CoO_3$ would be expected to be well above 100 K. Electrical resistivities of these cobaltates are also much higher (Fig. 3.12(b)). The large drop in the magnetic moment at low temperatures in the Pr and Nd derivatives is noteworthy. In order to understand the nature of these materials, we have investigated the magnetic properties of $Pr_{0.7}Ca_{0.3}CoO_3$ in detail, down to low temperatures.

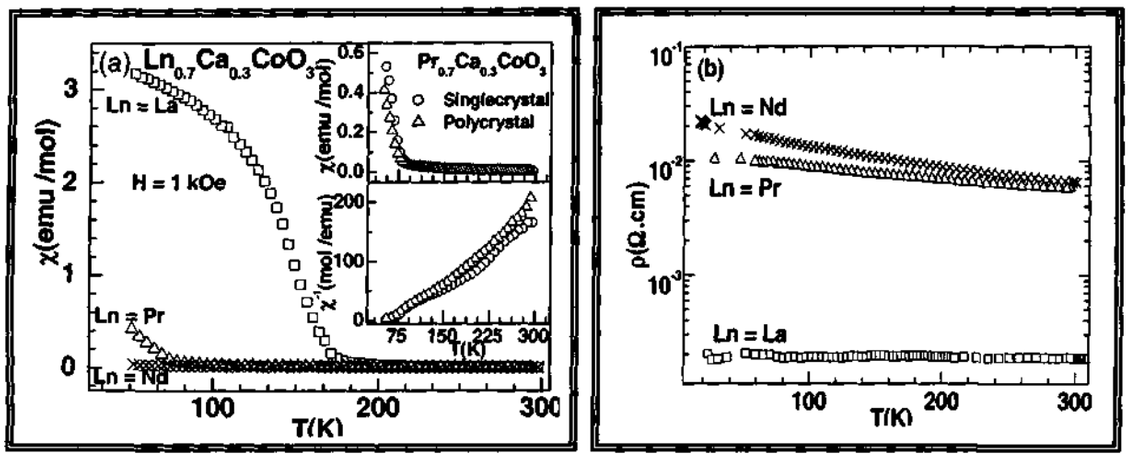

Figure 3.12 Temperature dependence of (a) the magnetic susceptibility (H = 1000 Oe) and (b) the electrical resistivity of $Ln_{0.7}Ca_{0.3}CoO_3$ (Ln = La, Pr and Nd). The inset in (a) shows the magnetic susceptibility and inverse magnetic susceptibility of $Pr_{0.7}Ca_{0.3}CoO_3$ for single crystal and polycrystalline samples.

In Fig. 3.13 we show the temperature dependence of the dc magnetic susceptibility of $Pr_{0.7}Ca_{0.3}CoO_3$ in the ZFC and FC conditions (H = 100 Oe). There is considerable divergence in the ZFC and FC magnetization behavior just as in magnetically frustrated systems [14].

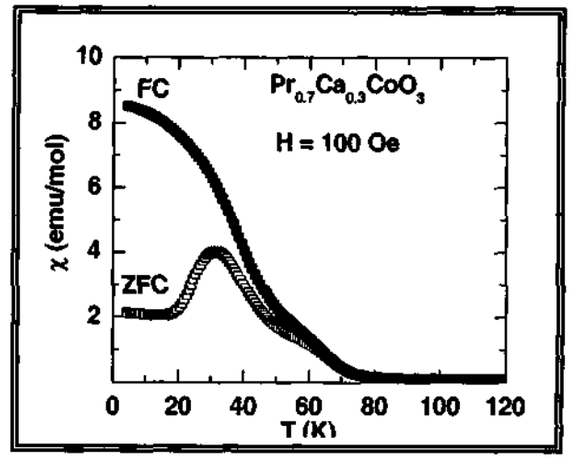

Figure 3.13 Temperature dependence of magnetic susceptibility of $Pr_{0.7}Ca_{0.3}CoO_3$ (H = 100 Oe).

The data show two broad transitions around 60 K and 30 K. Measurements carried out at 5 kOe, however, do not reveal the two peaks (Fig 3.14), suggesting that the intermediate temperature range M-H behavior of this material is rather complex at low fields. The data in Fig. 3.14 suggest that magnetic ordering sets in around 75 K with the susceptibility going through a broad maximum around 15 K. Inverse magnetic susceptibility data, as-

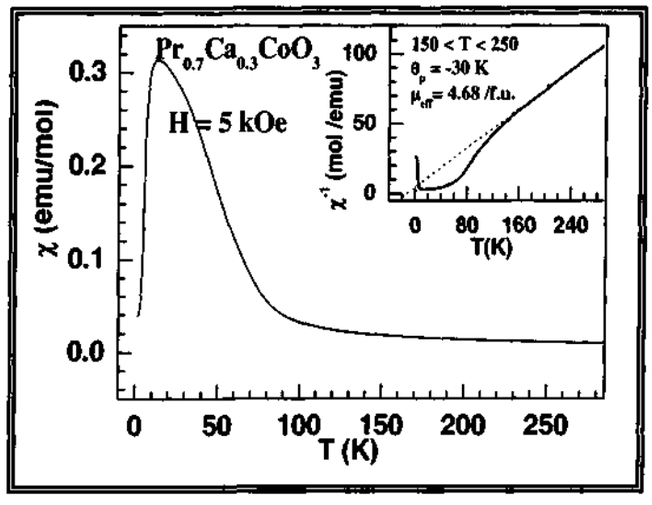

Figure 3.14 Temperature dependence of magnetic susceptibility of $Pr_{0.7}Ca_{0.3}CoO_3$. Inset shows the inverse magnetic susceptibility (H = 5 kOe).

shown in the inset of Fig. 3.14, yield a Curie temperature (θ_p) of - 30 K. The high temperature linear region of the inverse susceptibility data gives a magnetic moment of 4.7 μ_B/f.u. The shape of $\chi - T$ plot below 75 K is rather complex, not typical of normal ferromanets. It appears as though there is a spread of magnetic transition temperatures due to local environmental effects.

In Fig. 3.15, we show the M – H behavior of $Pr_{0.7}Ca_{0.3}CoO_3$. The behavior is rather complex especially in the temperature range of 25 – 60 K. The plots remain nonlinear upto 120 kOe even at 5 K. The behavior is unlike of ferromagnets and is somewhat comparable to that of frustrated systems. Extrapolation of the M – H data in the high field region to zero fields gives a saturation moment of around 0.4 μ_B/f.u.

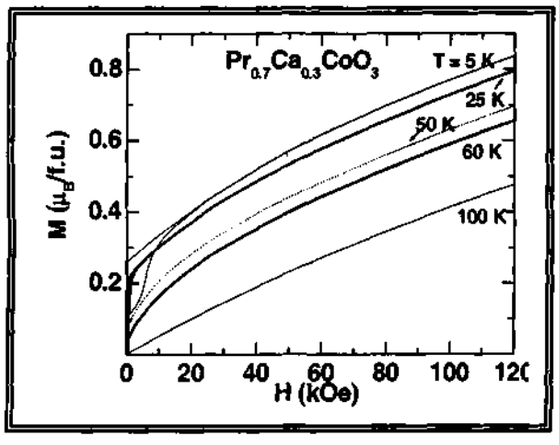

Figure 3.15 High field magnetization curve of $Pr_{0.7}Ca_{0.3}CoO_3$ at low temperatures.

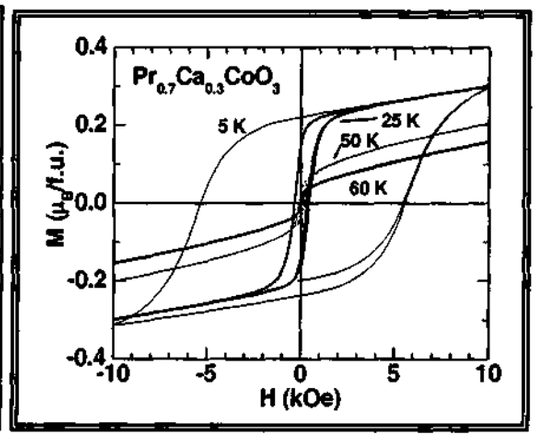

Figure 3.16 Low field magnetic hysteresis of $Pr_{0.7}Ca_{0.3}CoO_3$ at low temperatures.

The small value of the moment on cobalt in the apparently ferromagnetic state, compared with the value in the paramagnetic state, indicates itinerant ferromagnetism, which is possible because the material is conducting. From Fig. 3.16 we see that there is

hysteresis at 5 K even at low fields, suggesting a ferromagnet-like behavior. The width of the hysteresis loop decreases markedly with increasing temperature. The above results reveal that ferromagnetic and antiferromagnetic interactions coexist at low temperatures, with the small conducting ferromagnetic domains or clusters giving rise to a small magnetic moment.

The ac susceptibility measurements on the polycrystalline samples (Fig. 3.17) show that the low-temperature transition has a frequency dependence of about 1.3 K, as the frequency is increased from 1.3 to 1330 Hz. The 60 K peak, however, shows little shift (Fig. 3.17). The position of the low temperature peak in the ac susceptibility data at 1.3 Hz, for which the field of measurement is 1 Oe, occurs at 37.4 K, and shifts to lower temperatures at higher fields.

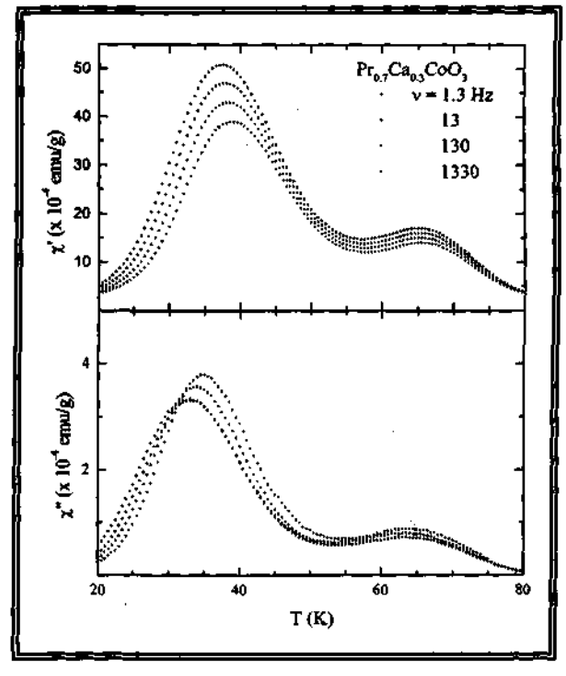

Figure 3.17 Temperature dependence ac-susceptibility data of $Pr_{0.7}Ca_{0.3}CoO_3$ at different frequencies.

Thus, for H = 100 and 5000 Oe, the peak occurs at 31.5 and 12.7 K respectively. Because of the inhomogeneous nature, it is difficult to clearly assign one temperature for the bulk

transition in this cobaltate, although the first transition clearly occurs around 60 K. We, therefore, conclude that the behavior of $Pr_{0.7}Ca_{0.3}CoO_3$ represents a special case of electronic phase separation.

We have carried out studies on polycrystalline $Nd_{0.7}Ca_{0.3}CoO_3$ as well. This sample also shows divergence in the ZFC and FC behavior at H = 100 Oe (Fig. 3.18), but the divergence is not marked as much as in $Pr_{0.7}Ca_{0.3}CoO_3$. The ZFC data seems to suggest two close transitions between 0 and 20 K. The dc susceptibility data at high fields (H = 5 kOe) shows one distinct transition around 20 K (Fig. 3.19). The inverse magnetic susceptibility data yield a θ_p value – 170 K. The M – H behavior of this cobaltate is also nonlinear just as $Pr_{0.7}Ca_{0.3}CoO_3$. The material shows narrow hysteresis below 5 K, at high fields (see inset Fig. 3.19).

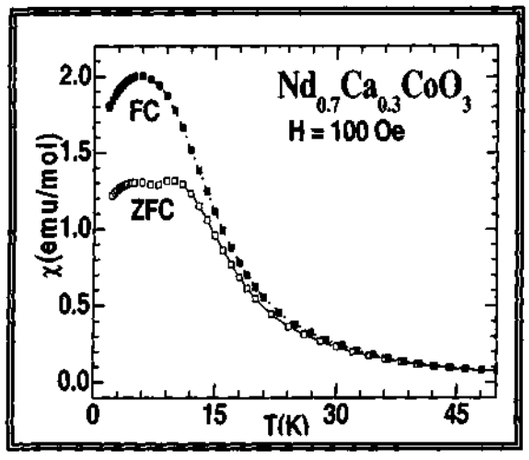

Figure 3.18 Temperature dependence of the magnetic susceptibility, χ, of $Nd_{0.7}Ca_{0.3}CoO_{2.95}$ (H = 100 Oe).

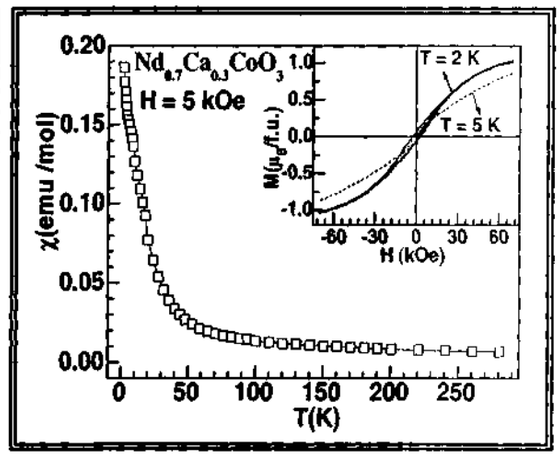

Figure 3.19 Temperature dependence of magnetic susceptibility, χ, of $Nd_{0.7}Ca_{0.3}CoO_{2.95}$ (H = 5000 Oe). Inset shows low temperatures hysteresis.

The electronic phase separation and associated magnetic properties of $Pr_{0.7}Ca_{0.3}CoO_3$ and $Nd_{0.7}Ca_{0.3}CoO_3$ arise because of the small average size of the A-site

cations. In these two cobaltates, the average radius (for orthorhombic structure) is less than 1.18 Å, which is the critical value only above which long-range ferromagnetism manifests itself [13]. It is known that increase in size disorder and decrease in size of the A-site cations favor phase separation.

Conclusions

$Pr_{0.7}Ca_{0.3}CoO_3$ does not show a sharp ferromagnetic type transition down to 50 K. There is large divergence between the dc magnetic susceptibility of the ZFC and FC sample. The magnetization is nonlinear with field. The ac susceptibility data show evidences for a magnetic transition around 60 K and a frequency-dependent transition at low temperatures. Properties of $Nd_{0.7}Ca_{0.3}CoO_3$ are not unlike those of the Pr analogue. These various features indicate that these cobaltates are magnetically inhomogeneous, with small ferromagnetic clusters or domains being present in an antiferromagnetic matrix.

3.4.2 Non-equilibrium magnetic properties of single crystalline[‡] rare earth cobaltates, $Ln_{0.7}Ca_{0.3}CoO_3$ (Ln = La, Pr and Nd)

$La_{0.7}Ca_{0.3}CoO_3$: The temperature dependence of the ZFC and FC magnetization of single-crystalline $La_{0.7}Ca_{0.3}CoO_3$ measured parallel to the c-axis of the sample at different

---

[‡]Investigations on poly- and single crystalline samples were carried out to examine the effect of magnetic and electron transport properties. It is assumed that a single crystal is monophasic with exact composition and with a well defined set of properties. These properties are strongly direction dependent. In our present investigations we have noticed some interesting features in single crystalline form, which were absent in polycrystalline samples may be due to grain size and/or grain boundary effects.

applied fields (10, 20, 100 and 1000 Oe) is shown in Fig. 3.20. A sharp increase of the magnetization occurs in the low-field FC data around 170 K indicating that the system orders and attains a spontaneous magnetization. A characteristic strong irreversibility between the low field ZFC and FC magnetization curves appears just below the transition temperature.

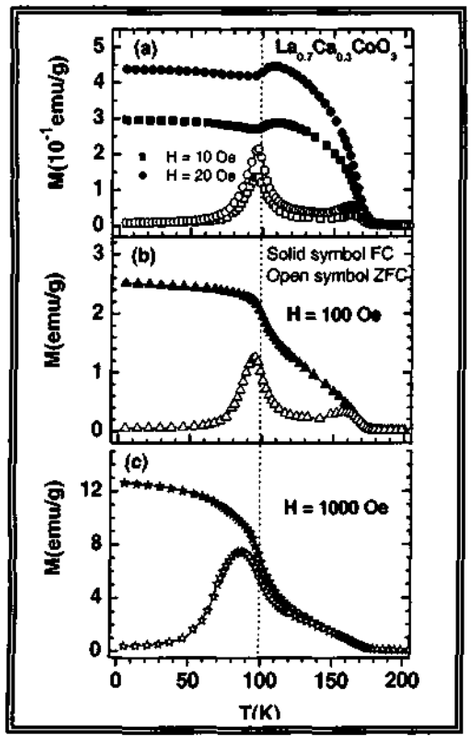

Figure 3.20 Temperature dependence of the ZFC and FC magnetization of $La_{0.7}Ca_{0.3}CoO_3$ at different applied fields (a) H = 10, 20 Oe (b) H = 100 Oe and (c) H = 1000 Oe. (Left)

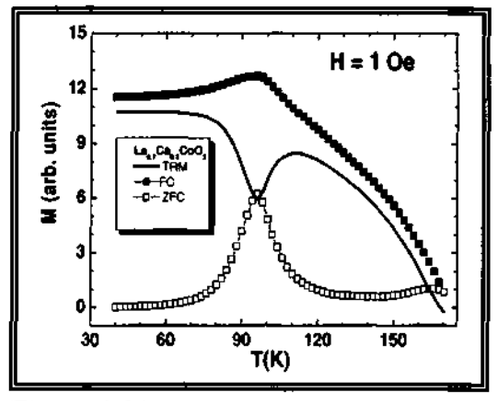

Figure 3.21 Temperature dependence of TRM, FC and ZFC magnetization recorded for $La_{0.7}Ca_{0.3}CoO_3$ at H = 1 Oe.

The ZFC data show a small peak close to 170 K and a second anomaly around 100 K as a relatively sharp maximum, accompanied by a change in the slope of the FC magnetization curve, indicating a transition in the ordered spin structure. Fig. 3.21 shows the ZFC, FC and thermo remnant magnetization (TRM) curves of $La_{0.7}Ca_{0.3}CoO_3$ measured in a weak field of 1 Oe. The transition at 100 K appears as a sharp dip in the TRM and a sharp maximum in the ZFC magnetization.

Some of the details of the temperature dependence of $M_{ZFC}(T)$ in Fig. 3.20 are noteworthy. With increasing field (H = 100 Oe), both the peaks in the ZFC data shift towards lower temperatures. Furthermore, on increasing the field up to 1000 Oe, the high temperature $M_{ZFC}(T)$ peak disappears, showing only a shoulder in this temperature region; the 100 K peak becomes broader at higher fields. Another interesting feature is that the irreversibility temperature, T_{irr}, (where FC and ZFC curves diverge) decreases with the increasing field, T_C being equal to T_{irr} at sufficiently low fields (10 and 20 Oe), however for higher fields $T_{irr} < T_C$. When the applied field is increased, the $M_{FC}(T)$ and $M_{ZFC}(T)$ curves merge down to ~ 100 K (T_f), a behavior akin to that of ordinary spin-glasses [49].

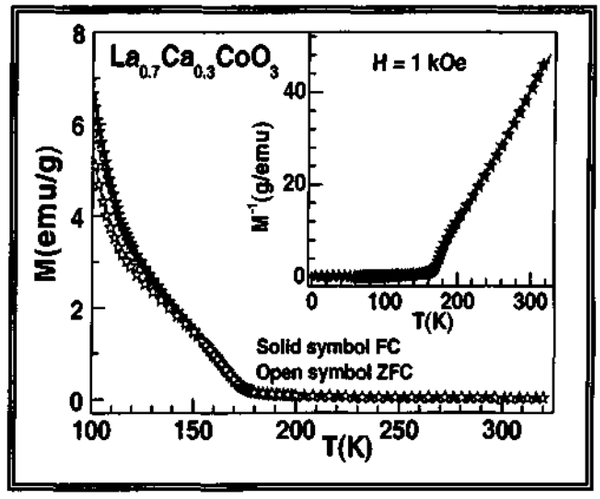

Figure 3.22 Temperature dependence of the ZFC and FC magnetization of $La_{0.7}Ca_{0.3}CoO_3$. The inset shows the temperature dependence of inverse magnetization, M^{-1}, (H = 1000 Oe).

In Fig. 3.22, the magnetization data of $La_{0.7}Ca_{0.3}CoO_3$ at 1000 Oe are plotted in the temperature range of 100-320 K along with the high-temperature inverse magnetization data (see inset). The sample shows Curie-Weiss behavior in the 200-300 K range and a fit to the Curie-Weiss law yields a ferromagnetic Weiss temperature, θ_p, of 150 K and a p_{eff} of ~ 1.6 μ_B/Co-ion, implying S ~ 0.6 μ_B. The derived Weiss-temperature is lower than the ferromagnetic transition temperature (170 K), defined from the

inflection point of the inverse magnetization vs. temperature curves. The anomaly occurring around 100 K can be considered to represent a re-entrant spin-glass transition, similar to that found in $Y_{0.7}Ca_{0.3}MnO_3$ by Mathieu et al [50].

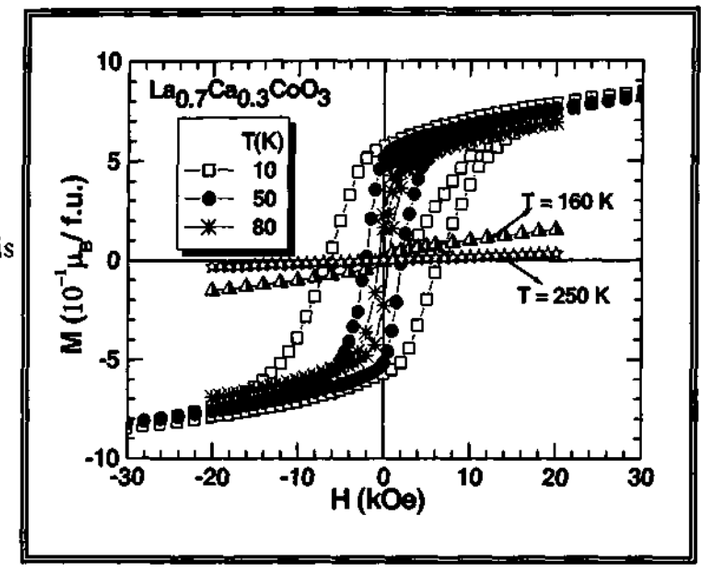

Figure 3.23 Typical hysteresis curves for $La_{0.7}Ca_{0.3}CoO_3$ at different temperatures.

In Fig. 3.23, we show M-H loops measured parallel to the c-axis of $La_{0.7}Ca_{0.3}CoO_3$ sample at different temperatures. A large hysteresis loop develops below the transition temperature at 170 K and attains a remanence value of ~ 0.6 μ_B/Co-ion and a coercive force of ~ 0.6 Tesla (T) at the lowest temperature. The material becomes harder with decreasing temperature, with the coercive field increasing monotonically with decreasing temperature from 0.02 T at 160 K (near T_C) to 0.6 T at 10 K. At temperatures higher than T_C (T = 250 K), the M-H behavior is linear corresponding to a paramagnetic state.

Figure 3.24 presents the $M_{FC}(T)$, $M_{ZFC}(T)$ and M-H behavior for two different orientations of $La_{0.7}Ca_{0.3}CoO_3$ crystal (H $\parallel$ c-axis and H $\perp$ c-axis). The magnitudes of

$M_{FC}(T)$ and $M_{ZFC}(T)$ are both higher in the perpendicular direction. Whereas the shape of $M_{ZFC}(T)$ curve remains similar, the shape of $M_{FC}(T)$ changes considerably depending on the direction. In spite of the large c-axis dependence of the initial low-field behavior, the high field part of the M-H curves is almost independent of field direction as can be seen from Fig. 3.24 (b). The coercive field and remanent magnetization are almost the same for both the orientations; the magnetic moment at 5 T is the same (~ 0.9 μ_B/Co-ion).

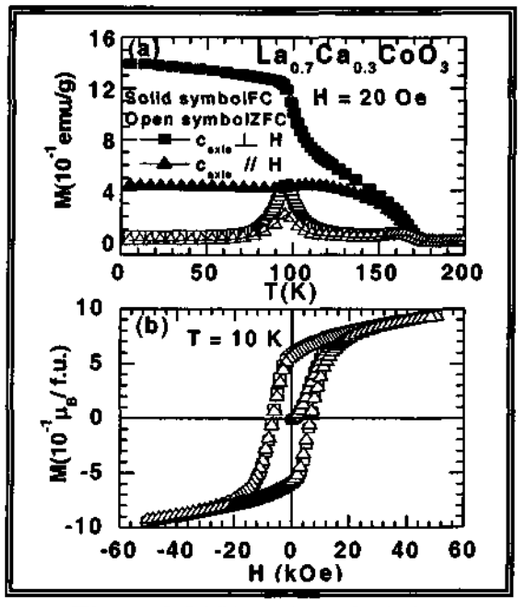

Figure 3.24 Variation of (a) the ZFC and FC magnetization and (b) magnetic hysteresis curves of $La_{0.7}Ca_{0.3}CoO_3$ for different field directions.

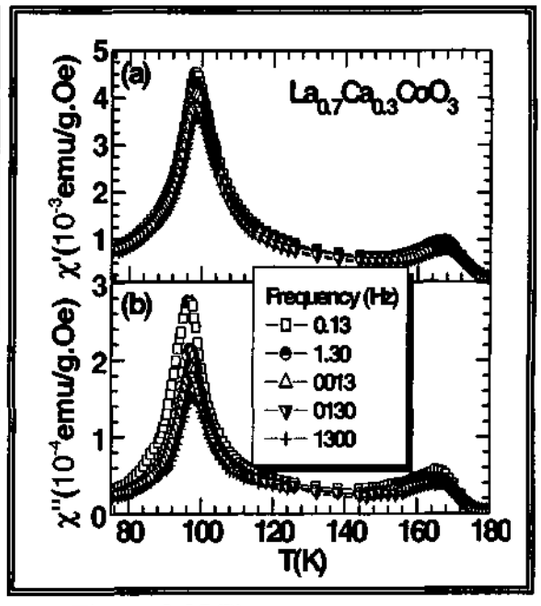

Figure 3.25 The temperature dependence of the (a) In-phase and (b) Out-of-phase ac-susceptibility of $La_{0.7}Ca_{0.3}CoO_3$ at different frequencies.

Figure 3.25 shows the in-phase $\chi'(T)$ and out-of-phase $\chi''(T)$ components of the ac-susceptibility of $La_{0.7}Ca_{0.3}CoO_3$ below Curie temperature (T_C). A rather similar behavior has also been reported in some manganate systems by Nam et al [51]. The in-phase component shows, in accordance with the low field ZFC magnetization, two distinct peaks: a frequency-independent high temperature peak at about 170 K that

indicates a ferromagnetic ordering and a lower temperature at 100 K peak that is sharper and frequency-dependent. The frequency-dependence of the ac-susceptibility near and below the 100 K anomaly is stronger than at higher temperatures.

In order to explore whether the system is in a thermodynamic equilibrium state or in a non-equilibrium spin-glass like state, the relaxation of the ZFC magnetization of $La_{0.7}Ca_{0.3}CoO_3$ was measured at 40, 85 and 110 K after different wait times. The long-time relaxations of the magnetization and aging phenomena well known in spin-glasses [52] are commonly found in many other random magnetic systems. In Figs. 3.26, 3.27 and 3.28 we present the results of $M_{ZFC}(T,t_w,t)$ and S(t) for T_m = 40, 85 and 110 K, respectively. It should be mentioned that all the magnetization relaxation curves are measured relative to the first measured data point at $t \approx 0.3$ s, which is set close to zero by a reset of the SQUID electronics.

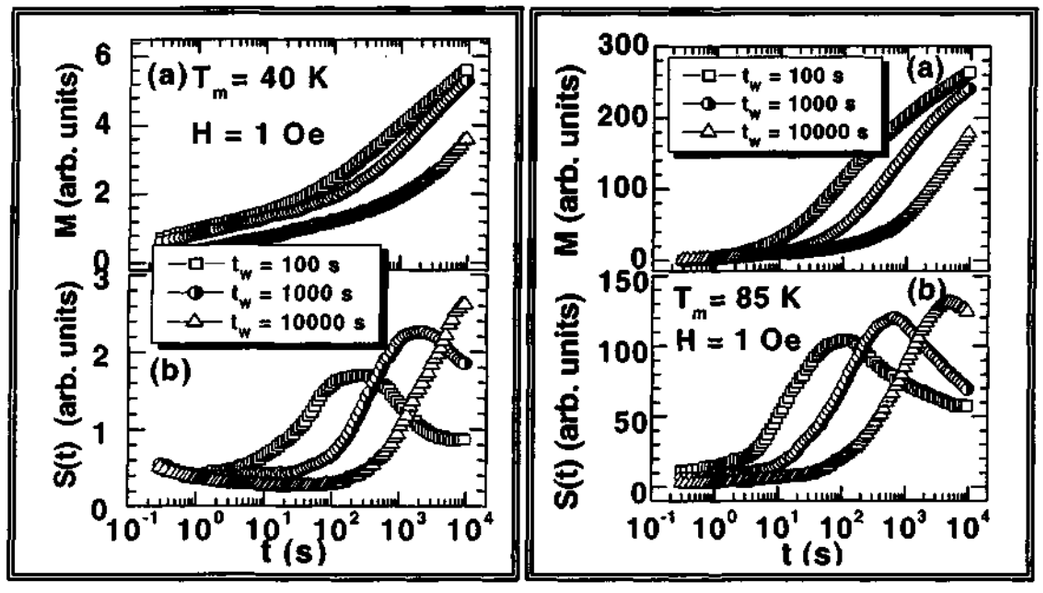

Figures 3.26 (left) and 3.27 (right): ZFC-relaxation measurements on $La_{0.7}Ca_{0.3}CoO_3$ at T_m = 40 K (left) and T_m = 85 K (right) for different waiting times, t_w = 100, 1000 and 10000s (H = 1 Oe).

The relaxation rate S(t) is defined by, $S(t) = 1/H\ [dM_{ZFC}(T,t_w,t)/dlog(t)]$, and emphasizes the aging features of the relaxation curves. In all the ZFC-relaxation measurements the applied field was 1 Oe and the wait times chosen were t_w = 100, 1000 and 10000 s. The $M_{ZFC}(T,t_w,t)$ measurements show that the sample exhibits logarithmically slow dynamics and an aging effect at all temperatures below T_C. The aging phenomenon is revealed from the difference between the $M_{ZFC}(T,t_w,t)$ curves with different t_w.

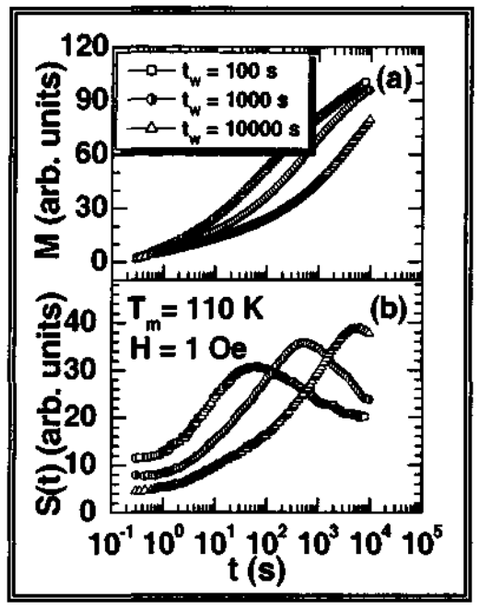

Figure 3.28 ZFC-relaxation measurements on $La_{0.7}Ca_{0.3}CoO_3$ at T_m = 110 K for different waiting times, t_w = 100, 1000 and 10000s (H = 1 Oe).

We notice a striking aging behavior, similar to that of spin-glasses at all three temperatures as revealed by an inflection point in the magnetization vs log (t) curves and a corresponding maximum in the relaxation rate curves at an observation time close to the wait time. The relaxation at 40 K is almost two orders of magnitude weaker than the relaxation at the two higher temperatures. In spite of this, the aging character dominates

the measured relaxation at all three temperatures. The relaxation of the magnetization measured within our experimental time window (0.3 – 10 000 s) corresponds to a fraction of the total relaxation, and the equilibrium magnetization is far from being reached within this time window. The aging-dominated relaxation observed here is strikingly similar to the behavior of conventional spin-glasses. In the latter situation, aging is interpreted within the droplet model (or domain growth) model for spin-glasses [53] to reflect the growth of equilibrium spin-glass domains, with the maximum in the relaxation rate being associated with a cross over between quasi-equilibrium (from processes within ordered spin-glass domains) and non-equilibrium dynamics (processes governed by effects at domain walls).

A key property to understand and model the dynamics of spin-glasses is the occurrence of memory. The memory phenomenon is observed in zero-field-cooled magnetization vs. temperature experiments as follows [54]. First a reference experiment is made, according to the ZFC protocol described earlier. A memory curve is then recorded, with the additional feature that the cooling of the sample is halted at a stop temperature for some hours during which the sample ages. This slows down the dynamics of the sample in a region around the stop temperature, which in turn causes a dip in the $M_{ZFC}(T)$ curve. To clearly illustrate memory, it is convenient to plot the difference between the reference and the memory curve. A characteristic of the spin-glass phase (ordinary or re-entrant) is the memory behavior, whereas a disordered and frustrated ferromagnetic phase would show little or no memory effect. We carried out three experiments, one with a halt below 100 K (85 K), the second with the halt above 100 K (110 K) and the third with halts at both 85 K and 110 K. In Fig. 3.29 (a), we show the

reference curve and the two memory curves for $La_{0.7}Ca_{0.3}CoO_3$ crystal. Fig. 3.29 (b) shows the difference plots. At 85 K, a clear memory dip is observed indicating that the system is in a spin-glass type phase. At 110 K, on the other hand, a memory dip can barely be discerned, indicating that the system is confined in a disordered ferromagnetic phase.

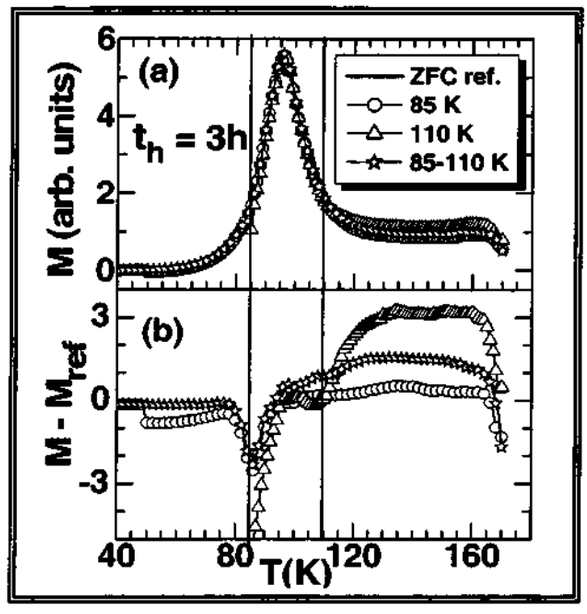

Figure 3.29 ZFC magnetization memory experiment on $La_{0.7}Ca_{0.3}CoO_3$; (a) the temperature dependence of ZFC magnetization, M, (reference curve) and on imprinting memories of two temperature stops (at 85 and 110 K) during cooling each for 3 hours and (b) the difference ($M-M_{ref}$) plot of the respective curves.

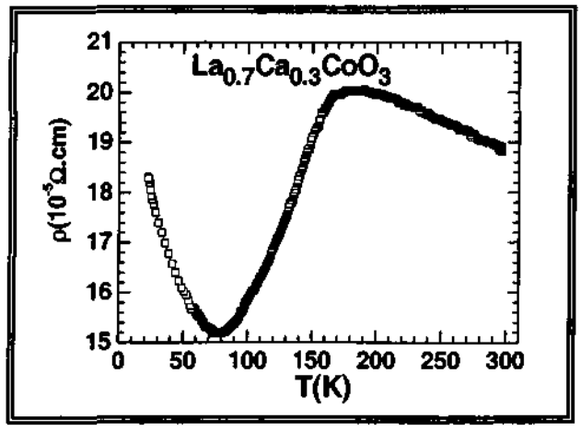

Figure 3.30 Temperature dependence of electrical resistivity, ρ, of $La_{0.7}Ca_{0.3}CoO_3$

The temperature dependence of electrical resistivity (ρ) of $La_{0.7}Ca_{0.3}CoO_3$ single crystal is shown in Fig. 3.30. With decreasing temperature there is not much variation in the- magnitude of resistivity, but the temperature coefficient of resistivity (dρ/dT) changes rapidly from room temperature to low temperatures. There is a change in slope around 170 K, above which dρ/dT becomes negative. Below this temperature, dρ/dT is positive indicating metallicity below T_c. Further decreasing the temperature, changes the slope from a positive to a negative value around 80 K, corresponding to an insulating behavior. In the 20 - 80 K range, the temperature variation of resistivity appears to conform to the variable range hopping regime [47] in accord with the results on polycrystalline samples discussed earlier.

Conclusions

Our investigation on single crystals of $La_{0.7}Ca_{0.3}CoO_3$ is that the system enters a non-equilibrium magnetic phase at temperatures below an apparent ferromagnetic transition at 170 K. The non-equilibrium ferromagnetic phase experiences an additional transition into a non-equilibrium re-entrant spin-glass phase at 100 K. The system appears to be phase separated into large carrier-rich ferromagnetic clusters (involves Co in the intermediate-spin (IS) and high-spin (HS) states) and carrier-poor antiferromagnetic or non-ferromagnetic matrix. The M(H) measurements also support this model. The hysteresis curve does not saturate even at higher field 5 T and lowest temperature (10 K). The absence of saturation even at higher fields is a characteristic feature of spin-glass system [49]. Considering the above magnetic behavior in the low temperature region; we propose that the system goes to re-entrant spin-glass state below 100 K. The magnetic moment of 1.6 μ_B/Co-ion, found by us is related to the percentage

of Co^{4+} in the system. While the Co^{3+} / Co^{4+} ratio is constant through out, the spin-state equilibrium varies with temperature. At low temperatures, both the cobalt ions would be in the low-spin (LS) state, but at higher temperatures the cobalt ions are mostly in the IS and HS states [46]. The value of p_{eff} obtained by us corresponds to a situation where both the Co^{3+} and Co^{4+} ions are in IS and or HS states. The positive θ_p value can be interpreted in terms of the short-range ferromagnetic interaction between Co^{3+} and Co^{4+} ions, which dominates over the super-exchange interactions between Co^{4+} - Co^{4+} and Co^{3+} - Co^{3+} ions.

$Pr_{0.7}Ca_{0.3}CoO_3$ and $Nd_{0.7}Ca_{0.3}CoO_3$:

Figure 3.31 shows temperature dependence of the ZFC and FC magnetization of single crystalline $Ln_{0.7}Ca_{0.3}CoO_3$ (Ln = La, Pr or Nd) measured parallel and perpendicular to the c-axis in an applied field of 20 Oe.

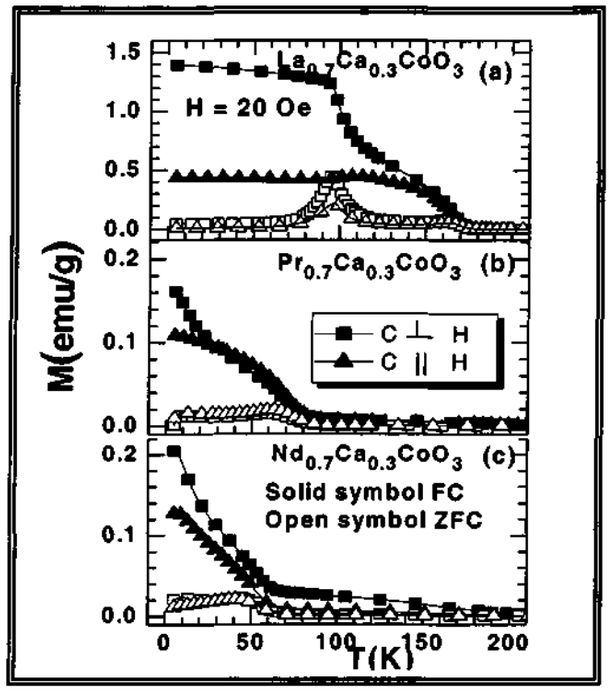

Figure 3.31 Temperature dependence of the ZFC and FC magnetization, M, of $Ln_{0.7}Ca_{0.3}CoO_3$ where (a) Ln = La (b) Ln = Pr and (c) Ln = Nd, at H = 20 Oe measured parallel (triangle) and perpendicular (square) to the c-axis.

The magnitudes of both $M_{FC}(T)$ and $M_{ZFC}(T)$ are higher in the perpendicular direction, the behavior remaining similar down to low temperatures. $La_{0.7}Ca_{0.3}CoO_3$ shows a distinct FM type transition in the FC data around 170 K (T_C) as expected, while the ZFC data show a cluster-glass transition around 95 K discussed in previous section. $Pr_{0.7}Ca_{0.3}CoO_3$ and $Nd_{0.7}Ca_{0.3}CoO_3$ do not, however, show such a ferromagnet type behavior down to low temperatures. On the other hand, they only show a slight increase in magnetization with decreasing temperature around 70 K, but the magnetization reaches values much lower than the theoretical saturation values even at 5 K. The irreversible temperature, T_{irr}, between the ZFC and FC data in $Pr_{0.7}Ca_{0.3}CoO_3$ and $Nd_{0.7}Ca_{0.3}CoO_3$ persists up to 200 K unlike in the La derivative where they merge around T_C. The T_{irr}, however, decreases with the increasing magnetic field. The TRM changes with temperature in a manner similar to the difference between the FC and ZFC magnetization. Inverse magnetic susceptibility data of the cobaltates provide supporting information. The data could be fitted to Curie-Weiss behavior with the extrapolated Weiss temperatures, θ_p, of 150 K, -180 K and -340 K for the La, Pr and Nd-derivatives respectively. The negative θ_p values in the latter two cobaltates imply the presence of antiferromagnetic interactions in the high temperature region, while for La-derivative the interaction is FM.

Fig. 3.32 shows M-H data of $Pr_{0.7}Ca_{0.3}CoO_3$ and $Nd_{0.7}Ca_{0.3}CoO_3$ at different temperatures, measured parallel to the c-axis of the samples. These cobaltates show hysteresis loops at low temperatures ($\leq$ 10 K) and a non-saturating behavior up to 5 Tesla (T). The values of the remanence magnetization and coercive field for the Pr compound at 10 K are $0.03\mu_B$/f.u. and 0.15T respectively while those for the Nd derivative are

$0.01\mu_B$/f.u. and 0.12T. The remanence magnetization and coercive field for $La_{0.7}Ca_{0.3}CoO_3$ at 10 K are $0.1\mu_B$/f.u. and 0.6T respectively. In spite of the c-axis dependence of the low-field behavior, the high-field parts of the M-H curves are nearly independent of the field direction. The coercive field and remanent magnetization are almost the same in both the orientations. With increasing temperature, the width of the hysteresis loop decreases rapidly and finally the M-H behavior becomes linear at higher temperatures (see the 100 K curves in Fig. 3.32).

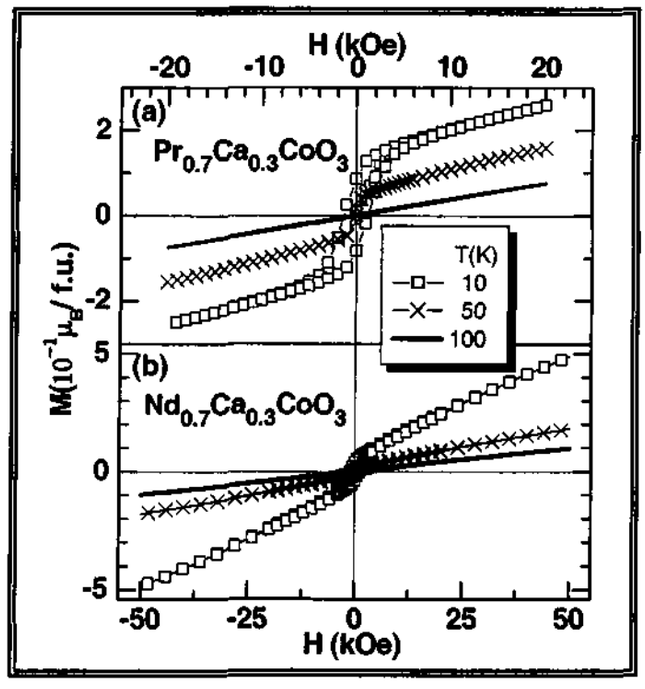

Figure 3.32 The hysteresis curves for (a) $Pr_{0.7}Ca_{0.3}CoO_3$ (b) $Nd_{0.7}Ca_{0.3}CoO_3$ at different temperatures measured parallel to the c-axis.

In order to further characterize the magnetic behavior of $Pr_{0.7}Ca_{0.3}CoO_3$ and $Nd_{0.7}Ca_{0.3}CoO_3$, we have carried out ac susceptibility and magnetic relaxation measurements which are useful to investigate the magnetic glassy behavior [49, 52].

Figure 3.33 shows the temperature dependence of the in-phase ZFC magnetization, $\chi'(T)$ and the out-of-phase $\chi''(T)$ components of the ac-susceptibility for $Pr_{0.7}Ca_{0.3}CoO_3$ and $Nd_{0.7}Ca_{0.3}CoO_3$. Both the systems show frequency-dependence below 80 K, down to low temperatures. A frequency-dependent maximum is observed around 70 K for $Pr_{0.7}Ca_{0.3}CoO_3$ in the in-phase as well as the out-of-phase components as can seen in Figs 3.33 (a) and (b). With increasing frequency, the peak value shifts toward higher temperatures. $Nd_{0.7}Ca_{0.3}CoO_3$ shows a peak around 55 K as shown in Figs. 3.33 (c) and (d). Thus, with decrease in the average radius of the A-site cations, $\langle r_A \rangle$, the magnetic transition temperature as revealed by the ac susceptibility maximum shifts to lower temperatures.

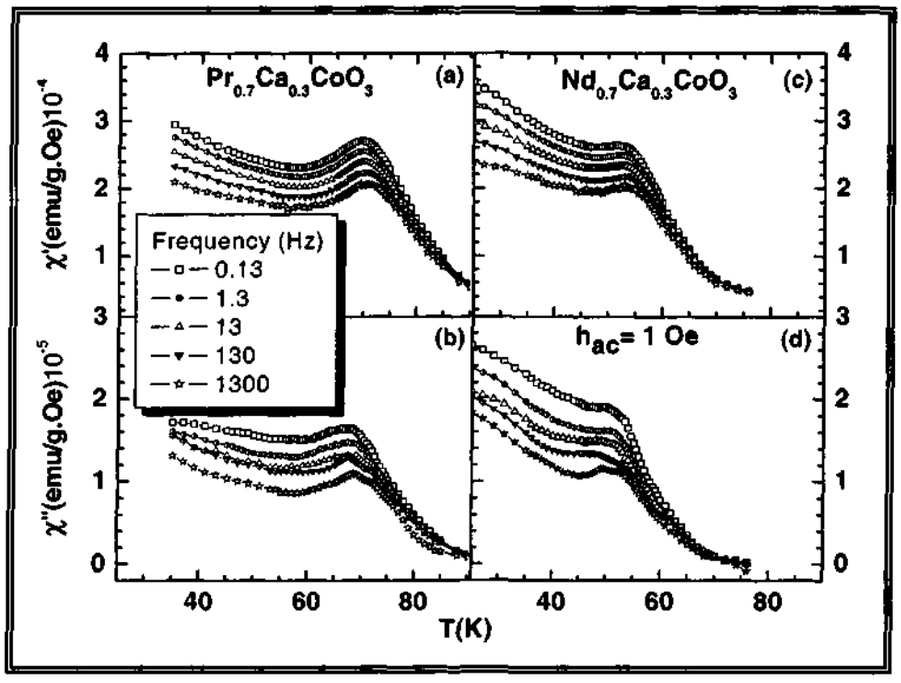

Figure 3.33 The temperature dependence of the In-phase and Out-of-phase ac-susceptibility for (a, b) $Pr_{0.7}Ca_{0.3}CoO_3$ and (c, d) $Nd_{0.7}Ca_{0.3}CoO_3$ at different frequencies (c-axis $\parallel h_{ac}$).

From the time-dependent ZFC magnetization measurements, we find that both $Pr_{0.7}Ca_{0.3}CoO_3$ and $Nd_{0.7}Ca_{0.3}CoO_3$ exhibit logarithmical dynamics below the transition temperature (70 and 55 K). Figs. 3.34 (a) and (b) present the time-dependent relaxation of the ZFC magnetization for $Pr_{0.7}Ca_{0.3}CoO_3$, measured at 50 K (T_m) and the corresponding relaxation rates $S(t) = 1/H\ [dM_{ZFC}(T,t_w,t)/d\log_{10}(t)]$. In all ZFC-relaxation measurements, the applied field was 1 Oe and the wait times were 100, 1000 and 10000 s.

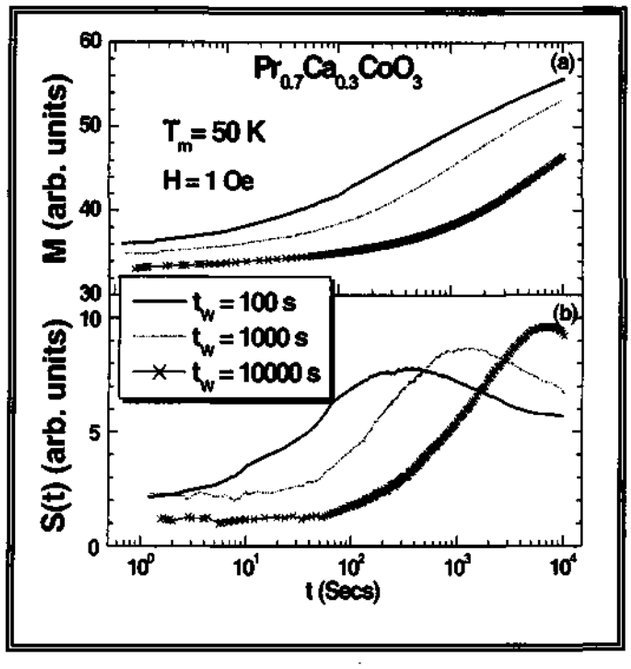

Figure 3.34 ZFC-relaxation measurements on $Pr_{0.7}Ca_{0.3}CoO_3$ at T_m = 50 K for different waiting times, t_w = 100, 1000 and 10000s (c-axis parallel to the field, H = 1 Oe).

Results of similar measurements on $Nd_{0.7}Ca_{0.3}CoO_3$ at 40 K are presented in Figs. 3.35 (a) and (b). The relaxation rate attains a maximum at the elapsed time, close to the wait time, indicating a pronounced age-dependent effect. Such a behavior is generally observed in spin-glasses [49]. Such an effect is explained within the droplet (or domain

growth) model, by associating the maximum in the relaxation rate with a crossover between quasi-equilibrium and non-equilibrium dynamics [54].

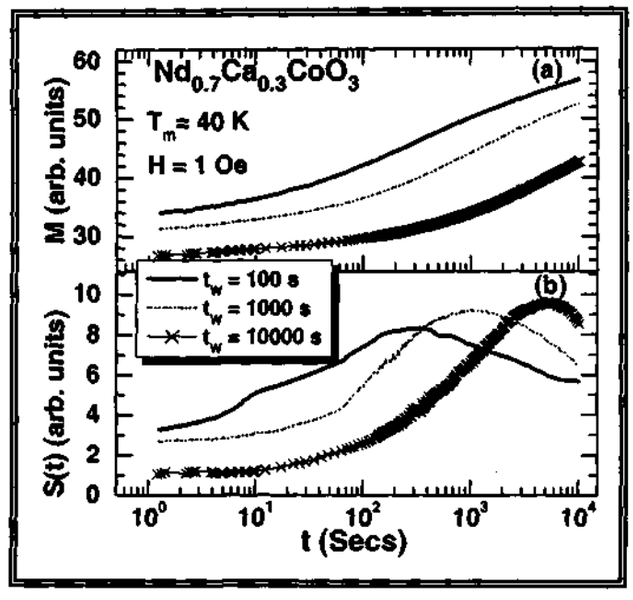

Figure 3.35 ZFC-relaxation measurements on $Nd_{0.7}Ca_{0.3}CoO_3$ at $T_m = 40$ K similar to Pr.

We have investigated memory effects using the zero-field-cooled magnetization vs. temperature experiments. First, a reference experiment was made according to the ZFC protocol described earlier. Then, a memory curve was recorded, with the additional feature that cooling was halted at a stop temperature for some hours during which the sample ages (c.f. aging experiments). This slows down the dynamics at temperatures around the stop temperature, which sustains when the temperature is decreased, and appears as a dip in the $M_{ZFC}(T)$ curve at the stop temperature on re-heating the sample. To clearly illustrate memory, it is convenient to plot the difference between the reference and the memory curve. It may be noted that a specific characteristic of a spin glass phase (ordinary or re-entrant) is the memory behavior, whereas a disordered and frustrated FM phase shows little or no memory effect. In the case of $Pr_{0.7}Ca_{0.3}CoO_3$, the experiments were carried (a) with a halt at 30 K, (b) with a halt at 50 K and (c) with halts at both 30

and 50 K. The weak dc field applied in the measurement does not affect the non-equilibrium process intrinsic to the sample, but only works as a non-perturbing probe of the system.

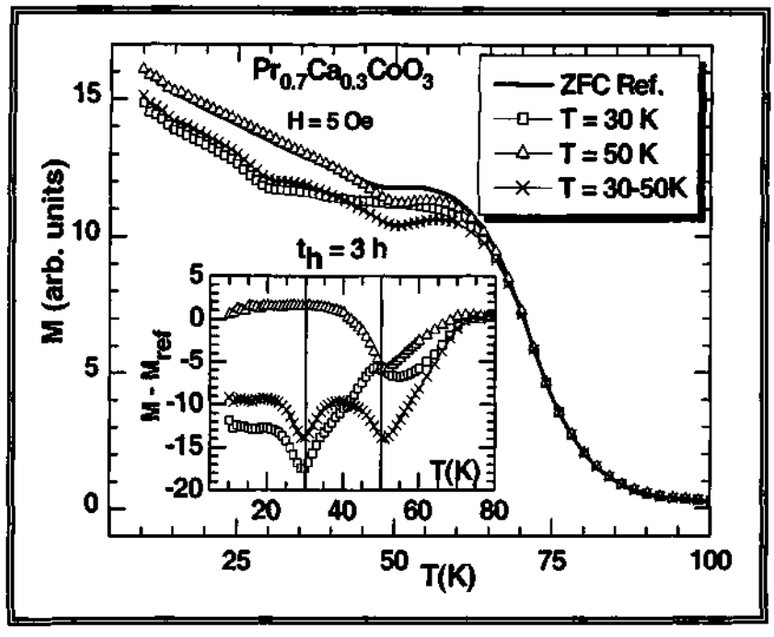

Figure 3.36 The temperature dependence of ZFC magnetization, M, (reference curve) and on imprinting memories of $Pr_{0.7}Ca_{0.3}CoO_3$ at two temperature stops (30 and 50 K) during cooling each for 3 hours. The inset shows the difference ($M-M_{ref}$) plot of the respective curves (c-axis parallel to the field, H = 5 Oe).

A memory effect is clearly observed as shown in Fig. 3.36, (a) at 30 K, (b) at 50 K and (c) at both 30 and 50 K after direct cooling from 100 K. The memory dip appears even more prominently on subtracting the reference curve as shown in the inset of Fig. 3.36.The memory experiments on $Nd_{0.7}Ca_{0.3}CoO_3$ at three different temperatures show similar results (see Fig. 3.37). In Fig. 3.37 (a), we show the reference curve along with two memory curves with halts at 35 K and 45 K, the inset corresponding to a halt at 40 K. We observe memory dips at the stop temperatures. The observed memory effects clearly

establish that both $Pr_{0.7}Ca_{0.3}CoO_3$ and $Nd_{0.7}Ca_{0.3}CoO_3$ behave like spin-glasses at the low temperatures.

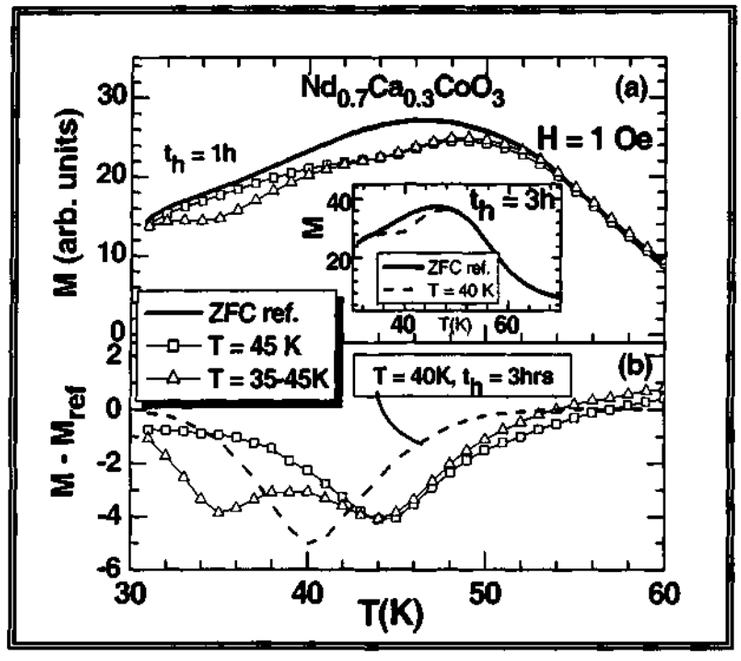

Figure 3.37 ZFC magnetization memory experiment on $Nd_{0.7}Ca_{0.3}CoO_3$; (a) the temperature dependence of ZFC magnetization, M, (reference curve) and on imprinting memories of two temperature stops (at 30 and 50 K) during cooling each for 1 hour and (b) the difference ($M-M_{ref}$) plot of the respective curves (c-axis parallel to the field, H = 1 Oe). The inset shows the memory curve corresponding to halting time 3 hours (T = 40K).

Conclusions

Although cobaltates of the type $La_{1-x}Sr_xCoO_3$ ($x \geq 0.3$) were considered to be itinerant ferromagnets, recent studies have revealed that these cobaltates show magnetic phase separation wherein relatively large FM clusters or domains associated with a distinct T_C, coexist with small magnetic clusters showing glassy behavior [17]. $La_{1-x}Sr_xCoO_3$ compositions also show an insulator-metal transition with increasing x since the large FM clusters are metallic. Previous studies of polycrystalline samples of $La_{0.7-x}Ln_xCa_{0.3}CoO_3$ (Ln = Pr, Nd, Gd and Dy) reinforce the phase separation scenario wherein

large carrier-rich FM clusters and carrier-poor smaller clusters coexist. Such magnetic phase separation would be expected to be sensitive to the size of A-site cations. As the size of the A-site cations decreases as in $Pr_{0.7}Ca_{0.3}CoO_3$ and $Nd_{0.7}Ca_{0.3}CoO_3$, we would expect a situation where a small magnetic clusters to dominate, favoring glassy behavior. Evidence for such behavior was found in our studies of polycrystalline samples of these cobaltates. Measurements on single crystalline $Pr_{0.7}Ca_{0.3}CoO_3$ and $Nd_{0.7}Ca_{0.3}CoO_3$ show these effects even more vividly. Thus, both these cobaltates do not exhibit a ferromagnet-like magnetic behavior with well defined T_C (associated with large FM clusters or domains). Instead, they behave like spin-glasses at low temperatures. In other words, because of the small A-site cations radius, $\langle r_A \rangle$, these two cobaltates are genuine spin-glasses. Accordingly, both these cobaltates are insulators. The properties of $Pr_{0.7}Ca_{0.3}CoO_3$ found here are comparable to those reported by Tsubouchi et al [55], but the interpretation of the results provided here in the light of the non-equilibrium properties is different.

3.4.3 Cation size-disorder as the crucial determinant of the unusual magnetic and electronic properties of $Gd_{0.5}Ba_{0.5}CoO_3$

The unit cell parameters are presented in Table 3.2 along with the weighted radius, $\langle r_A \rangle$, and the σ^2 value for the cobaltates, $Ln_{0.5}Ba_{0.5}CoO_3$ (Ln = La, Nd and Gd). The $\langle r_A \rangle$-

Table 3.2 Structure and properties of $Ln_{0.5}Ba_{0.5}CoO_{3-\delta}$ (Ln = La, Nd and Gd)

Composition	$\langle r_A \rangle$ (Å)	σ^2 (Å^2)	Lattice parameters (Å)[a]			Space group	V (Å^3)
			a	*b*	*c*		
$La_{0.5}Ba_{0.5}CoO_{2.98}$	1.485	0.016	5.4859	-	-	*R*3*c*	165
$Nd_{0.5}Ba_{0.5}CoO_{2.94}$	1.317	0.024	11.7165	11.6842	7.6019	*Pmmm*	1041
$Gd_{0.5}Ba_{0.5}CoO_{2.90}$	1.289	0.033	11.7077	11.6334	7.5332	*Pmmm*	1026
$Gd_{0.5}Sr_{0.5}CoO_{2.98}$	1.209	0.010	5.3746	7.5601	5.3746	*Pnma*	218

[a] Uncertainty is approximately ±0.004.

values were calculated using the Shannon radii for 12-coordination in the case of rhombohedral cobaltates and for 9-coordination in the case of the orthorhombic ones.

In Fig. 3.38, we show the temperature variation of the dc magnetic susceptibility of $Gd_{0.5}Ba_{0.5}CoO_{2.9}$ measured at a relatively high field of 5 kOe. There is a definitive increase in the susceptibility around 280 K as in a ferromagnet, but there is no saturation.

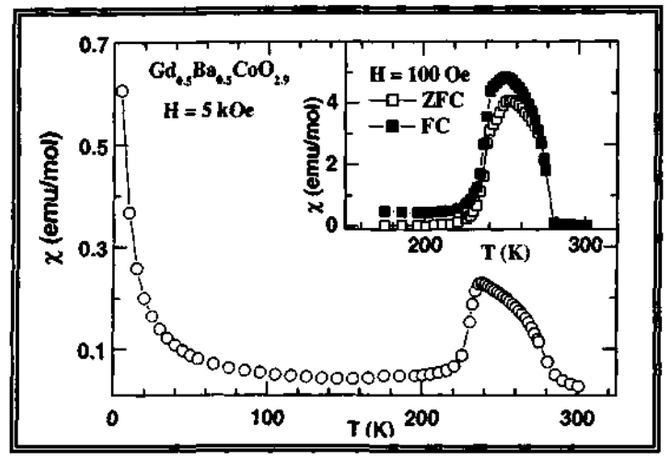

Figure 3.38 Dc magnetic susceptibility of $Gd_{0.5}Ba_{0.5}CoO_{2.9}$. The inset shows the FC and ZFC measurements.

The highest value of susceptibility reached around 240 K gives an average magnetic-moment of only 0.21 μ_B. This is to be contrasted with $Nd_{0.5}Ba_{0.5}CoO_{2.94}$ and $La_{0.5}Ba_{0.5}CoO_{2.95}$ which exhibit sharp ferromagnetic transitions

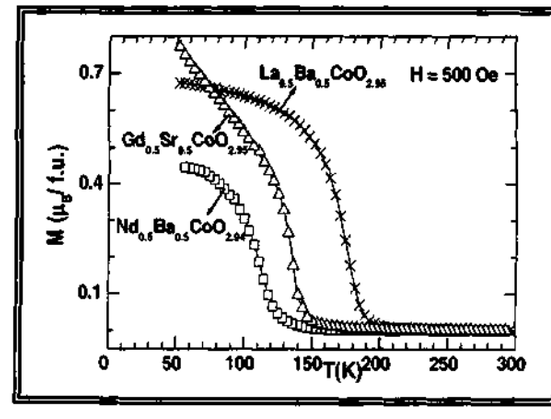

Figure 3.39 Temperature variation-magnetization of $La_{0.5}Ba_{0.5}CoO_{2.95}$, $Nd_{0.5}Ba_{0.5}CoO_{2.94}$ and $Gd_{0.5}Sr_{0.5}CoO_{2.95}$.

with T_C values of 130 K and 190 K respectively with considerably higher saturation moments of 0.45 and 0.67 μ_B respectively as shown in Fig. 3.39. The fact that these T_C values are much lower than the onset temperature of the so-called ferromagnet type transition of $Gd_{0.5}Ba_{0.5}CoO_{2.9}$ at 280 K shows that the latter is not a genuine ferromagnetic transition. The inset in Fig. 3.38, shows the dc susceptibility of the ZFC and FC conditions (H = 100 Oe). There is no appreciable difference in the behavior of the ZFC and FC samples. Fig. 3.38, also shows a sharp drop in the susceptibility around 230 K, suggesting antiferromagnetic ordering below this temperature. We observe low-field hysteresis at 250 K, which disappears below 230 K (Fig. 3.39), indicating the presence of ferromagnetic interactions in the 280-230 K regime.

In Fig. 3.40, we show the temperature variation of the electrical resistivity of $Gd_{0.5}Ba_{0.5}CoO_{2.9}$ and $Nd_{0.5}Ba_{0.5}CoO_{2.94}$. There is sharp increase in the resistivity of $Gd_{0.5}Ba_{0.5}CoO_{2.9}$ around 350 K, but no anomaly in resistivity is observed at the 230 K transition. We find that the 350 K transition is not accompanied by a change in crystal structure, in conformity with earlier observations. There is only the expected thermal-

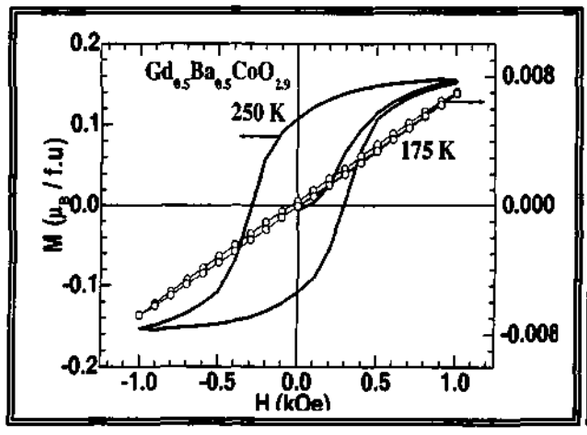

Figure. 3.39 Low field magnetic hysteresis of $Gd_{0.5}Ba_{0.5}CoO_{2.9}$ at 250 K and 175 K.

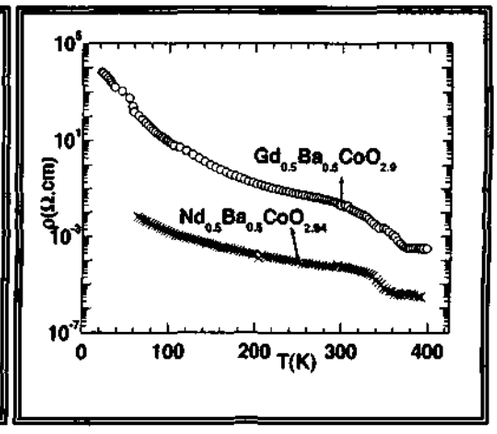

Figure 3.40 Electrical resistivity of $Ln_{0.5}Ba_{0.5}CoO_3$ (Ln = Nd and Gd).

expansion across the transition. The 350 K transition is unaffected by Nd substitution in the Gd site and occurs in pure $Nd_{0.5}Ba_{0.5}CoO_{2.94}$ as well (Fig. 3.40). The transition seems to be insensitive to oxygen stoichiometry and occurs in $Gd_{0.5}Ba_{0.5}CoO_{2.5}$ with only Co^{3+} ions [56], showing thereby that charge ordering here involves the A-site cations, although there will be some associated ordering of the B-site ions in the mixed-valent $Gd_{0.5}Ba_{0.5}CoO_{2.9}$. Charge ordering occurs in the paramagnetic regime. On cooling, the charge ordered-state in $Gd_{0.5}Ba_{0.5}CoO_{2.9}$ transforms to a magnetic state where ferromagnetic interactions dominate, but this state is stable only in the 280-230 K range, becoming antiferromagnetic at 230 K. The transition at 280 K is somewhat comparable to the re-entrant ferromagnetic transition in rare-earth manganates of the type $La_{0.25}Nd_{0.25}Ca_{0.5}MnO_3$ where $T_{CO} > T_C$ [57]. The magnetic transition in $Gd_{0.5}Ba_{0.5}CoO_{2.9}$ at 280 K is, however, not to a ferromagnetic state as mentioned earlier. What we have is a system exhibiting paramagnetic–ferromagnetic-like-antiferromagnetic transitions. We have examined the antiferromagnetic state by measuring M - H data at high fields and observed an unusual high-field hysteresis at 175 K in the 30–80 kOe range as shown in Fig. 3.41.

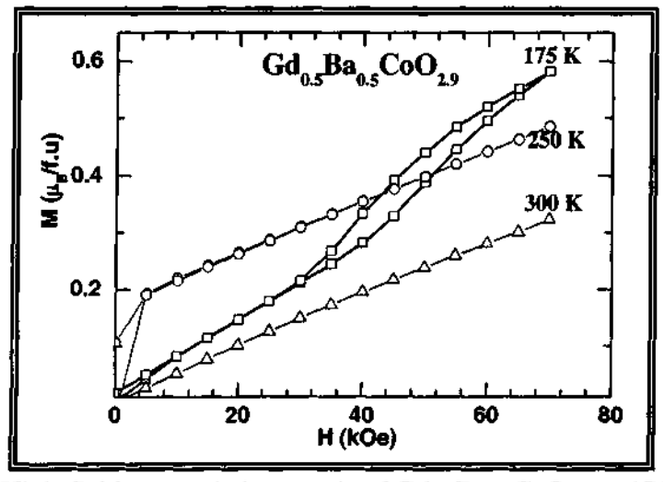

Figure 3.41 High-field magnetic hysteresis of $Gd_{0.5}Ba_{0.5}CoO_{2.9}$ at 175 K, which disappears at higher temperatures.

The antiferromagnetic state is transformed to the ferromagnetic state on application of magnetic fields. The ac susceptibility measurements at different frequencies show a sharp peak around 275 K which is frequency-independent (Fig. 3.42). In addition, we see small broad peaks around the main peak, possibly representing transitions arising from different clusters or domains co-existing in the sample. These features suggest the presence of inhomogeneties or electronic phase separation in $Gd_{0.5}Ba_{0.5}CoO_{2.9}$ similar to that in $La_{0.25}Nd_{0.25}Ca_{0.5}MnO_3$ and other charge-ordered rare-earth manganates [7, 57, 58]. The ferromagnetic interactions are comparable to those responsible for the cluster glass behavior reported in some of the $La_{0.5-x}Sr_xCoO_3$ compositions [14, 31].

It is instructive to compare the magnetic properties of $Gd_{0.5}Ba_{0.5}CoO_{2.9}$ with those of $Gd_{0.5}Ba_{0.5}CoO_{2.75}$ where only the Co^{3+} ions are present [56, 59]. This material undergoes a metal-insulator type transition around 360 K in the resistivity data, which has been assigned to a low-spin state to high-spin state transition via an intermediate-spin state. This assignment seems to be wrong. The resistivity transition is more likely to be due to the charge-ordering of the A-site cations referred to earlier. There appears to be a paramagnetic-ferromagnetic-like - antiferromagnetic transition in the 300-250 K range in the Co^{3+} system as well. The ferromagnetic-antiferromagnetic competition here is reminiscent of a canted antiferromagnet such as La_2CuO_4, the antiferromagnetic ordering being quenched by magnetic fields. The presence of 33 % Co^{4+} in $Gd_{0.5}Ba_{0.5}CoO_{2.9}$ would change many of these properties, and electronic phase separation and related factors assume greater importance. The crucial role of cation disorder in $Gd_{0.5}Ba_{0.5}CoO_{2.9}$ is clearly evidenced when we compare its properties with those of $Gd_{0.5}Sr_{0.5}CoO_{2.95}$. The

Sr derivative shows a ferromagnetic transition with a T_C of 140 K (see Fig. 3.39) although the $\langle r_A \rangle$ is considerably smaller (1.209 Å). This can only be because the σ^2 value is only 0.0103 $Å^2$ in the Sr derivative. Accordingly, $Gd_{0.17}Pr_{0.33}Ba_{0.35}Sr_{0.15}CoO_3$ with $\langle r_A \rangle$ equal to that of $Gd_{0.5}Ba_{0.5}CoO_{2.9}$ is ferromagnetic (T_C = 155 K), since σ^2 is reduced to 0.0211 $Å^2$.

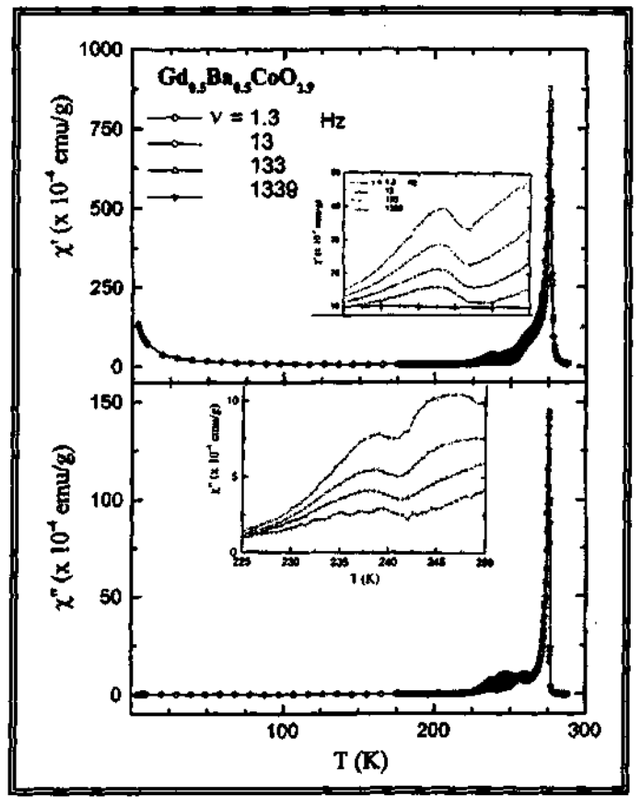

Figure 3.42 The ac susceptibility data of $Gd_{0.5}Ba_{0.5}CoO_{2.9}$. Inset shows expanded version over a narrow temperature range.

Conclusions

$Gd_{0.5}Ba_{0.5}CoO_{2.9}$ which is charge-ordered at ordinary temperatures, exhibits an increase in magnetization around 280 K, reaching a rather small value of the magnetic moment (−0.21μ_B /f.u.) followed by a sharp drop in magnetization around 230 K to an

antiferromagnetic state. Application of high magnetic fields destroys the anti-ferromagnetic state. The behavior is consistent with the presence of magnetic phase separation as supported by ac susceptibility measurements. The ferromagnetic metallic state generally found in $La_{0.5}Ba_{0.5}CoO_3$ and other analogous cobaltates of the type $Ln_{0.5}A_{0.5}CoO_3$ does not manifest itself in $Gd_{0.5}Ba_{0.5}CoO_{2.9}$ mainly because of the cation size-induced disorder, arising from the size mismatch between the Gd and the Ba ions.

$Gd_{0.5-x}Ln_xBa_{0.5}CoO_3$ (Ln = La and Nd) and $Gd_{0.5}Ba_{0.5-x}Sr_xCoO_3$

The crystal structure and unit cell parameters of $Gd_{0.5-x}Ln_xBa_{0.5}CoO_3$ (Ln = La and Nd) series of cobaltates are listed in Table 3.3 along with the weighted average radius $\langle r_A \rangle$, and the σ^2 values. In Tables 3.4 and 3.5, we have presented the structural parameters of $La_{0.5-x}Nd_xBa_{0.5}CoO_3$ and $Gd_{0.5}Ba_{0.5-x}Sr_xCoO_3$ respectively along with the ferromagnetic T_C values.

Table 3.3 Structure and properties of $Gd_{0.5-x}Ln_xBa_{0.5}CoO_3$

Composition x	$\langle r_A \rangle$ (Å)	σ^2 (Å^2)	Space group	Lattice parameters (Å)			V (Å^3)
				a	b	c	
0.0	1.289	0.033	*Pmmm*	11.708	11.633	7.533	1026
Ln = Nd							
0.1	1.294	0.031	*Pmmm*	11.729	11.660	7.535	1030
0.2	1.300	0.029	*Pmmm*	11.752	11.668	7.548	1035
0.3	1.305	0.028	*Pmmm*	11.699	11.656	7.583	1034
0.4	1.311	0.026	*Pmmm*	11.759	11.686	7.586	1042
0.5	1.317	0.024	*Pmmm*	11.717	11.684	7.602	1041
Ln = La							
0.1	1.299	0.030	*Pmmm*	11.673	11.687	7.575	1033
0.25	1.316	0.025	*Pmmm*	11.712	11.684	7.630	1044
0.3	1.321	0.024	*Pmmm*	11.717	11.683	7.640	1046
0.4	1.459	0.028	$R\bar{3}C$	5.481	—	—	164
0.5	1.485	0.016	$R\bar{3}C$	5.486	—	—	165

Table 3.4 Structure and properties of $La_{0.5-x}Nd_xBa_{0.5}CoO_3$

Composition	$\langle r_A \rangle$	σ^2	Space	Lattice parameters (Å)			T_c
x	(Å)	(Å^2)	group	a	b	c	(K)
0.0	1.485	0.016	$R\bar{3}C$	5.486	—	—	190
0.1	1.476	0.019	$R\bar{3}C$	5.482	—	—	180
0.2	1.332	0.019	*Pmmm*	11.688	11.651	7.692	177
0.3	1.327	0.021	*Pmmm*	11.711	1.676	7.622	164
0.4	1.322	0.022	*Pmmm*	11.704	11.691	7.623	150
0.5	1.317	0.024	*Pmmm*	11.717	11.684	7.602	130

Table 3.5 Structure and properties of $Gd_{0.5}Ba_{0.5-x}Sr_xCoO_3$

Composition	$\langle r_A \rangle$	σ^2	Space	Lattice parameters (Å)			T_c
x	(Å)	(Å^2)	group	a	b	c	(K)
0.0	1.289	0.033	*Pmmm*	11.708	11.633	7.533	—
0.1	1.273	0.030	*Pmmm*	11.653	11.608	7.522	—
0.2	1.257	0.026	*Pmmm*	11.587	11.571	7.524	—
0.3	1.241	0.021	*Pmmm*	11.582	11.555	7.499	133
0.4	1.225	0.016	*Pnma*	5.389	7.599	5.380	145
0.5	1.209	0.010	*Pnma*	5.371	7.558	5.371	150

Before we discuss the results of our investigations of the cobaltate compositions of the type $Gd_{0.5-x}Ln_xBa_{0.5}CoO_3$ (Ln = La and Nd) and $Gd_{0.5}Ba_{0.5-x}Sr_xCoO_3$, it would be in order to briefly examine the properties of the parent compound $Gd_{0.5}Ba_{0.5}CoO_{2.9}$ based on the literature [35-37] and our own measurements. In Fig. 3.43 (a), we compare the magnetization data of $Ln_{0.5}Ba_{0.5}CoO_{3-\delta}$ with Ln = La, Nd and Gd to show how $Gd_{0.5}Ba_{0.5}CoO_{2.9}$ is uniquely different from $La_{0.5}Ba_{0.5}CoO_{2.95}$ and $Nd_{0.5}Ba_{0.5}CoO_{2.94}$. The last two cobaltates show FM transitions around 190 and 130 K respectively with

saturation magnetic moments of 1.43 and 0.57 μ_B. $Gd_{0.5}Ba_{0.5}CoO_{2.9}$ shows an increase in magnetization starting around 280 K, reaching a maximum value around 240 K, with an associated magnetic moment of only 0.21 μ_B.

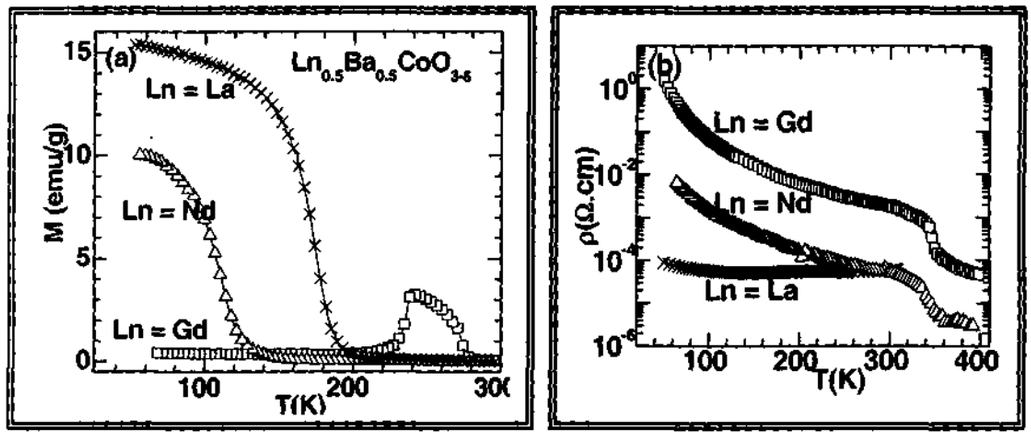

Figure 3.43 Temperature variation of (a) the magnetization and (b) the electrical resistivity of $Ln_{0.5}Ba_{0.5}CoO_{3-\delta}$ (Ln = La, Nd or Gd).

The magnetization drops sharply around 230 K to an antiferromagnetic state, and the AFM transition is destroyed by magnetic fields. The increase in magnetization in $Gd_{0.5}Ba_{0.5}CoO_{2.9}$ at 280 K is clearly not due to a FM transition. A FM transition should have occurred at temperatures lower than 130 K, considering that Gd^{3+} is much smaller than Nd^{3+}. The observed magnetic properties of $Gd_{0.5}Ba_{0.5}CoO_{2.9}$ could arise from electronic phase separation arising from the large cation size-disorder. Electrical properties of $Gd_{0.5}Ba_{0.5}CoO_{2.9}$ are also different from those of $La_{0.5}Ba_{0.5}CoO_{2.95}$ as can be seen from Fig. 3.43 (b). Thus, $La_{0.5}Ba_{0.5}CoO_{2.95}$ shows a nearly temperature-independent resistivity from 300 K to 20 K. $Nd_{0.5}Ba_{0.5}CoO_{2.94}$ and $Gd_{0.5}Ba_{0.5}CoO_{2.9}$, on the other hand, show transitions around 360 K due to charge-ordering. The resistivity of the Gd derivative is much higher than that of the Nd derivative, although both are insulators.

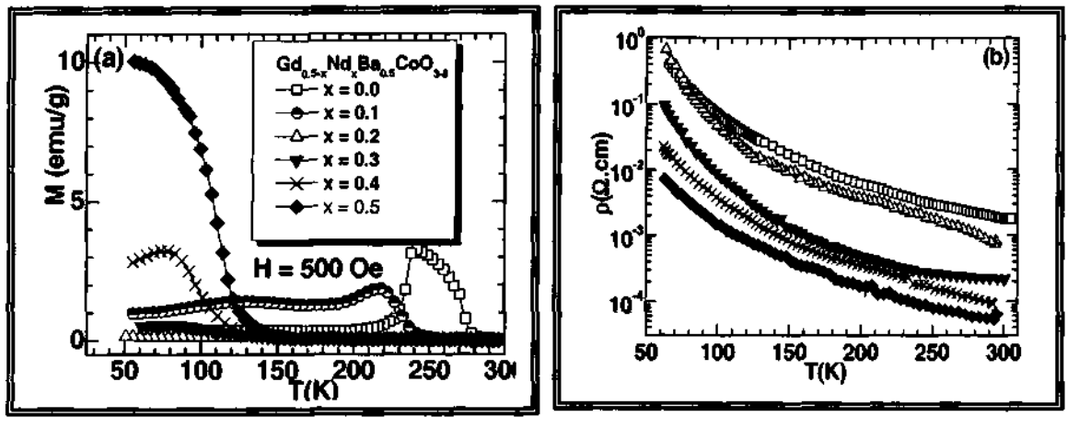

Figure 3.44 Temperature variation of (a) the magnetization and (b) the electrical resistivity of $Gd_{0.5-x}Nd_xBa_{0.5}CoO_{3-\delta}$.

In order to study the effects of cation size, we have examined the magnetic and electrical properties of several series of cobaltates. We show the magnetization and resisitivity data of $Gd_{0.5-x}Nd_xBa_{0.5}CoO_3$ in Fig. 3.44. With increase in x, we observe the evolution of ferromagnetism. What is interesting is that the 280 K magnetic transition of $Gd_{0.5}Ba_{0.5}CoO_{2.9}$ disappears even when $x \geq 0.1$. When Ln = Nd, we observe a complex behavior for $x = 0.1$, with a magnetic transition around 220 K. We observe no obvious magnetic transitions in the 200-280 K region for $0.1 < x < 0.4$. The $x = 0.3$ composition shows a small increase in magnetization around 125 K, and the increase becomes more marked when $x = 0.4$. When Ln = La, there is no magnetic transition in the 200-280 K region for $0.1 < x < 0.25$. A distinct FM transition occurs at $x = 0.5$ in the case of Nd, and at $x = 0.4$ in the case of La. It is interesting that the FM characteristics start emerging at low temperatures (< 150 K) in these cobaltate compositions around a $\langle r_A \rangle$ value of 1.30 Å. Clearly with increase x, the size of ferromagnetic clusters increases, eliminating the phase separation at small x, caused by size disorder. It is noteworthy that in $Pr_{1-x}A_xCoO_3$ ($0 \leq x \leq 0.5$, A = Sr, Ba) spin or cluster glass behavior has been found at low temperatures [60].

Spin glass behavior is found in $La_{1-x}Sr_xCoO_3$ ($x < 0.1$), but with increase in x ferromagnetism manifests itself [61].The resistivity data of the $Gd_{0.5-x}Nd_xBa_{0.5}CoO_3$ compositions show insulating behavior, but the resistivity decreases significantly with increase in x, the $x = 0.5$ composition exhibiting the lowest resistivity (Fig. 3.44 (b)). When Ln = La, the resistivity decreases with increase in x, becoming temperature-independent for $x = 0.5$. All the other compositions are insulating. Considering that with increase in x, there is significant increase in $\langle r_A \rangle$ in the two $Gd_{0.5-x}Ln_xBa_{0.5}CoO_3$ (Ln = La, Nd) series of cobaltates, the changes observed can essentially be attributed to the effects of cation size. Our measurements on the $La_{0.5-x}Nd_xBa_{0.5}CoO_3$ system confirm this observation. In Fig. 3.45, we show the magnetization and resistivity data of this system. There is a decrease in T_C with increase in x in this series as expected, with an accompanying increase in the resistivity. Although the changes in the properties in this series of cobaltates is essentially due to cation size effects, it should be noted that there is also a small increase in σ^2 with increasing x in this system.

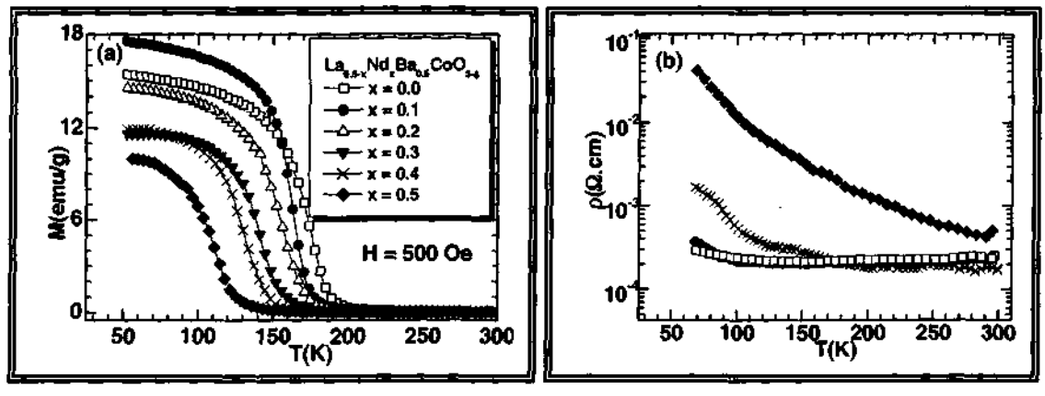

Figure 3.45 Temperature variation of (a) the magnetization and (b) the electrical resistivity of $La_{0.5-x}Nd_xBa_{0.5}CoO_{3-\delta}$.

In order to understand the role of size-disorder due to cation size mismatch, we have investigated two series of cobaltates with fixed $\langle r_A \rangle$ values of 1.317 and 1.289 Å, corresponding to those of $Nd_{0.5}Ba_{0.5}CoO_3$ and $Gd_{0.5}Ba_{0.5}CoO_3$. The structural parameters of $Ln_{0.5-x}Ln'_xA_{0.5-y}A'_yCoO_3$, cobaltates are given in Table 3.6, along with T_C values.

Table 3.6 Structure and properties of $Ln_{0.5-x}Ln'_xA_{0.5-y}A'_yCoO_3$ with fixed $\langle r_A \rangle$ values

Composition	σ^2 (Å^2)	Space group	Lattice parameters (Å)			T_c (K)
			a	*b*	*c*	
$\langle r_A \rangle = 1.317$ Å						
$La_{0.22}Pr_{0.28}Ba_{0.4}Sr_{0.1}CoO_3$	0.0170	*Pnma*	5.470	7.726	5.471	190
$Pr_{0.5}Ba_{0.45}Sr_{0.05}CoO_3$	0.0200	*Pmmm*	11.688	11.666	7.639	166
$Nd_{0.1}Pr_{0.4}Ba_{0.46}Sr_{0.04}CoO_3$	0.0207	*Pmmm*	11.682	11.650	7.634	160
$Nd_{0.5}Ba_{0.5}CoO_3$	0.0235	*Pmmm*	11.717	11.684	7.602	130
$Pr_{0.39}Gd_{0.11}Ba_{0.5}CoO_3$	0.0239	*Pmmm*	11.715	11.674	7.609	—
$\langle r_A \rangle = 1.289$ Å						
$La_{0.29}Gd_{0.21}Ba_{0.3}Sr_{0.2}CoO_3$	0.0184	*Pnma*	5.447	7.685	5.425	220
$Gd_{0.17}Pr_{0.33}Ba_{0.35}Sr_{0.15}CoO_3$	0.0211	*Pmmm*	11.633	11.591	7.600	155
$Gd_{0.22}Nd_{0.28}Ba_{0.4}Sr_{0.1}CoO_3$	0.0248	*Pmmm*	11.658	11.639	7.569	128
$Gd_{0.1}Sm_{0.4}Ba_{0.42}Sr_{0.08}CoO_3$	0.0276	*Pmmm*	11.658	11.638	7.551	—
$Gd_{0.35}Nd_{0.15}Ba_{0.45}Sr_{0.05}CoO_3$	0.0287	*Pmmm*	11.728	11.651	7.542	—
$Gd_{0.5}Ba_{0.5}CoO_3$	0.0329	*Pmmm*	11.708	11.633	7.533	—

We show the results of the magnetization measurements in Figs 3.46 (a) and 3.47 (a) respectively. The data in Fig. 3.46 (a) for a fixed $\langle r_A \rangle$ of 1.317 Å, show that the T_C -

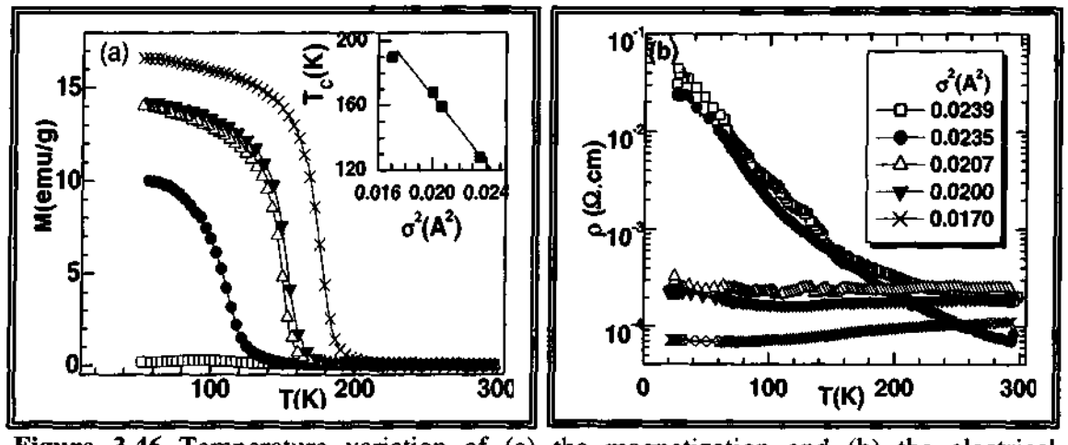

Figure 3.46 Temperature variation of (a) the magnetization and (b) the electrical resistivity of $Ln_{0.5-x}Ln'_xA_{0.5-y}A'_yCoO_3$ with a fixed $\langle r_A \rangle$ value of 1.317Å.

decreases as σ^2 increases, eventually destroying ferromagnetism at a high value of σ^2 ($\approx$ 0.024 Å^2). The linear relation between T_C and σ^2 gives a slope of 10830 ± 300 K Å^{-2} with an intercept, T_C^o, of 385 ± 2 K. Here, T_C^o represents the T_C value of the disorder-free cobaltate in this series.

The data in Fig. 3.47 (a), corresponding to a fixed $\langle r_A \rangle$ of 1.289 Å, are interesting. With decrease in σ^2, the magnetic behavior of this system changes markedly. Thus, when σ^2 = 0.028 Å^2, we do not see the magnetic anomaly of $Gd_{0.5}Ba_{0.5}CoO_{2.9}$ at 280 K. When σ^2 = 0.021 Å^2, we observe a ferromagnetic transition with a T_C of ~ 160 K. When σ^2 is 0.0184 Å^2, the T_C reaches 220 K, a value higher than that of $La_{0.5}Ba_{0.5}CoO_3$.

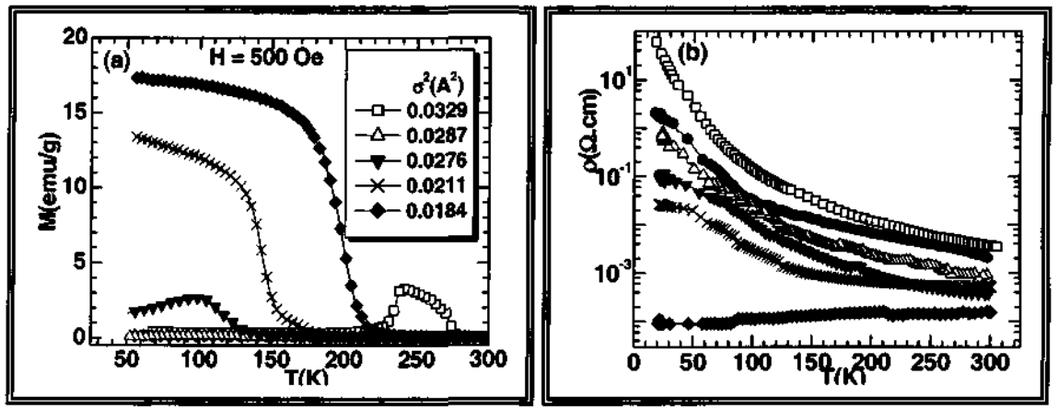

Figure 3.47 Temperature variation of (a) the magnetization and (b) the electrical resistivity of $Ln_{0.5-x}Ln'_xA_{0.5-y}A'_yCoO_3$ with a fixed $\langle r_A \rangle$ value of 1.289Å.

These data clearly demonstrate that the absence of ferromagnetism in $Gd_{0.5}Ba_{0.5}CoO_3$, as well as its unusual magnetic properties, such as the magnetic anomaly at 280 K, are almost entirely due to the disorder arising from the cation size mismatch. Such size-disorder can give rise to electronic phase separation as in rare earth manganates [7, 13]. Thus, in the series of compounds $La_{0.7-x}Ln_xCa_{0.3}MnO_3$ (Ln = Pr, Nd, Gd and Y) the size disorder increases with the decreasing size of the Ln ion and increasing *x*.

Accordingly, phase separation occurs at lower x with decreasing size. The situation is similar to $Gd_{0.5-x}Ln_xBa_{0.5}CoO_3$ (Ln = La and Nd) compounds.

The electrical resistivity behavior of the two series of cobaltates with fixed $\langle r_A \rangle$ values corroborates the results from the magnetic measurements. In Figs. 3.46 (b) and 3.47 (b), we show the resistivity data for the two series to demonstrate how the resistivity increases with increase in σ^2. Interestingly, we observe disorder-induced insulator-metal transitions in both the series of cobaltates, the cobaltate compositions with $\sigma^2 < 0.02$ Å^2 showing metallic behavior. Such disorder-induced insulator-metal transitions are indeed novel. Further support for the observation that cation size-disorder crucially determines the properties of $Gd_{0.5}Ba_{0.5}CoO_{2.9}$ is provided by our study of the $Gd_{0.5}Ba_{0.5-x}Sr_xCoO_3$ series of cobaltates. Here, the $x = 0.5$ composition, corresponding to $Gd_{0.5}Sr_{0.5}CoO_3$, has a smaller $\langle r_A \rangle$ than $Gd_{0.5}Ba_{0.5}CoO_{2.9}$, and yet it shows ferromagnetic features [Fig. 3.48(a)].

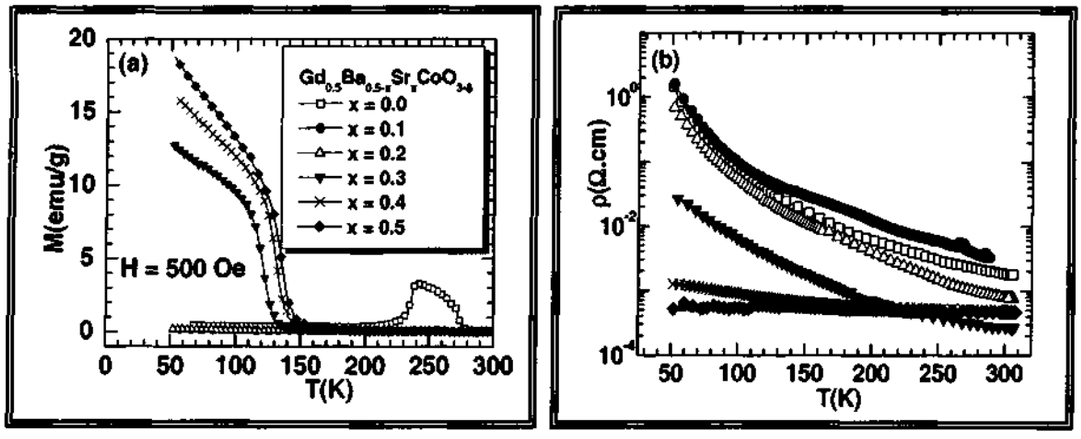

Figure 3.48 Temperature variation of (a) the magnetization and (b) the electrical resistivity of the cobaltates $Gd_{0.5}Ba_{0.5-x}Sr_xCoO_{3-\delta}$.

The 280 K magnetic anomaly of $Gd_{0.5}Ba_{0.5}CoO_3$ disappears even when $x = 0.1$ and the apparent T_C increases with increase in x in the series. This behavior is clearly due

to size disorder, since σ^2 decreases with increase in x. Accordingly, this system exhibits an insulator-metal transition with increase in x or decrease in σ^2 (see figure 3.48 (b)). It appears that a σ^2 value larger than 0.02 $Å^2$ generally destroys ferromagnetism in the cobaltates and changes the metal into an insulator.

Conclusions

The present investigation shows that the ferromagnetic metallic state, generally found in $La_{0.5}Ba_{0.5}CoO_{2.95}$ and other analogous cobaltates of the type $Ln_{0.5}A_{0.5}CoO_{3-\delta}$, does not manifest itself in $Gd_{0.5}Ba_{0.5}CoO_{2.9}$, mainly because of the disorder arising from the size mismatch between the Gd and the Ba ions. Accordingly, if the size-disorder is reduced, keeping the average size of the A-site cations the same, the material becomes ferromagnetic, reaching a T_C of 220 K. It appears that reducing the size-disorder diminishes the electronic phase separation in this system. The crucial role of size-disorder is also evidenced in the properties of $Gd_{0.5}Ba_{0.5-x}Sr_xCoO_{3-\delta}$, where with increasing x, the material becomes ferromagnetic, although the $\langle r_A \rangle$ decreases.

3.4.4 Effects of large cation size-disorder on the magnetic properties of the rare earth cobaltates, $Ln_{0.5}Ba_{0.5}CoO_3$ (Ln = Dy and Er)

For, $Gd_{0.5-x}Ln_xBa_{0.5}CoO_3$ (Ln = Dy or Er) series of cobaltates the unit cell parameters are presented in Table 3.7 along with the values of $\langle r_A \rangle$ and σ^2.

Table 3.7 Crystal Structure data of $Gd_{0.5-x}Ln_xBa_{0.5}CoO_3$ (Ln = Dy or Er)

Composition	$\langle r_A \rangle$ (Å)	σ^2 ($Å^2$)	Space group	Lattice parameters (Å)			V ($Å^3$)
				a	*b*	*c*	
x=0.00	1.289	0.033	*Pmmm*	11.708	11.633	7.533	1026
Ln=Dy							
x=0.25	1.283	0.035	*Pmmm*	11.726	11.599	7.522	1023
x=0.50	1.277	0.037	*Pmmm*	11.715	11.578	7.511	1019
Ln=Er							
x=0.05	1.286	0.034	*Pmmm*	11.688	11.631	7.472	1024
x=0.25	1.277	0.037	*Pmmm*	11.655	11.657	7.509	1020
x=0.50	1.266	0.042	$P6_3cm$	12.142	12.142	11.250	1436

In Fig.3.49, we compare the temperature variation of the dc magnetization and electrical resistivity of $Gd_{0.5}Ba_{0.5}CoO_{2.9}$ with that of $Dy_{0.5}Ba_{0.5}CoO_{2.91}$ and $Er_{0.5}Ba_{0.5}CoO_{2.9}$. We notice that the Dy derivative exhibits a magnetic anomaly similar to that of the Gd compound, except that the transition temperature is slightly higher (290 K), indicating that the magnetic anomaly is related to the size disorder. The Dy compound becomes antiferromagnetic at ~ 245 K. When the size disorder is increased further as in $Er_{0.5}Ba_{0.5}CoO_{2.9}$, the material shows no magnetic anomaly and is instead paramagnetic down to low temperatures. The room-temperature electrical resistivity increases with decrease in the size of rare earth ion in the order Er > Dy > Gd. The charge-ordering transition found at 360 K in $Gd_{0.5}Ba_{0.5}CoO_{2.9}$ occurs at 320 K in $Dy_{0.5}Ba_{0.5}CoO_{2.91}$, thereby decreasing the gap between the charge ordering and the magnetic transitions. $Er_{0.5}Ba_{0.5}CoO_{2.9}$, on the other hand, does not exhibit the charge-ordering transition.

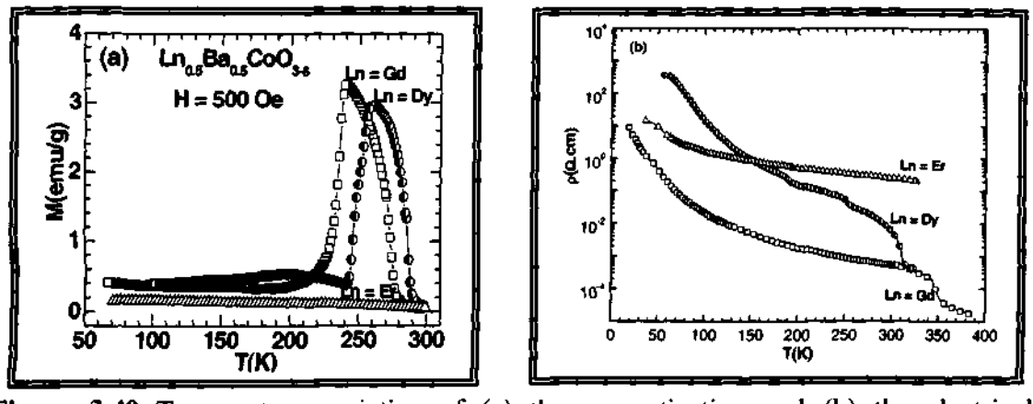

Figure 3.49 Temperature variation of (a) the magnetization and (b) the electrical resistivity of $Ln_{0.5}Ba_{0.5}CoO_3$ (Ln = Gd, Dy and Er).

In Fig. 3.50 we present the magnetic properties of $Gd_{0.5-x}Ln_xBa_{0.5}CoO_3$ with Ln = Dy and Er. The data show that when x = 0.25, the behavior is intermediate between that of the Gd and Dy derivatives. When Ln = Er, even 5 % doping reduces the magnitude of

magnetic anomaly markedly. Thus, the magnetic anomaly and the antiferromagnetic transition are not seen as clearly. The material becomes paramagnetic when $x = 0.25$. The electrical resistivity increases with increasing x, the $x = 0.5$ composition exhibiting the highest resistivity.

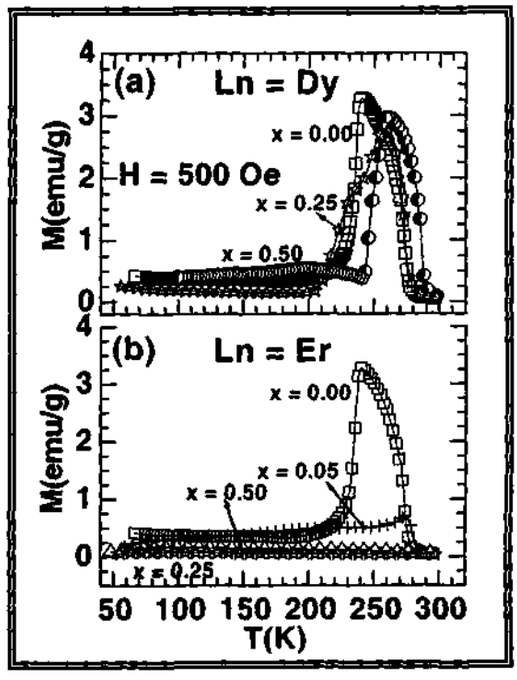

Figure 3.50 Temperature variation of the magnetization of $Gd_{0.5-x}Ln_xBa_{0.5}CoO_3$, with (a) Ln = Dy and (b) Ln = Er.

If the size disorder is indeed responsible for the properties of $Ln_{0.5}Ba_{0.5}CoO_3$ (Ln = Dy and Er), we would expect major changes in the magnetic and the electrical properties if the size-disorder is varied, keeping $\langle r_A \rangle$ constant. In order to understand the effect of size-disorder due to cation size mismatch on a quantitative basis, we have investigated two series of cobaltates with fixed $\langle r_A \rangle$ values of 1.277 and 1.266 Å corresponding to those of $Dy_{0.5}Ba_{0.5}CoO_{2.91}$ and $Er_{0.5}Ba_{0.5}CoO_{2.9}$ respectively. The structural parameters for two series of cobaltates of the general formula $Ln_{0.5-x}Ln'_xA_{0.5-y}A'_yCoO_3$, with fixed $\langle r_A \rangle$ values of 1.277 and 1.266 Å are given in Table 3.8.

Table 3.8 Structure and properties of $Ln_{0.5-x}Ln'_xA_{0.5-y}A'_yCoO_3$ with fixed $\langle r_A \rangle$ values

Composition	σ^2 (Å^2)	Space group	Lattice parameters (Å)			V (Å^3)
			a	*b*	*c*	
$\langle r_A \rangle$=1.277 Å						
$Pr_{0.5}Ba_{0.2}Sr_{0.3}CoO_3$	0.011	*Pnma*	5.435	7.668	5.421	225
$Nd_{0.3}Gd_{0.2}Ba_{0.39}Sr_{0.12}CoO_{2.95}$	0.021	*Pnma*	5.438	7.673	5.425	226
$Gd_{0.5}Ba_{0.43}Sr_{0.07}CoO_{2.93}$	0.031	*Pmmm*	11.717	11.599	7.53	1023
$Dy_{0.5}Ba_{0.5}CoO_{2.91}$	0.037	*Pmmm*	11.715	11.578	7.511	1019
$\langle r_A \rangle$=1.266 Å						
$La_{0.15}Pr_{0.35}Ba_{0.1}Sr_{0.4}CoO_3$	0.007	*Pnma*	5.422	7.653	5.417	224
$La_{0.25}Nd_{0.25}Ba_{0.1}Sr_{0.4}CoO_{2.95}$	0.008	*Pnma*	5.422	7.666	5.416	225
$La_{0.24}Gd_{0.26}Ba_{0.2}Sr_{0.3}CoO_{2.94}$	0.016	*Pnma*	5.436	7.678	5.418	226
$Gd_{0.5}Ba_{0.36}Sr_{0.14}CoO_{2.93}$	0.028	*Pmmm*	11.621	11.595	7.527	1014
$Er_{0.5}Ba_{0.5}CoO_{2.9}$	0.042	$P6_3cm$	12.142	12.142	11.250	1436

In Fig. 3.51, we show the magnetization and electrical resistivity data for the series with a fixed $\langle r_A \rangle$ value of 1.277 Å. With a small decrease in σ^2 from 0.037 to 0.031 Å^2, the material shows a small magnetic anomaly at 280 K, much smaller in magnitude than that in $Dy_{0.5}Ba_{0.5}CoO_{2.91}$. With a further decrease in σ^2 to 0.02 Å^2, the material shows a ferromagnetic transition with a T_C of ~ 180 K, the T_c increasing with decreasing σ^2. The material becomes metallic with decreasing σ^2 (Fig. 3.51(b)).

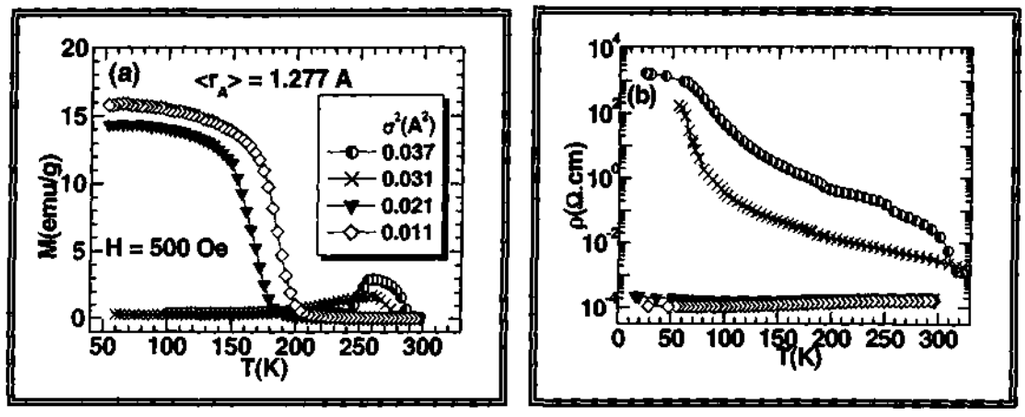

Figure 3.51 Temperature variation of (a) the magnetization and (b) the electrical resistivity of $Ln_{0.5-x}Ln'_xA_{0.5-y}A'_yCoO_3$ with a fixed $\langle r_A \rangle$ value of 1.277Å.

The data in Fig. 3.52 corresponding to a fixed $\langle r_A \rangle$ of 1.266 Å, are similar to those of the $\langle r_A \rangle$ = 1.277 Å series. The material remains essentially paramagnetic down to a σ^2 value of 0.02 $Å^2$, below which a clear ferromagnetic transition occurs, the T_C increasing with decreasing σ^2. Here again, the electrical resistivity decreases with decreasing σ^2, becoming metallic at small σ^2. It appears that these cobaltates start exhibiting ferromagnetism and metallicity only when σ^2 is around 0.02 $Å^2$ or less.

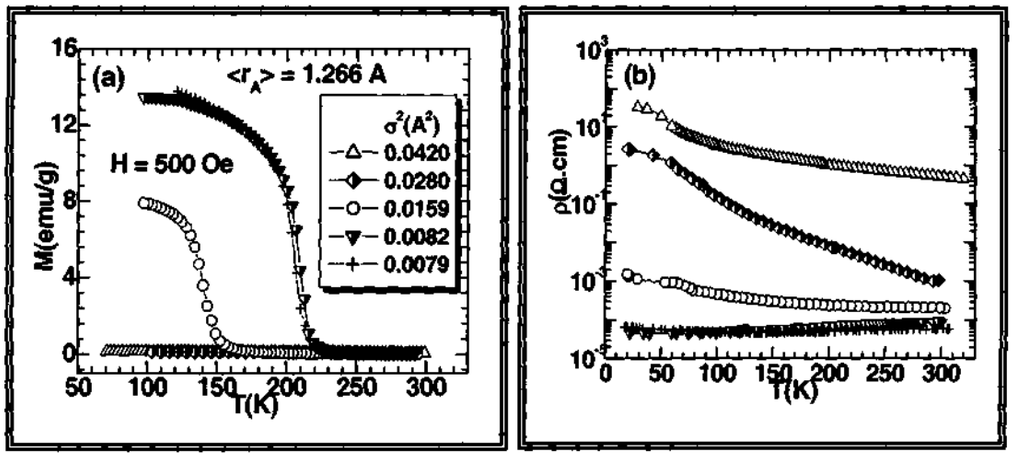

Figure 3.52 Temperature variation of (a) the magnetization, M, and (b) the electrical resistivity, ρ, of $Ln_{0.5-x}Ln'_xA_{0.5-y}A'_yCoO_3$ with a fixed $\langle r_A \rangle$ value of 1.266Å

Conclusions

Our present investigation shows that incorporation of large cation size-disorder in $Ln_{0.5}Ba_{0.5}CoO_{3-\delta}$ through small rare earth ions eliminates ferromagnetism, showing essentially paramagnetic behavior when the A-site cationic radius is very small or the disorder is large. Accordingly, keeping $\langle r_A \rangle$ constant and decreasing the size-disorder results in the progressive appearance of ferromagnetism and metallicity. The complete elimination of the magnetic anomalies arising from significant ferromagnetic interactions by large size-disorder is noteworthy.

3.5 REFERENCES

1. J. B. Goodenough, J. Phys. Chem. Solids, **6**, 287 (1958); G. H. Jonker, J. Appl. Phys., **37**, 1424 (1966).
2. W. H. Madhusudan, K. Jagannathan, P. Ganguly and C. N. R. Rao, J. Chem. Soc. Dalt. Trans., 1397 (1980).
3. C. N. R. Rao, Int. Rev. Phys. Chem., **4**, 19, (1985); T. Arunarkavalli, G. U. Kulkarni and C. N. R. Rao, J. Solid State Chem., **107**, 299 (1993).
4. D. N. H. Nam, K. Jonason, P. Nordblad, N. V. Khiem, and N. X. Phuc, Phys. Rev. B, **59**, 4189 (1999); Y. Kobayashi, N. Fujiwara, S. Murata, K. Asai, and H. Yasuoka, Phys. Rev. B, **62**, 410 (2000); F. Fauth, E. Suard, and V. Caignert, Phys. Rev. B, **65**, 060401 (2002).
5. W. Kobayashi, S. Ishiwata, I. Terasaki, M. Takano, I. Grigoraviciute, H. Yamauchi, and M. Karppinen, Phys. Rev. B **72**, 104408 (2005).
6. J. Wu, J. W. Lynn, C. J. Glinka, J. Burley, H. Zheng, J. F. Mitchell and C. Leighton, Phys. Rev. Lett., **94**, 037201 (2005).
7. C. N. R. Rao and P. V. Vanitha, Curr. Opin. Solid State Mater. Sci., **6**, 97 (2002); C. N. R. Rao, A. K. Kundu, M. M. Seikh and L. Sudheendra, Dalton Trans., **19**, 3003 (2004).
8. N. Kumar and C. N. R. Rao, J. Solid. State. Chem., **129**, 363 (1997).
9. H. Masuda, T. Fujita, T. Miyashita, M. Soda, Y. Yasui, Y. Kobayashi and M. Sato, J. Phys. Soc. Japan, **72**, 873 (2003).
10. M. Uehara, S. Mori, C. H. Chen and S. W. Cheong, Nature, **399**, 560 (1999).

11. H. J. Lee, K. H. Kim, M. W. Kim, T. W. Noh, B. G. Kim, T. Y. Koo, S. W. Cheong, Y. J. Wang and X. Wei, Phys. Rev. B, **65**, 115118 (2002).

12. A. M. Balagurov, V. Yu Pomjakushin, D. V. Sheptyakov, V. L. Aksenov, P. Fischer, L. Keller, O. Yu Gorbenko, A. R. Kaul and N. A. Babushkina, Phys. Rev. B, **64**, 024420 (2001).

13. L. Sudheendra and C. N. R. Rao, J. Phys.: Condens. Matter, **15**, 3029 (2003).

14. M. Itoh, I. Natori, S. Kubota and K. Matoya, J. Phys. Soc. Japan, **63**, 1486 (1994).

15. P. Ganguly, P. S. Anil Kumar, P. N. Santosh and I. S. Mulla, J. Phys.: Condens. Matter, **6**, 533 (1994).

16. P. S. Anil Kumar, P. A. Joy and S. K. Date, J. Phys.: Condens. Matter, **10**, L487 (1998).

17. J. Wu and C. Leighton, Phys. Rev. B, **67**, 174408 (2003).

18. J. C. Burley, J. F. Mitchell and S. Short, Phys. Rev. B, **69**, 054401 (2004).

19. C. N. R. Rao, J. Phys. Chem. B, **104**, 5877 (2000).

20. H. Y. Hwang, S. W. Cheong, P. G. Radaelli, M. Marezio and B. Batlogg, Phys. Rev. Lett., **75**, 914 (1995).

21. P. M. Woodward, T. Vogt, D. E. Cox, A. Arulraj, C. N. R. Rao, P. Karen, A. K. Cheetam, Chem. Mater., **10**, 3652 (1998).

22. E. O. Wollan and W. C. Koehler, Phys. Rev., **100**, 545 (1955).

23. Y. Tomioka, A. Asamitsu, H. Kuwahara, Y. Moritomo and Y. Tokura, Phys. Rev. B, **53**, R1689 (1996).

24. G. H. Jonker and J. H. Van Santen, Physica, **19**, 120 (1953).

25. H. Taguchi, M. Shimada and M. Koizumi, J. Solid State Chem., **41**, 329 (1982).

39. L. M. Rodriguez-Martinez and J. P. Attfield, Phys. Rev. B, **54**, R15622 (1996); L. M. Rodriguez-Martinez and J. P. Attfield, Phys. Rev. B, **63**, 024424 (2000).

40. I. O. Troyanchuk, D. D. Khalyavin, T. K. Solovykh, H. Szymczak, Q. Huang and J. W. Lynn, J. Phys.: Condens. Matter, **12**, 2485 (2000).

41. H. Kuwahara, Y. Tomioka, A. Asamitgu, Y. Moritomo and Y. Tokura, Science **270**, 961 (1995).

42. C. N. R. Rao, and B. Raveau (Eds), *Colossal Magnetoresistance, Charge Ordering and related properties of Manganese Oxides* (World Scientific: Singapore, 1998).

43. F. Licci, G. Turrili and P. Ferro, J. Mag. Mag. Mater., **164**, L268 (1996); M. Karooinen, M. Matvejeff, K. Salomaki and H. Yamauchi, J. Mater. Chem., **12**, 1761 (2002).

44. A. R. West, *Solid state chemistry and its applications* (John Wiley & Sons: Singapore, 2004); C. N. R. Rao and J. Gopalakrishnan, *New Directions in Solid State Chemistry*, 2nd edition (Cambridge University Press, 1997).

45. W. Tong, L. Hu, H. Zhu, S. Tan and Y. Zhang, J. Phys.: Condens. Matter, **16**, 103 (2004).

46. C. N. R. Rao, M. M. Seikh, and N. Chandrabhas, Top. Curr. Chem. **1**, 234 (2004).

47. N. F. Mott, *Metal-Insulator Transitions*, (Taylor and Francis: London, 1990).

48. C. N. R. Rao and O. Parkash, Phil. Mag., **35**, 1111 (1977); C. N. R. Rao, V. G. Bhide and N. F. Mott, Phil. Mag., **32**, 1277 (1975).

26. N. Gayathri, A. K. Roychaudhuri, S. K. Tiwary, R. Gundakaram, A. Arulraj and C. N. R. Rao, Phys. Rev. B, **56**, 1345 (1997).

27. R. Ganguly, I. K. Gopalakrishnan and J. V. Yakhmi, Physica B, **271**, 116 (1999).

28. C. N. R. Rao, O. Prakash, D. Bahadur, P. Ganguly and S. Nagabhushana, J. Solid State Chem., **22**, 353 (1977).

29. H. W. Brinks, H. Fjellvag, A. Kjekshus and B. C. Hauback, J. Solid State Chem., **147**, 464 (1999).

30. K. Yoshii and A. Nakamura, Physica B, **281 & 282**, 514 (2000).

31. M. A. Senaris-Rodriguez and J. B. Goodenough, J. Solid State Chem., **118**, 323 (1995).

32. H. Masuda, T. Fujita, T. Miyashita, M. Soda, Y. Yasui, Y. Kobayashi and M. Sato, J. Phys. Soc. Japan, **72**, 873 (2003).

33. J. B. Goodenough and P. M. Raccah, Phys. Rev., **155**, 932 (1967).

34. V. G. Bhide, D. S. Rajoria, C. N. R. Rao, G. R. Rao and V. G. Jadhao, Phys. Rev. B, **12**, 2832 (1975).

35. I. O. Troyanchuk, N. V. Kasper, D. D. Khalyavin, H. Szymczak, R. Szymczak and M. Baran, Phys. Rev. Lett., **80**, 3380 (1998).

36. I. O. Troyanchuk, N. V. Kasper, D. D. Khalyavin, H. Szymczak, R. Szymczak and M. Baran, Phys. Rev. B, **58**, 2418 (1998).

37. Y. Moritomo, M. Takeo, X. J. Liu, T. Akimoto and A. Nakamura, Phys. Rev. B, **58**, R13334 (1998).

38. P. V. Vanitha, A. Arulraj, P. N. Santosh, C. N. R. Rao, Chem. Mater., **12**, 1666 (2000).

49. J. A. Mydosh, in *"Spin Glasses: An Experimental Introduction"* Taylor and Francis, London (1993); K. Binder and A. P. Young, Rev. Mod. Phys., **58**, 801 (1986).

50. R. Mathieu, P. Nordblad, D. N. H. Nam, N. X. Phuc and N. V. Khiem, Phys. Rev. B, **63**, 174405 (2001).

51. D. N. H. Nam, R. Mathieu, P. Nordblad, N. V. Khiem and N. X. Phuc, Phys. Rev. B, **62**, 1027 (2000).

52. L. Lundgren, P. Svedlindh, P. Nordblad, and O. Beckman, Phys. Rev. Lett., **51**, 911 (1983).

53. D. S. Fisher, and D. A. Huse, Phys. Rev. B, **38**, 373 (1988).

54. R. Mathieu, P. Jonsson, D. N. H. Nam, and P. Nordblad, Phys. Rev. B, **63**, 092401 (2001).

55. S. Tsubouchi, T. Kyomen, M. Itoh and M. Oguni, Phys. Rev. B, **69**, 144406 (2004).

56. S. Roy, M. Khan, Y. Q. Guo, J. Craig, N. Ali, Phys. Rev. B, **65**, 064437 (2002).

57. P. V. Vanitha and C. N. R. Rao, J. Phys: Condens. Matter., **13**, 11707 (2001).

58. C. N. R. Rao, P. V. Vanitha, A. K. Cheetham, Chem. Euro. J., **9**, 829 (2003).

59. A. A. Taskin, A. N. Lavrov, Y. Ando, Phys. Rev. Lett., **90**, 227201 (2003).

60. K. Yoshii, S. Tsutsui and A. Nakamura, J. Mag. Mag. Mater., **226-230,** 829 (2001).

61. K. Yoshii, H. Abe and A. Nakamura, Mat. Res. Bull., **36**, 1447 (2001).